

STOCKHOLM UNIVERSITY

Doctoral Studies in Physics

Licentiate Thesis  
Akademisk avhandling för avläggande av filosofie  
licentiatexamen vid Stockholm universitet

# Search for Supersymmetry in Monojet Final States with the ATLAS Experiment



**Advisor:**  
doc. Christophe CLEMENT  
**Co-Supervisor:**  
doc. David MILSTEAD

**Candidate:**  
Gabriele BERTOLI

---

SEPTEMBER 29, 2016





# Acknowledgments

# Contents

<b>Acknowledgments</b>	IV
<b>1 Introduction</b>	1
1.1 Author's Contribution . . . . .	1
<b>2 Theoretical overview</b>	3
2.1 The Standard Model . . . . .	3
2.1.1 Electroweak Symmetry Group . . . . .	3
2.1.2 Electroweak Interactions . . . . .	6
2.2 The Higgs mechanism . . . . .	7
2.2.1 Non Abelian Spontaneously Broken Symmetry . . . . .	8
2.2.2 The Higgs Mechanism . . . . .	9
2.2.3 Masses for the $W^\pm$ and $Z^0$ Gauge Bosons . . . . .	10
<b>3 Beyond the Standard Model</b>	11
3.1 Open Questions of the Standard Model . . . . .	11
3.1.1 The Hierarchy Problem and Naturalness . . . . .	11
3.1.2 Dark Matter . . . . .	12
3.2 Supersymmetry . . . . .	12
<b>4 Experimental Apparatus</b>	15
4.1 The Large Hadron Collider . . . . .	15
4.2 The ATLAS Detector . . . . .	16
4.2.1 The Coordinate System . . . . .	16
4.2.2 The Inner Detector . . . . .	18
4.2.3 The Calorimeter . . . . .	19
4.2.4 The Muon Spectrometer . . . . .	20
4.2.5 The Forward Detectors . . . . .	21
4.2.6 The Trigger System . . . . .	21
<b>5 Noise Studies with the Tile Calorimeter</b>	23
5.1 Calorimetry . . . . .	23
5.1.1 Electromagnetic Shower . . . . .	23
5.1.2 Hadronic Shower . . . . .	23
5.1.3 Energy Resolution . . . . .	24
5.2 The ATLAS TileCal . . . . .	24
5.2.1 Signal Reconstruction . . . . .	26
5.2.2 Electronic Noise . . . . .	28
5.3 The 2011 TileCal Run I Reprocessing . . . . .	29

5.3.1	Results	30
5.4	Time Stability	32
5.5	Conclusions	36
<b>6</b>	<b>Physical Objects Reconstruction</b>	39
6.1	Primary Vertex	39
6.2	Track reconstruction	39
6.3	Electrons	40
6.4	Muons	41
6.5	Topocluster	42
6.6	Jets	42
6.6.1	The $\text{anti-}k_{\text{t}}$ Algorithm	43
6.6.2	The Jet Vertex Tagger	43
6.6.3	Jet Calibration	44
6.6.4	Jet Selection	44
6.7	Overlap Removal	45
6.8	Missing Transverse Energy	45
<b>7</b>	<b>The Monojet Signature</b>	47
7.1	Motivation	47
7.2	Event Selection	49
7.3	Jet Veto	49
7.4	Sources of Background	50
7.5	Estimation of the $Z + \text{jets}$ and $W + \text{jets}$ backgrounds	52
7.5.1	The Muon Control Region	52
7.5.2	The Electron Control Region	53
7.5.3	The Di-Muon Control Region	53
7.5.4	The Global Simultaneous Likelihood Fit	54
7.6	Other Backgrounds	55
7.6.1	The Multi-Jet Background	55
7.6.2	The Non-Collision Background	56
7.7	Systematic Uncertainties	56
7.7.1	Theoretical Uncertainties	57
7.7.2	Experimental Uncertainties	57
7.8	Results and Interpretations	58
7.8.1	The Signal Hypothesis Exclusion Procedure	58
7.8.2	Expected Limits	59
7.8.3	Model Independent Limits	60
7.8.4	SUSY Compressed Spectra Interpretation	61
<b>8</b>	<b>Conclusions</b>	63
<b>Appendix A</b>	<b>Further Studies</b>	65
<b>Bibliography</b>		70

# List of Tables

2.1	Weak Isospin and Hypercharge Quantum Numbers of Leptons and Quarks	5
5.1	The table reports the comparison between the double Gaussian parameters stored in the COOL database and those obtained from the fit for two different run numbers corresponding to before and after the jump for a cell where there is no variation in the cell noise. . . . .	34
5.2	The table reports the comparison between the double Gaussian parameters stored in the COOL database and those obtained from the fit for two different run numbers corresponding to before and after the jump for a cell where a variation in the cell noise was spotted. . . . .	35
6.1	Electron definition for the monojet analysis. . . . .	41
6.2	Muon definitions for the monojet analysis. . . . .	42
6.3	Jet definition in the monojet analysis. . . . .	45
7.1	Definition of the signal region. . . . .	50
7.2	Summary table of the different background processes and the corresponding control regions used to evaluate the normalization factors. . .	55
7.3	Results on the expected and observed upper limits on the number of events, $S_{\text{exp}}^{95}$ and $S_{\text{obs}}^{95}$ respectively and on the visible cross section at 95% CL. . . . .	61

# List of Figures

4.1	The LHC injection chain [19]. . . . .	16
4.2	Section of the ATLAS detector showing the interaction of different particle types with the sub-detectors [20]. . . . .	17
4.3	Overview of the ATLAS detectors with its main sub-detectors [13]. . . . .	17
4.4	Schematic view of a charged track of 10 GeV $p_T$ that traverses the different ID sub-detectors. After traversing the beryllium pipe, the track passes through the three cylindrical silicon-pixel layers, the four layers of silicon-microstrip sensors (SCT) and the approximately 36 straws contained in the TRT within their support structure [13]. . . . .	19
4.5	Cut-away view of the ATLAS calorimeter system [13]. . . . .	20
4.6	Cut-away view of the ATLAS muon spectrometer [13]. . . . .	21
5.1	Cut away showing an individual TileCal module along with the optical read out and design of a TileCal module [25]. . . . .	25
5.2	Schematic view of the TileCal layer and cell structure in a plane containing the beam axis $z$ [27]. . . . .	26
5.3	The ATLAS TileCal calibration chain [29]. . . . .	28
5.4	Comparison between the TileCal electronic noise, measured as the RMS of the reconstructed amplitude distribution in pedestal runs and the $\sigma$ of the Gaussian fit of the distribution for the old and new LVPS [31]. . .	29
5.5	$\phi$ -averaged RMS of electronic cell noise as a function of $\eta$ of the cell, with both readout channels in High Gain. For each cell the average value over all modules is taken. Values have been extracted using all the calibration runs used for the 2011 RUN I reprocessing. The different cell types are shown separately, A, BC, D, and E (gap/crack). The transition between the long and extended barrels can be seen in the range $0.7 <  \eta  < 1.0$ . HGHG combination is relevant when the energy deposition in the cell is $\lesssim 15$ GeV [32]. . . . .	30
5.6	$\phi$ -averaged RMS of electronic cell noise as a function of $\eta$ of the cell, with both readout channels in Low Gain. For each cell the average value over all modules is taken. Values have been extracted using all the calibration runs used for the 2011 RUN I reprocessing. The different cell types are shown separately, A, BC, D, and E (gap/crack). The transition between the long and extended barrels can be seen in the range $0.7 <  \eta  < 1.0$ . LGLG combination is relevant when the energy deposition in the cell is $\gtrsim 15$ GeV [32]. . . . .	31

5.7	$\phi$ -averaged RMS of electronic cell noise as a function of $\eta$ of the cell, with one readout channel in High Gain and the other in Low Gain. For each cell the average value over all modules is taken. Values have been extracted using all the calibration runs used for the 2011 RUN I reprocessing. The different cell types are shown separately, A, BC, D. E cells do not appear int this plot since they have only one readout channel. The transition between the long and extended barrels can be seen in the range $0.7 <  \eta  < 1.0$ . When the energy deposition in the cell is between $10 \text{ GeV} \lesssim E \lesssim 20 \text{ GeV}$ it can happen that the cell is read out with different voltage on the readout channels [32]. . . . .	31
5.8	Time evolution for two different representative cells in the calorimeter over the entire reprocessing period. The plot shows the change relative to the first run considered for several quantities for different IOVs (vertical dashed lines). If a channel is off due to some problems (Bad channel), this is reported in the plot with a black square. . . . .	33
5.9	Fit of the reconstructed pulse shape on a control cell with no variation (jump) in the cell noise. . . . .	34
5.10	Fit of the reconstructed pulse shape on a cell with variation (jump) in the cell noise non compatible with a change in the calibration, digital noise or channel status. . . . .	35
5.11	Comparison of the reconstructed pulse shape of a cell with the cell noise variation without a corresponding variation in he calibration constants, digital noise or channel status (jump) with the double Gaussian fit superimposed with the noise filter (Figures 5.11a and 5.11b) and without noise filter (Figures 5.11c and 5.11d). . . . .	36
5.12	Comparison between the $\phi$ -averaged RMS of electronic cell noise as a function of $\eta$ of the cell before and after reprocessing for the high statistic 192130 run with both channels in high gain. The different layers are shown separately, A, BC, D and E (gap/crack). The transition between the long and extended barrels can be seen in the range $0.7 <  \eta  < 1.0$ .	37
5.13	Distribution of the ratio $\sigma / \text{RMS}_{\text{eff}}$ where the $\sigma$ and $\text{RMS}_{\text{eff}}$ values are taken from all IOVs considered for the 2011 TileCal reprocessing. .	37
6.1	Track parameters at the perigee. In the figure $\mathbf{p}$ is the momentum of the incoming particle, $\mathbf{e}_x, \mathbf{e}_y, \mathbf{e}_z$ are the versors of the coordinate system defined in Section 4.2.1 and $\theta$ and $\phi$ , also defined in Section 4.2.1 are the polar and azimuthal angle respectively. . . . .	40
7.1	Event topology of squark pair production resulting in a neutralinos with two jets final state with (Figure 7.1b) and without (Figure 7.1a) initial state radiation. . . . .	48
7.2	Exclusion limits for direct production of squark pairs [46]. . . . .	48
7.3	Jet veto efficiency for different jet $p_T$ thresholds and $N(\text{jets}) \leq 4$ as a function of the average number of interactions per bunch crossing $< \mu >$ for a compressed spectra $M_{\tilde{q}} = 450 \text{ GeV}$ $M_{\tilde{\chi}_0^1} = 435 \text{ GeV}$ . In Figure 7.3a no JVT cut is applied and there is some drop of the efficiency at high pile-up. In Figure 7.3b a $\text{JVT} > 0.64$ cut is applied, the dependence from pile-up is reduced. . . . .	51

7.4	Jet veto efficiency for different jet $p_T$ thresholds and $N(\text{jets}) \leq 4$ with a $\text{JVT} > 0.64$ selection applied as a function of the average number of interactions per bunch crossing $\langle \mu \rangle$ for the analysis $Z \rightarrow \nu\bar{\nu}$ background (Figure 7.4a) and the SUSY squark–neutralino signal model with $M_{\tilde{q}} = 450$ GeV and $M_{\tilde{\chi}_0^1} = 435$ GeV. . . . .	51
7.5	Observed and predicted $E_T^{\text{miss}}$ and leading jet $p_T$ distributions after the background only fit in the single muon CR for the $E_T^{\text{miss}} > 250$ GeV selection. The error bands include the statistical and systematic error. . . . .	53
7.6	Observed and predicted $E_T^{\text{miss}}$ and leading jet $p_T$ distributions after the background only fit in the electron CR for the $E_T^{\text{miss}} > 250$ GeV selection. The error bands include the statistical and systematic error. . . . .	54
7.7	Observed and predicted $E_T^{\text{miss}}$ and leading jet $p_T$ distributions after the background only fit in the di-muon CR for the $E_T^{\text{miss}} > 250$ GeV selection. The error bands include the statistical and systematic error. . . . .	54
7.8	Distribution of the $E_T^{\text{miss}}$ and the leading jet $p_T$ for IM1 signal region compared with the background estimates from the background only fit in the control regions. The distributions of different signal models are superimposed for comparison. The contribution from the multi-jet and NCB background is negligible and not reported in the plot. In the ratio window the error bars include experimental and systematic uncertainties. . . . .	58
7.9	Sensitivity to the compressed SUSY models with an integrated luminosity of $L = 3.3 \text{ fb}^{-1}$ in the plane defined by the squark mass $m_{\tilde{q}}$ and the mass difference between the squark mass and the lightest neutralino mass $\Delta m = m(\tilde{q}) - m(\tilde{\chi}_1^0)$ . The color scale reflects the lowest excludable signal strength for a particular mass point. The values indicated on the map indicate the actual excludable $\mu$ values at a some specific SUSY models. The dashed line shows the limit between excludable and not excludable models. The theoretical uncertainties in the signal are not included. . . . .	60
7.10	Expected and observed limits on the SUSY compressed models using the Run 2 2015 data, in the plane defined by the squark mass on the $x$ -axis and the mass difference between the squark and lightest neutralino mass on the $y$ -axis. All experimental and theoretical systematic uncertainties are included. . . . .	62

*Si sta,  
come d'autunno,  
sugli alberi,  
le foglie.*

[G. UNGARETTI, Soldati]

# Chapter 1

## Introduction

The Standard Model of particle physics is the theory used to describe the elementary constituents of matter and their interactions. Through the years it has been tested by many experiments and despite its success it cannot explain, among other problems, the so called hierarchy and dark matter problems. Supersymmetry is an extension of the Standard Model that could solve these issues by introducing new particles. The lightest of these particles, in the context of a minimal supersymmetric model, could be produced through the  $\tilde{q} \rightarrow q + \tilde{\chi}_1^0$  ( $q = u, d, c, s$ ) process and, lacking electromagnetic and strong interaction [1], escape detection. With an energy in the center of mass of  $\sqrt{s} = 13$  TeV, the large hadron collider could be able to produce such kind of particles, the ATLAS detector could be able to infer their presence by the energy unbalance they would create. This thesis presents the result of the search for physics beyond the Standard Model with the ATLAS detector in the  $3.2 \text{ fb}^{-1}$  delivered in 2015 in an experimental signature with jets and large missing transverse momentum in the final state.

### 1.1 Author's Contribution

My contribution to the ATLAS experiment started in early 2013 by studying the electronic noise in the hadronic calorimeter. The Tile Calorimeter is designed to measure jets, tau particles, missing energy and for the energy reconstruction of hadrons, thus having an up-to-date description of the noise in the detector is important for most physics analysis in ATLAS. During the reprocessing of the 2011 data I developed a set of python scripts in order to plot the noise constants variation over several calibration runs. Based on these scripts I carried out new studies of noise evolution some of which are described in Chapter 5. The performance of the ATLAS TileCal were presented in a poster at the “XXVII International Symposium on Lepton Photon Interactions at High Energies (2015)” and appear in the proceedings of the conference on the “Proceedings of Science”.

I later started analyzing the ATLAS data joining the monojet team in the effort of trying to answer relevant Standard Model open questions. During Run I my contribution was limited to the study of some of the systematic uncertainties associated to the cross section for extra dimension models. In Run II the ATLAS software framework was radically changed along with the data format thus the Stockholm analysis code had to be largely rewritten. I am the main contributor to this software that allows to

produce end-user last analysis stage ROOT files from the ATLAS centrally produced data sets.

In the Run II analysis an upper cut on the number of jets was introduced, the efficiency of such a cut was studied using a multivariate method based on the TMVA package and the results, being in agreement with other studies performed in the group, implemented in the analysis. The expected limits and the sensitivity of the SUSY compressed spectra scenario with  $\tilde{q} \rightarrow q + \tilde{\chi}_1^0$  ( $q = u, d, c, s$ ) were for the first time estimated by me in the monojet analysis and lately compared to the observed limit in the  $3.2 \text{ fb}^{-1}$  collected by ATLAS during Run II data taking. The results of this study are summarized in the paper in ref. [2].

# Chapter 2

## Theoretical overview

### 2.1 The Standard Model

The [Standard Model \(SM\)](#) is a theoretical model which describes the elementary constituents of matter and their interactions. Up to now, we discovered three kind of different interactions, the *strong*, the *electroweak* and the *gravitational*; excluding gravity, all of them are described by means of a *quantum field gauge theory*.

The Standard Model is the collection of these gauge theories, it is based on the gauge symmetry group  $SU(3)_C \times SU(2)_L \times U(1)_Y$  where  $SU(3)_C$  is the symmetry group of the *Quantum Chromo-Dynamics* (QCD), the “C” subscript stands for *color charge* which is the conserved charge in the strong interaction. The  $SU(2)_L$  is the weak isospin group acting on *left-handed* doublet of fermions while the  $U(1)_Y$  group is the *hypercharge* symmetry group. Together  $SU(2)_L \times U(1)_Y$  form the electroweak symmetry group.

The Standard Model also contains and has predicted the existence of *elementary particles* that interacts between them via the forces mentioned above. The matter constituents are called *fermions*, the interaction are mediated by other particles called *gauge bosons*. Fermions are further categorized into *quark* which bound to form *hadrons* and interact through the strong force and *leptons* which do not experience the strong force. These are the true fundamental constituents of matter; the gauge bosons arise from the gauge symmetry group of the Standard Model.

The existence of all the leptons, quarks and gauge bosons is confirmed by experimental tests. Among the bosons, the Higgs boson is peculiar because, unlike the others, it carries spin 0 and it is not associated with any interaction, instead arises as a consequence of the *spontaneously broken symmetry* of the electroweak sector which is the property, responsible of giving mass to all the elementary particles and the weak gauge bosons.

#### 2.1.1 Electroweak Symmetry Group

We can now see how to find out the weak interaction symmetry group, to this end, let us start by writing out the *Hamiltonian* for the weak interaction:

$$H_{weak} = \frac{4G_F}{\sqrt{2}} J_\mu^\dagger J^\mu \quad (2.1.1)$$

where

$$\begin{aligned} J_\mu &\equiv J_\mu^{(+)} = \bar{\psi}_{\nu_e} \gamma_\mu \frac{1}{2} (1 - \gamma_5) \psi_e \equiv \bar{\nu}_{e_L} \gamma_\mu e_L \\ J_\mu^\dagger &\equiv J_\mu^{(-)} = \bar{\psi}_e \gamma_\mu \frac{1}{2} (1 - \gamma_5) \psi_{\nu_e} \equiv \bar{e}_L \gamma_\mu \nu_{e_L}, \end{aligned} \quad (2.1.2)$$

here  $J_\mu^{(+)}$  and  $J_\mu^{(-)}$  are the charge weak currents,  $\gamma_\mu$  ( $\mu = 0, 1, 2, 3$ ) are the Dirac matrices and  $\gamma_5 = i\gamma_0\gamma_1\gamma_2\gamma_3$ . To easy the notation, let us write:

$$\chi_L = \begin{pmatrix} \nu_{e_L} \\ e_L^- \end{pmatrix} \equiv \begin{pmatrix} \nu_e \\ e^- \end{pmatrix} \quad (2.1.3)$$

and using the Pauli matrices

$$\tau_\pm = \frac{1}{2}(\tau_1 \pm i\tau_2) \quad (2.1.4)$$

we have:

$$\begin{aligned} J_\mu^{(+)} &= \bar{\chi}_L \gamma_\mu \tau_+ \chi_L \\ J_\mu^{(-)} &= \bar{\chi}_L \gamma_\mu \tau_- \chi_L \end{aligned} \quad (2.1.5)$$

by introducing a “neutral” current:

$$J_\mu^{(3)} = \bar{\chi}_L \gamma_\mu \frac{\tau_3}{2} \chi_L = \frac{1}{2} \bar{\nu}_L \gamma_\mu \nu_L - \frac{1}{2} \bar{e}_L \gamma_\mu e_L \quad (2.1.6)$$

we have a “triplet” of currents:

$$J_\mu^i = \bar{\chi}_L \gamma_\mu \frac{\tau_i}{2} \chi_L. \quad (2.1.7)$$

Now if chose an  $SU(2)_L$  transformation:

$$\chi_L(x) \rightarrow \chi'_L(x) = e^{i\vec{\varepsilon} \cdot \vec{T}} \chi_L(x) = e^{i\vec{\varepsilon} \cdot \frac{\vec{T}}{2}} \chi_L(x), \quad (2.1.8)$$

where  $T_i = \tau_i/2$  are the  $SU(2)_L$  generators, and think the  $\chi_L$  as the fundamental representation, then the current triplet is a triplet of  $SU(2)_L$ , the weak isotopic spin.

The right handed fermions are singlet for the  $SU(2)_L$ , thus:

$$e_R \rightarrow e'_R = e_R. \quad (2.1.9)$$

Since we are considering the global transformations, we have no interaction, so the Lagrangian reads:

$$\mathcal{L} = \bar{e} i \gamma^\mu \partial_\mu e + \bar{\nu} i \gamma^\mu \partial_\mu \nu \equiv \bar{\chi}_L i \gamma^\mu \partial_\mu \chi_L + \bar{e}_R i \gamma^\mu \partial_\mu e_R; \quad (2.1.10)$$

for now we are bounded to set  $m_e = 0$ , in fact the mass term couples right and left fermion’s components and it is not  $SU(2)_L$  invariant. In 1973, experiments detected events of the type:

$$\bar{\nu}_\mu e^- \rightarrow \bar{\nu}_\mu e^- \quad (2.1.11)$$

$$\begin{cases} \nu_\mu N \rightarrow \nu_\mu X \\ \bar{\nu}_\mu N \rightarrow \bar{\nu}_\mu X \end{cases} \quad (2.1.12)$$

which are evidence of a neutral current. Further investigations yielded that the neutral weak current is predominantly  $V - A$  (i.e. left-handed) but not purely  $V - A$  so the  $J_\mu^{(3)}(x)$  current introduced above can not be used as it involves only left handed fermions. We know a neutral current that mixes left and right components namely the electromagnetic current:

$$J_\mu \equiv e J_\mu^{(em)} = e \bar{\psi} \gamma_\mu Q \psi \quad (2.1.13)$$

where  $Q$  is the charge operator with eigenvalue  $Q = -1$  for the electron.  $Q$  is the generator of the  $U(1)_{(em)}$  group. So we have an isospin triplet and we have included the right hand components, the isospin singlet, what we want to do, is to combine them and define the hypercharge operator:

$$Y = 2(Q - T_3) \rightarrow Q = T_3 + \frac{Y}{2}, \quad (2.1.14)$$

for the current we have

$$J_\mu^{(em)} = J_\mu^{(3)} + \frac{1}{2} J_\mu^Y \quad (2.1.15)$$

where

$$J_\mu^Y = \bar{\psi} \gamma_\mu Y \psi \quad (2.1.16)$$

so, by analogy, the hypercharge  $Y$  generates a  $U(1)_Y$  symmetry, and, as it is a  $SU(2)_L$  singlet, leaves (2.1.10) invariant under the transformations:

$$\begin{aligned} \chi_L(x) &\rightarrow \chi'_L(x) = e^{i\beta Y} \chi_L(x) \equiv e^{i\beta y_L} \chi_L \\ e_R(x) &\rightarrow e'_R(x) = e^{i\beta Y} e_R(x) \equiv e^{i\beta y_R} e_R. \end{aligned} \quad (2.1.17)$$

We thus have incorporated the electromagnetic interactions extending the group to  $SU(2)_L \times U(1)_Y$  and instead of having a single symmetry group we have a direct product of groups, each with his own *coupling constant*, so, in addition to  $e$  we will have another coupling to be found. Since we have a direct product of symmetry groups, the generators of  $SU(2)_L$ ,  $T_i$ , and the generators of  $U(1)_Y$ ,  $Y$  commute, the commutation relations are:

$$[T_+, T_-] = 2T_3 \quad ; \quad [T_3, T_\pm] = \pm T_\pm \quad ; \quad [Y, T_\pm] = [Y, T_3] = 0, \quad (2.1.18)$$

member of the same isospin triplet, have same hypercharge eigenvalue; the relevant quantum numbers are summarized in the table 2.1.

<b>Lepton</b>	$T$	$T^{(3)}$	$Q$	$Y$	<b>Quark</b>	$T$	$T^{(3)}$	$Q$	$Y$
$\nu_e$	$\frac{1}{2}$	$\frac{1}{2}$	0	-1	$u_L$	$\frac{1}{2}$	$\frac{1}{2}$	$\frac{2}{3}$	$\frac{1}{3}$
$e_L^-$	$\frac{1}{2}$	$-\frac{1}{2}$	-1	-1	$d_L$	$\frac{1}{2}$	$-\frac{1}{2}$	$-\frac{1}{2}$	$\frac{1}{3}$
$e_R^+$	0	0	-1	-2	$u_R$	0	0	$\frac{2}{3}$	$\frac{4}{3}$
					$d_R$	0	0	$-\frac{1}{3}$	$-\frac{2}{3}$

Table 2.1: Weak Isospin and Hypercharge Quantum Numbers of Leptons and Quarks

### 2.1.2 Electroweak Interactions

As stated before, interactions are mediated by a gauge boson, we now want to find out those for the electroweak interaction, to this end let us consider *local* gauge transformations

$$\begin{aligned}\chi_L &\rightarrow \chi'_L = e^{i\vec{\epsilon}(x) \cdot \vec{T} + i\beta(x)Y} \chi_L \\ \psi_R &\rightarrow \psi'_R = e^{i\beta(x)Y} \psi_R,\end{aligned}\tag{2.1.19}$$

introducing four gauge bosons,  $W_\mu^{(1)}, W_\mu^{(2)}, W_\mu^{(3)}, B_\mu$  (same as the number of generators) and the *covariant derivative*

$$\begin{aligned}D_\mu \chi_L &= (\partial_\mu + ig \frac{\vec{\tau}}{2} \cdot \vec{W}_\mu(x) + i \frac{g'}{2} y_L B_\mu(x)) \chi_L \\ &= (\partial_\mu + ig \frac{\vec{\tau}}{2} \cdot \vec{W}_\mu(x) - i \frac{g'}{2} B_\mu(x)) \chi_L \\ D_\mu \psi_R &= (\partial_\mu + i \frac{g'}{2} y_R B_\mu(x)) \psi_R \\ &= (\partial_\mu - i \frac{g'}{2} B_\mu(x)) e_R\end{aligned}\tag{2.1.20}$$

the Lagrangian (2.1.10) reads

$$\begin{aligned}\mathcal{L} &= \bar{\chi}_L i\gamma^\mu \partial_\mu \chi_L + \bar{e}_R i\gamma^\mu \partial_\mu e_R - g \bar{\chi}_L \gamma^\mu \frac{\vec{\tau}}{2} \chi_L \vec{W}_\mu + \frac{g'}{2} (\bar{\chi}_L \gamma^\mu \chi_L + 2 \bar{e}_R \gamma^\mu e_R) B_\mu \\ &\quad - \frac{1}{4} \vec{W}_{\mu\nu} \vec{W}^{\mu\nu} - \frac{1}{4} B_{\mu\nu} B^{\mu\nu}\end{aligned}\tag{2.1.21}$$

where

$$\begin{aligned}\vec{W}_{\mu\nu} &= \partial_\mu \vec{W}_\nu - \partial_\nu \vec{W}_\mu - g \vec{W}_\mu \times \vec{W}_\nu \\ B_{\mu\nu} &= \partial_\mu B_\nu - \partial_\nu B_\mu\end{aligned}\tag{2.1.22}$$

are the kinetic plus non abelian interaction term for the  $SU(2)_L$  symmetry (first equation) and the kinetic term for the abelian symmetry group  $U(1)_Y$ . We can now split the Lagrangian terms to find out the field of the vector bosons coupled to the charged current and to the neutral current.

**Charged Currents Interaction** Let us consider the term

$$\mathcal{L}_{int}^{ew} = -g \bar{\chi}_L \gamma_\mu \frac{\vec{\tau}}{2} \chi_L \vec{W}_\mu + \frac{g'}{2} \bar{\chi}_L \gamma_\mu \chi_L B^\mu + g' \bar{e}_R \gamma_\mu e_R B^\mu\tag{2.1.23}$$

defining

$$W_\mu^\pm = \frac{1}{\sqrt{2}} W^{(1)} \mp i W^{(2)}\tag{2.1.24}$$

we can write

$$\mathcal{L}^{CC} = -\frac{g}{\sqrt{2}} (J_\mu^{(+)} W^{-\mu} + J_\mu^{(-)} W^{+\mu})\tag{2.1.25}$$

and recognize two charged vector bosons with coupling given by “ $g$ ”.

**Neutral Current Interaction** The relevant term left to consider for what concerns the electroweak currents is

$$\mathcal{L}^{NC} = -g J_\mu^{(3)} W^{(3)\mu} - \frac{g'}{2} J_\mu^Y B^\mu, \quad (2.1.26)$$

the electromagnetic interaction,  $-ie J^{(em)\mu} A_\mu$ , is embedded in this expression as will became clear considering the *spontaneously broken symmetry* phenomena, for now, is sufficient to define

$$\begin{aligned} W_\mu^{(3)} &= \cos \theta_w Z_\mu + \sin \theta_w A_\mu \\ B_\mu &= -\sin \theta_w Z_\mu + \cos \theta_w A_\mu \end{aligned} \quad (2.1.27)$$

and invert to get

$$\begin{aligned} A_\mu &= \sin \theta_w W_\mu^{(3)} + \cos \theta_w B_\mu \\ Z_\mu &= \cos \theta_w W_\mu^{(3)} - \sin \theta_w B_\mu \end{aligned} \quad (2.1.28)$$

where  $\theta_w$  is the electroweak *mixing angle*. Plugging this into (2.1.26) and rearranging terms

$$\begin{aligned} \mathcal{L}^{NC} &= -[(g \sin \theta_w J_\mu^{(3)} + \frac{g'}{2} \cos \theta_w J_\mu^Y) A^\mu \\ &\quad + (g \cos \theta_w J_\mu^{(3)} - \frac{g'}{2} \sin \theta_w J_\mu^Y) Z^\mu] \end{aligned} \quad (2.1.29)$$

since  $A^\mu$  is the photon field, the first parenthesis must be identified with the electro-magnetic current, thus

$$-(g \sin \theta_w J_\mu^{(3)} + \frac{g'}{2} \cos \theta_w J_\mu^Y) A^\mu = -e J_\mu^{(em)} A^\mu \equiv -e (J_\mu^{(3)} + \frac{J_\mu^Y}{2}) A^\mu \quad (2.1.30)$$

from which we get the relation

$$g \sin \theta_w = g' \cos \theta_w = e \quad (2.1.31)$$

and so we can rewrite (2.1.26),

$$\mathcal{L}^{NC} = -\frac{g}{\cos \theta_w} [J_\mu^{(3)} - \sin^2 \theta_w J_\mu^{(em)}] Z^\mu \quad (2.1.32)$$

so that  $Z^\mu$  can be identified with the field for the neutral vector boson.

## 2.2 The Higgs mechanism

Up to now, we have massless gauge vector bosons, in fact no term such as  $M^2 B_\mu B^\mu / 2$  appear in the Lagrangian (2.1.21), but this kind of terms are not gauge invariant and thus we can not just add them or we will end up with troubles later when trying to renormalize the theory.

A gauge invariant way to recover the fermions and bosons masses, is to spontaneously brake the local  $SU(2)_L \times U(1)_Y$  electroweak symmetry.

### 2.2.1 Non Abelian Spontaneously Broken Symmetry

Let us consider a local symmetry breaking and refer to [3] for a more complete explanation. Be  $\phi$  a complex scalar field,

$$\mathcal{L} = (\partial_\mu \phi^*)(\partial_\mu \phi) - \underbrace{\mu^2 \phi^* \phi - \lambda(\phi^* \phi)^2}_{V(\phi^* \phi)} \quad (2.2.1)$$

setting

$$\begin{aligned} \phi &= \frac{\phi_1 + i\phi_2}{\sqrt{2}} \\ \phi^* &= \frac{\phi_1 - i\phi_2}{\sqrt{2}} \end{aligned} \quad (2.2.2)$$

we get

$$\mathcal{L} = \frac{1}{2}(\partial_\mu \phi_1)^2 + \frac{1}{2}(\partial_\mu \phi_2)^2 - \frac{\mu^2}{2}(\phi_1^2 + \phi_2^2) - \frac{\lambda}{4}(\phi_1^2 + \phi_2^2)^2 \quad (2.2.3)$$

the gauge transformations are

$$\begin{cases} \phi(x) \rightarrow \phi'(x) = e^{-i\epsilon} \phi(x) \\ \phi^\dagger(x) \rightarrow \phi'^\dagger(x) = e^{-i\epsilon} \phi^\dagger(x). \end{cases} \quad (2.2.4)$$

There are two possible choices for the potential

- $\mu^2 > 0$ , which gives a stable configuration around  $|\phi| = 0$ .
- $\mu^2 < 0$ , which gives a circle of minima such that  $\phi_1^2 + \phi_2^2 = v^2$ , with  $v^2 = -\mu^2/\lambda$ .  
This minima are not gauge invariant, in fact

$$\phi_0 = \langle 0 | \phi | 0 \rangle \rightarrow \frac{v}{\sqrt{2}} e^{i\alpha} \quad \text{if } \phi \rightarrow e^{i\alpha} \phi \quad (2.2.5)$$

To get the particle interaction we make a perturbative expansion around one minimum, we chose one, for example  $\alpha = 0$ , for which  $\phi_1 = v$  and  $\phi_2 = 0$  and introduce the two perturbations  $\eta(x)$  and  $\xi(x)$  so that

$$\phi(x) = \frac{1}{\sqrt{2}} v + \overbrace{\xi(x)}^{\phi_1} + i \overbrace{\eta(x)}^{\phi_2} \quad (2.2.6)$$

and plug them in the Lagrangian (2.2.3) to obtain

$$\begin{aligned} \mathcal{L}'(\xi, \eta) &= \frac{1}{2}(\partial_\mu \xi)^2 + \frac{1}{2}(\partial_\mu \eta)^2 - \frac{1}{2}(-2\mu^2)\eta^2 \\ &\quad - \lambda v(\eta^2 + \xi^2)\eta - \frac{1}{4}(\eta^2 + \xi^2)^4 + \dots \end{aligned} \quad (2.2.7)$$

as we can see, the third term looks like a mass term so that the field  $\eta$  has mass  $m_\eta^2 = -2\mu^2$  while we have no mass term for the field  $\xi$ .

This “trick” to give mass to one of the gauge field, is the *breaking of the symmetry*. In fact, by choosing one particular vacuum among the infinite ones, we lost our gauge invariance; moreover, we ended up with a scalar gauge boson, known as *Goldstone boson*. We need to find a way to recover the masses of the gauge bosons in a gauge invariant way by getting rid of massless scalar fields; the solution is the topic of the very next section. next section.

### 2.2.2 The Higgs Mechanism

Consider now a local gauge  $SU(2)$  symmetry, the field transformations are

$$\phi(x) \rightarrow \phi'(x) = e^{i\sum_{k=1}^3 \epsilon^k T^k} \phi(x), \quad (2.2.8)$$

where  $T^k = \frac{\tau^k}{2}$  and  $[T^i, T^j] = i\epsilon^{ijk}T^k$  with  $i, j, k = 1, 2, 3$ . To achieve invariance for the Lagrangian

$$\mathcal{L} = (\partial_\mu \phi)^\dagger (\partial^\mu \phi) - \mu^2 \phi^\dagger \phi - \lambda (\phi^\dagger \phi)^2, \quad (2.2.9)$$

where

$$\phi \equiv \begin{pmatrix} \phi_i \\ \phi_j \end{pmatrix} = \frac{1}{\sqrt{2}} \begin{pmatrix} \phi_1 + i\phi_2 \\ \phi_3 + i\phi_4 \end{pmatrix}, \quad (2.2.10)$$

we need to introduce the covariant derivative

$$D_\mu = \partial_\mu + ig \frac{\vec{\tau}}{2} \cdot \vec{W}_\mu(x). \quad (2.2.11)$$

In the case of infinitesimal transformations, the fields transform like

$$\phi(x) \rightarrow \phi'(x) \simeq (1 + i\vec{\epsilon}(x) \cdot \frac{\vec{\tau}}{2})\phi(x) \quad (2.2.12)$$

while the gauge bosons transformations are

$$\vec{W}_\mu(x) \rightarrow \vec{W}'_\mu(x) - \frac{1}{g} \partial_\mu \vec{\epsilon}(x) - \vec{\epsilon}(x) \times \vec{W}_\mu(x). \quad (2.2.13)$$

Replacing everything in the Lagrangian we obtain

$$\mathcal{L} = (\partial_\mu \phi + ig \frac{\vec{\tau}}{2} \cdot \vec{W}_\mu \phi)^\dagger (\partial_\mu \phi + ig \frac{\vec{\tau}}{2} \cdot \vec{W}_\mu) - V(\phi) - \frac{1}{4} \vec{W}_{\mu\nu} \cdot \vec{W}^{\mu\nu}, \quad (2.2.14)$$

where the potential is given by

$$V(\phi) = \mu^2 \phi^\dagger \phi + \lambda (\phi^\dagger \phi)^2 \quad (2.2.15)$$

and the kinetic term is

$$\vec{W}_{\mu\nu} = \partial_\mu \vec{W}_\nu - \partial_\nu \vec{W}_\mu - g \vec{W}_\mu \times \vec{W}_\nu. \quad (2.2.16)$$

We are interested in the case of the spontaneously broken symmetry, thus  $\mu^2 < 0$  and  $\lambda > 0$ . The minima of the potential lie on

$$\phi^\dagger \phi = \frac{1}{2} (\phi_1^2 + \phi_2^2 + \phi_3^2 + \phi_4^2) = -\frac{\mu^2}{2\lambda} \quad (2.2.17)$$

and we have to choose one of them, let it be

$$\phi_1 = \phi_2 = \phi_4 = 0, \quad \phi_3^2 = -\frac{\mu^2}{\lambda} \equiv v^2. \quad (2.2.18)$$

To expand  $\phi$  around this particular vacuum

$$\phi_0 \equiv \frac{1}{\sqrt{2}} \begin{pmatrix} 0 \\ v \end{pmatrix} \quad (2.2.19)$$

it is sufficient to substitute the expansion

$$\phi(x) = \frac{1}{\sqrt{2}} \begin{pmatrix} 0 \\ v + h(x) \end{pmatrix} \quad (2.2.20)$$

in the Lagrangian (2.2.14) in order to get rid of the, unobserved, Goldstone bosons and retain only one neutral scalar field, the *Higgs field*.

### 2.2.3 Masses for the $W^\pm$ and $Z^0$ Gauge Bosons

The gauge bosons masses are generated simply substituting the vacuum expectation value,  $\phi_0$ , in the Lagrangian, the relevant term is

$$\begin{aligned}
 & \left| (g \frac{\vec{\tau}}{2} \cdot \vec{W}_\mu + \frac{g'}{2} B_\mu) \phi \right|^2 = \\
 &= \frac{1}{8} \left| \begin{pmatrix} gW_\mu^3 + g'B_\mu & g(W_\mu^1 - iW_\mu^2) \\ g(W_\mu^1 + iW_\mu^2) & -gW_\mu^3 + g'B_\mu \end{pmatrix} \begin{pmatrix} 0 \\ v \end{pmatrix} \right|^2 \\
 &= \frac{1}{8} v^2 g^2 [(W_\mu^1)^2 + (W_\mu^2)^2] + \frac{1}{8} v^2 (g'B_\mu - gW_\mu^3)(g'B_\mu - gW_\mu^{3\mu}) \\
 &= (\frac{1}{2} gv)^2 W_\mu^+ W^{-\mu} + \frac{1}{8} v^2 (W_\mu^3 - B_\mu) \begin{pmatrix} g^2 & -gg' \\ -gg' & g^2 \end{pmatrix} \begin{pmatrix} W^{3\mu} \\ B^\mu \end{pmatrix}
 \end{aligned} \tag{2.2.21}$$

having used  $W^\pm = (W^1 \mp iW^2)/\sqrt{2}$ . The mass term, lead us to conclude that

$$M_W = \frac{1}{2} gv. \tag{2.2.22}$$

The remaining term is off diagonal

$$\begin{aligned}
 \frac{1}{8} v^2 [g^2 (W_\mu^3)^2 - 2gg' W_\mu^3 B^\mu + g'^2 B_\mu^2] &= \frac{1}{8} v^2 [gW_\mu^3 - gB_\mu]^2 \\
 &+ 0 \quad [g'W_\mu^3 - g'B_\mu]^2
 \end{aligned} \tag{2.2.23}$$

but one can diagonalize and find that

$$\begin{aligned}
 A^\mu &= \frac{g'W_\mu^3 + gB_\mu}{\sqrt{g^2 + g'^2}} \\
 Z^\mu &= \frac{gW_\mu^3 + g'B_\mu}{\sqrt{g^2 + g'^2}}
 \end{aligned} \tag{2.2.24}$$

with  $M_A = 0$  and  $M_Z = v\sqrt{g^2 + g'^2}/2$  which are the photon and neutral weak vector boson fields. Thus the mass eigenstates are a massless vector boson,  $A_\mu$  and a massive gauge boson  $Z_\mu$ .

We have shown in this section how the Higgs mechanism can be applied to give mass to the gauge bosons of the electroweak model.

# Chapter 3

## Beyond the Standard Model

### 3.1 Open Questions of the Standard Model

The Standard Model was introduced in the early 1970s and has so far managed to explain the interactions between the elementary particles that constitutes the building blocks of matter. Through the years it has been tested in a number of experiments and predicted the existence of the  $W$  and  $Z$  bosons, the charm and top quark and of the Higgs boson that was recently discovered. Despite its great success, the Standard Model only explains three of the four fundamental interactions, failing to incorporate gravity. There are also some open questions that are not answered by the theory as we know it so far, two of these are briefly outlined in the sections below, namely: the *hierarchy problem* and *dark matter*. The answer to these questions is the search focus of [Beyond Standard Model \(BSM\)](#) theories.

#### 3.1.1 The Hierarchy Problem and Naturalness

The *naturalness criterion* states that: “one such [dimensionless and measured in units of the cut-off ( $\Lambda$ )] parameter is allowed to be much smaller than unity only if setting it to zero increases the symmetry of the theory. If this does not happen, the theory is unnatural” [4].

One important concept in physics that enter in the formulation of the naturalness principle is that of symmetries. *Symmetries* are closely connected to conservation laws through the Noether’s theorem, moreover theory parameters that are protected by a symmetry, if smaller than the unit, are not problematic according to the naturalness criterion.

Let us consider the strength of the gravitational force, characterized by the Newton’s constant,  $G_N$  and the weak force, characterized by the Fermi’s constant  $G_F$ , if we take the ratio of these we get:

$$\frac{G_F \hbar^2}{G_N c^2} = 1.738 \times 10^{33}. \quad (3.1.1)$$

The reason why this number is worth some attention is that theory parameters close to the order of unit in the SM, may be calculated in a more fundamental theory, if any, using fundamental constants like  $\pi$  or  $e$  while numbers that deviates from one, may not have such a simple mathematical expression and thus may lead to uncover new properties of the fundamental theory.

This number becomes even more interesting if we consider quantum effects. *Virtual particles* are off-shell ( $E \neq m^2 + p^2$ ) and according to the *uncertainty principle*,  $\Delta t \Delta E \geq \hbar/2$ , can appear out of the vacuum for a short time that depends on the energy of the virtual particle; according to quantum field theory, the vacuum is populated with virtual particles. The Higgs field has the property to couple with other SM particles with a strength proportional to their mass. All these virtual particles have a mass determined by the cut-off energy  $\Lambda$  and when the Higgs field travels through space, couples with these virtual particles and its mass squared gets a contribution proportional to  $\Lambda$  (see [5]):

$$\delta m_H^2 = k\Lambda^2, \text{ with } k = \frac{3G_F}{4\sqrt{2}\pi^2} (4m_t^2 - 2m_W^2 - m_Z^2 - m_H^2). \quad (3.1.2)$$

Since  $k \approx 10^{-2}$  [5], the value of Higgs mass  $m_H (\sim G_F^{-1/2})$ , should be close to the maximum energy scale  $\Lambda$  and if we assume this to be the Plank scale  $M_{Pl} = G_N^{-1/2}$ , the ratio  $G_F/G_N$ , should be close to the unity which contradicts Eq. (3.1.1), this goes by the name of *hierarchy problem*.

The large quantum corrections in Eq. (3.1.2) are mainly due to the fact that in the SM, there is no symmetry protecting the mass of the Higgs field.

### 3.1.2 Dark Matter

Observations on galaxies rotation suggests that their mass is not enough to generate the gravitational force needed to counteract the effect of the centripetal force and to prevent them to torn apart [6]. Since observation also suggest that stars and planets in galaxies are indeed kept together by the gravitational attraction, we conclude that there must be extra mass that we cannot see that generate the gravity needed to hold them together. This unknown matter goes by the name of *dark matter* and is thought to be made of **Weakly Interacting Massive Particles (WIMPs)**. These particles do not interact or interact weakly with the electromagnetic force, as a consequence, dark matter does not emit, reflect or absorb light making it hard to detect. Cosmological measurements on the content of matter of the universe have been performed [7] that seems to suggest that the visible matter (the one we can see and measure), only accounts for 5% of the total energy of the universe and that dark matter constitutes roughly the 27%, the remaining 68% is called *dark energy* and is believed to be responsible for the accelerated expansion of the universe. Some theories [8] predict that dark matter particles should be light enough to be produced at hadron colliders but due to their “dark” nature, they would escape detection leading to an energy imbalance in the detector that could be used as an hint of their existence.

## 3.2 Supersymmetry

One possible solution to the dark matter and the hierarchy problem is achieved introducing a symmetry, called **Supersymmetry (SUSY)** [9], that relates fermions and bosons. Supersymmetry is capable of solving the hierarchy problem by canceling out the quantum corrections that bring  $m_H$  close to  $\Lambda$  thus restoring the naturalness of the SM. SUSY introduces a set of new particles that are the *superpartners* of the SM ones. These supersymmetric particles or *sparticles* have the same quantum numbers and couplings of their SM counterpart but turn with a supersymmetry transformation a spin 1/2 fermionic SM particle into a bosonic spin 0 sparticle and a spin 1 SM boson

in a spin 1/2 fermion while a scalar particle becomes a spin 1/2 sparticle. The superpartners of the SM leptons are called *sleptons*, adding the “s” prefix (that stands for “scalar”) to their SM fermionic partners and are denoted with a “~” on top of their symbol, so for example the SM electrons are called *selectrons* and denoted with  $\tilde{e}_L$  and  $\tilde{e}_R$  where the R and L does not refer to their helicity (being 0-spin bosons) but to that of their SM superpartners. Similarly for *smuons* and *staus*:  $\tilde{\mu}_L, \tilde{\mu}_R, \tilde{\tau}_L, \tilde{\tau}_R$  and for the *squarks*:  $\tilde{q}_L, \tilde{q}_R$  (with  $q = u, d, s, b, c, t$ ). The supersymmetric partners of the gauge bosons are called *gauginos*, adding the “ino” suffix to their SM partners, for instance, the  $W$  and  $Z$  bosons have the *wino* ( $\widetilde{W}$ ) and *zino* ( $\widetilde{Z}$ ) superpartners, the photon has the *photino* ( $\widetilde{\gamma}$ ) and the Higgs field has the *Higgsino* ( $\widetilde{H}$ ). In addition to these new particles, the minimal supersymmetric extension of the Standard Model, called **Minimal Supersymmetric Standard Model (MSSM)** [1], introduces three neutral and two charged Higgs bosons leading to five physical Higgs states. The neutral superpartners of these Higgs states ( $\widetilde{H}^0$ ), combine with the bino and the wino ( $\widetilde{B}, \widetilde{W}^0$ ) in four new electrically neutral mass eigenstates called *neutralinos* ( $\widetilde{\chi}_i^0$  with  $i = 1, 2, 3, 4$ ). The charged higgsinos ( $\widetilde{H}^+, \widetilde{H}^-$ ) and the winos ( $\widetilde{W}^+, \widetilde{W}^-$ ) mix and give rise to two electrically charged mass eigenstates of charge  $\pm 1$  called *charginos* ( $\widetilde{\chi}_i^\pm$  with  $i = 1, 2$ ). In the MSSM framework a new multiplicative quantum number can be introduced, the R-parity, that, if it is conserved, explains the stability of the proton and is defined as:

$$R = (-1)^{3(B-L)+2S} \quad (3.2.1)$$

where  $B$  and  $L$  are the baryon and lepton numbers respectively and  $S$  is the spin. It can be seen that all SM particles have  $R = +1$  while supersymmetric particles have  $R = -1$ . The conservation of R-parity has important phenomenological consequences:

- The **Lightest Supersymmetric Particle (LSP)** is stable.
- The final decay products of SUSY particles are an odd number.
- In collider experiments sparticles can only be produced in pairs.

If the LSP is stable and electrically neutral (dark) and interacts only weakly with matter it makes a good candidate for non-baryonic dark matter [10]. In the MSSM, good LSP candidates are either the neutralino or the gravitino, the supersymmetric partner of the graviton (the hypothetical gauge boson associated to gravitation).

No sparticle has been observed at particle colliders so far, hinting that they must have a larger mass than their SM counterparts. If they had the same mass they would have already been produced at particle colliders, this imply that SUSY is a *broken symmetry*. Detecting one of these supersymmetric particles would shed light on some of the SM shortcomings and thus many searches at the current colliders focus their attention on finding SUSY particles.

Supersymmetry is expected to solve some of the shortcomings of the Standard Model mentioned in Section 3.1, it is possible to estimate, from Eq. (3.1.2), the scale at which new physics is expected. Using  $m_H = 125$  GeV [11], we get that  $\Lambda \approx 1$  TeV. If the naturalness criterion holds, we thus expect the two main experiments at LHC, ATLAS and CMS, to find signal for new physics at the TeV scale.



## Chapter 4

# Experimental Apparatus

### 4.1 The Large Hadron Collider

The [Large Hadron Collider \(LHC\)](#) [12] is a two ring superconducting hadron accelerator and collider located at the [European Organization for Nuclear Research \(CERN\)](#).

The performance of a collider is evaluated in terms of its available *center of mass energy*,  $\sqrt{s}$  and the *instantaneous luminosity*  $\mathcal{L}$ . The former defines the accessible energies for particle production. The latter is defined as the interaction rate per unit cross section of the colliding beams (collisions / (cm<sup>2</sup> s)).

The LHC is designed to operate at  $\sqrt{s} = 14$  TeV in the center of mass although it started off at 7 TeV in 2010 and 2011, 8 TeV in 2012 and 13 TeV in 2015 after the long shutdown in 2013 and 2014.

There are six experiments at LHC: ATLAS [13], CMS [14], ALICE [15], LHCb [16], LHCf [17] and TOTEM [18]. ATLAS and CMS are designed to work with the maximum luminosity that LHC can provide  $\sim 10^{34}$  cm<sup>-2</sup> s<sup>-1</sup>. This requirement, due to the low efficiency production, excludes the use of anti-proton beams and therefore the LHC is designed to be a [proton-proton \(\*pp\*\)](#) and heavy ions collider. The protons are organized in bunches, accelerated by LINAC2 to an energy of 50 MeV and subsequently injected in the [Proton Synchrotron Booster \(PSB\)](#). Here they are further accelerated to an energy of 1.4 GeV and fed to the [Proton Synchrotron \(PS\)](#) where they reach the energy of 25 GeV to be then passed to the [Super Proton Synchrotron \(SPS\)](#) which accelerate them to an energy of 450 GeV. They are finally injected in the LHC in opposite directions where they reach the nominal energy. There are four interaction points where the four main experiments (ATLAS, CMS, ALICE, LHCb) are located, at these locations, every 25 ns, the bunches cross and interact with each other (*bunch crossing*). A schematic view of the injection chain is depicted in Figure 4.1.

The instantaneous luminosity depends on the beam parameters and is given by:

$$\mathcal{L} = \frac{N_b^2 n_b f_{rev} \gamma}{4\pi \epsilon_n \beta^*} F \quad (4.1.1)$$

where  $N_b$  is the number of particles per bunch,  $n_b$  is the number of bunches per beam,  $f_{rev}$  is the revolution frequency,  $\gamma$  is the relativistic gamma factor,  $\epsilon_n$  the normalized transverse beam emittance, the beta function is a measure of the transverse beam size and  $\beta^*$  is the value of the beta function at the interaction point and  $F$  is the geometric reduction factor due to the crossing angle of the beams at the [interaction](#)

point (IP) [12]. The integrated luminosity is given by:

$$L = \int \mathcal{L} dt \quad (4.1.2)$$

and the integral is carried over data taking periods of the detector. The integrated luminosity can be related to the total number of events of a certain process by:

$$N_{events} = L\sigma_{events} \quad (4.1.3)$$

where  $N_{events}$  is the total number of events,  $L$  is the integrated luminosity and  $\sigma_{events}$  is the cross section for the process in units of barn ( $1 \text{ b} = 10^{-28} \text{ m}^2$ ). In 2015 ATLAS recorded an integrated luminosity of  $3.2 \text{ fb}^{-1}$ .

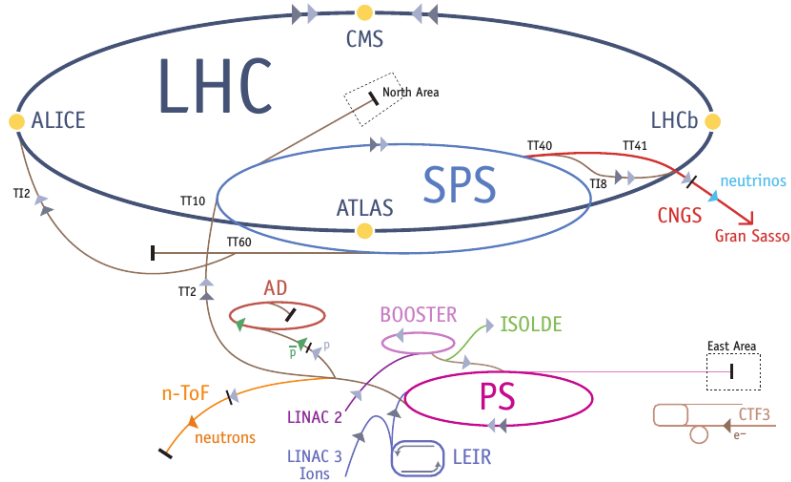


Figure 4.1: The LHC injection chain [19].

## 4.2 The ATLAS Detector

A Toroidal LHC apparaS (ATLAS) is a multi purpose detector designed to be sensitive to a large physics signatures (supersymmetry and dark matter, briefly introduced in Section 3.2 and Section 3.1.2) and to fully take advantage of the LHC potential. It is capable of identifying photons, electrons, muons, taus, jets and missing energy, Figure 4.2 shows a schematic view of the interaction of the different kind of particles with the ATLAS sub-detectors while Figure 4.3 shows the ATLAS detector with its subsystems. In the following sections a brief overview of the various subsystems that allow particle identification and reconstruction is presented.

### 4.2.1 The Coordinate System

A right handed coordinate system is defined for the ATLAS detector, the origin is at the geometric center of ATLAS with the  $z$ -axis oriented along the beam direction and the  $xy$  plane orthogonal to it. The positive  $x$ -axis points to the center of the LHC ring while the positive  $y$ -axis is pointing upwards. The A-side of the detector is defined as that with a positive  $z$ -axis while the C-side has the negative  $z$ -axis.

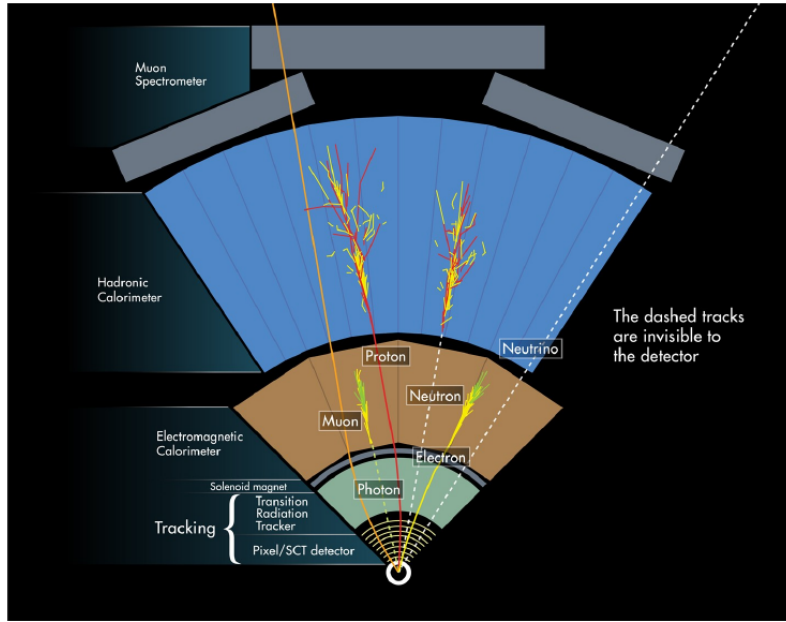


Figure 4.2: Section of the ATLAS detector showing the interaction of different particle types with the sub-detectors [20].

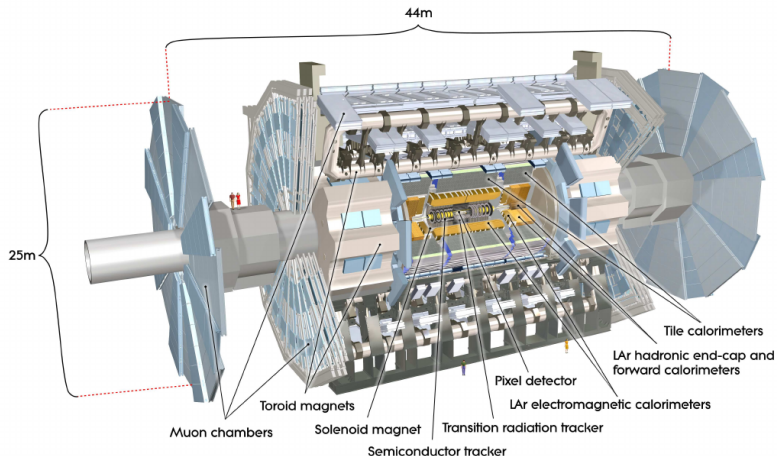


Figure 4.3: Overview of the ATLAS detectors with its main sub-detectors [13].

The LHC beams are unpolarized and thus invariant under rotations around the beam line axis, a cylindrical coordinate system is particularly convenient to describe the detector geometry where:

$$r = \sqrt{x^2 + y^2}, \quad \phi = \arctan \frac{y}{x}. \quad (4.2.1)$$

A momentum dependent coordinate, the *rapidity*, is commonly used in particle physics for its invariance under Lorentz transformations along the  $z$ -axis. The rapidity is

defined as:

$$y = \frac{1}{2} \ln \frac{E + p_z}{E - p_z} \quad (4.2.2)$$

where  $E$  is the energy of the particle and  $p_z$  its momentum along the  $z$ -axis. Rapidity intervals are Lorentz invariant under boost along the  $z$ -axis. In the relativistic limit or when the mass of the particle is negligible, the rapidity only depends on the production angle of the particle with respect to the beam axis,

$$\theta = \arctan \frac{\sqrt{p_x^2 + p_y^2}}{p_z}. \quad (4.2.3)$$

This approximation is called **pseudorapidity ( $\eta$ )** and is defined as:

$$y \xrightarrow{p \gg m} \eta = -\ln \left( \tan \frac{\theta}{2} \right). \quad (4.2.4)$$

A value of  $\theta = 90^\circ$ , perpendicular to the beam axis, corresponds to  $\eta = 0$ . The spatial separation between particles in the detector is commonly given in terms of a Lorentz invariant variable defined as:

$$\Delta R = \sqrt{\Delta\phi^2 + \Delta\eta^2}. \quad (4.2.5)$$

Other quantities used to describe the kinematics of the  $pp$  interaction are the **transverse momentum ( $p_T$ )** and the **transverse energy ( $E_T$ )** defined as  $p_T = p \sin \theta$  and  $E_T = E \sin \theta$  respectively.

### 4.2.2 The Inner Detector

The **Inner Detector (ID)** [13] is designed to provide good track reconstruction, precise momentum resolution and both primary and secondary vertex measurements (see Section 6.1) above a nominal  $p_T$  threshold of 0.5 GeV and within the pseudorapidity  $|\eta| < 2.5$ . The ID is 6.2 m long and has a radius of about 1.1 m, it is surrounded by a solenoidal magnetic field of 2 T. Its layout is schematized in Figure 4.4 and, as can be seen, it is composed of three sub-detectors.

At the inner radius the *pixel detector* measures charged particles with silicon sensors with a minimum and maximum size of  $50 \times 400 \mu\text{m}^2$  and  $50 \times 600 \mu\text{m}^2$  respectively.

In the middle of the ID the **SemiConductor Tracker (SCT)** is designed to give eight precision measurements per track which contribute to determine the primary and secondary vertex position and momentum measurements. The silicon sensors are 80  $\mu\text{m}$  pitch micro strips.

The last layer of the ID is the **Transition Radiation Tracker (TRT)**, it contributes to tracking and identification of charged particles. It consists of drift (straw) tubes, 4 mm in diameter with a 31  $\mu\text{m}$  wire in the center of each straw, filled with a gas mixture. These tubes substantially act like proportional counters where the tube is the cathode and the wire is the anode and set to ground. When a charged particle crosses one tube, leaves a signal; the set of signals in the tubes, reconstructs to a track which represents the path of the crossing object. The space between the straw tubes is filled with material with a different dielectric constant than the inside, this causes charged particles crossing the boundaries to emit transition radiation thus leading to some straw to have a much stronger signal. The transition radiation depends on the Lorentz  $\gamma$  factor which in turn depends on the energy and the mass of the particles.

Lighter particles will have higher transition energy and stronger signal in the straw tubes. This allows to distinguish between electrons (the lightest charged particle) and single hadrons (pions), for instance, tracks with several strong signal straw, can be identified as belonging to electrons.

An additional layer, the **Insertable B-Layer (IBL)**, was recently added in the region between the beam pipe and the inner pixel layer (B-layer). It is designed to increase the tracking robustness by replacing damaged parts of the pixel B-layer and increasing the hit redundancy with higher luminosity. In addition, being closer to the beam pipe it increases the impact parameter measurement precision [21].

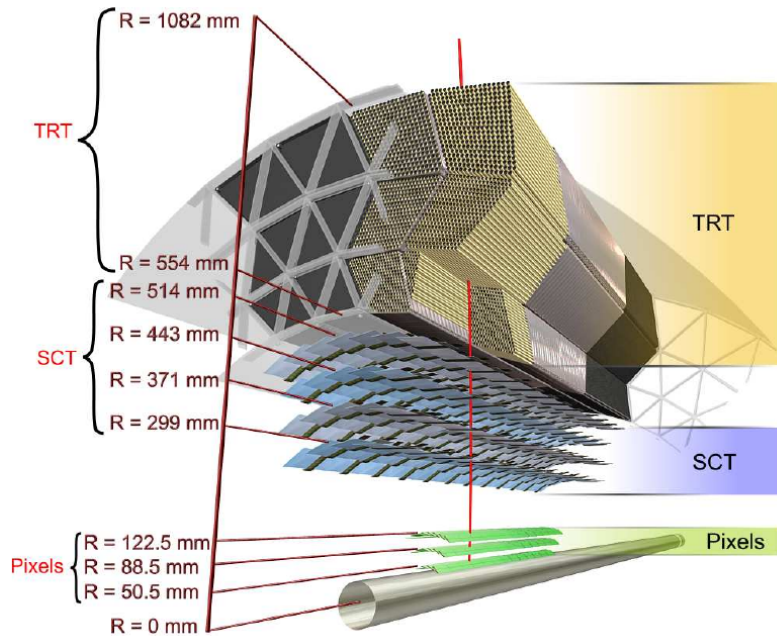


Figure 4.4: Schematic view of a charged track of 10 GeV  $p_T$  that traverses the different ID sub-detectors. After traversing the beryllium pipe, the track passes through the three cylindrical silicon-pixel layers, the four layers of silicon-microstrip sensors (SCT) and the approximately 36 straws contained in the TRT within their support structure [13].

### 4.2.3 The Calorimeter

The main purpose of a calorimeter is to measure the energy of electrons, photons and hadrons by mean of materials capable of completely absorbing the energy of the incoming particles transforming it in some measurable quantity. Calorimeters can be classified in two categories, **electromagnetic (EM)** and **hadronic** depending on the particle they are designed to detect. The EM calorimeters are used to detect photons and electrons while the task of hadronic calorimeters is to identify hadrons. Both types of calorimeters can be further divided into *sampling calorimeters* and *homogeneous calorimeters*. Sampling calorimeters alternate layers of a dense material used to absorb the energy of incident particles (absorber) and an active material to collect the signal. The interaction between the particles and the absorber produces a shower of secondary particles with progressively degraded energy which is deposited

in the active material in form of charge or light that can be converted into energy. Homogeneous calorimeters use only one material that serves both as an absorber and an active material [22].

The ATLAS calorimeter is a sampling calorimeter covering up the  $|\eta| < 4.9$  region the large  $\eta$  coverage, ensures a good missing transverse momentum measurement (see Section 6.8); an illustration of the system is shown in Figure 4.5.

The EM calorimeter has a barrel and two end-caps, covering the  $|\eta| < 1.475$  and  $1.375 < |\eta| < 3.2$  region respectively. It uses [Liquid Argon \(LAr\)](#) as active material and lead as absorber in an accordion geometry that provides  $\phi$  symmetry without azimuthal cracks. In the region  $|\eta| < 1.8$  a presampler consisting of a LAr active region is used to correct for electrons and photons energy loss upstream of the calorimeter.

There are three hadronic calorimeters: the [Tile Calorimeter \(TileCal\)](#), the [Hadronic End-cap Calorimeter \(HEC\)](#) and the [LAr Forward Calorimeter \(FCal\)](#). The TileCal barrel and extended barrels cover the  $|\eta| < 1.0$  and  $0.8 < |\eta| < 1.7$  and uses steel as absorber and scintillating tiles connected to photomultiplier tubes through wavelength shifting fibers for readout as an active material. The HEC covers the  $1.5 < |\eta| < 3.2$  region and, to avoid drops in material density at the transition, it overlaps slightly with the FCal that covers the  $3.1 < |\eta| < 4.9$ .

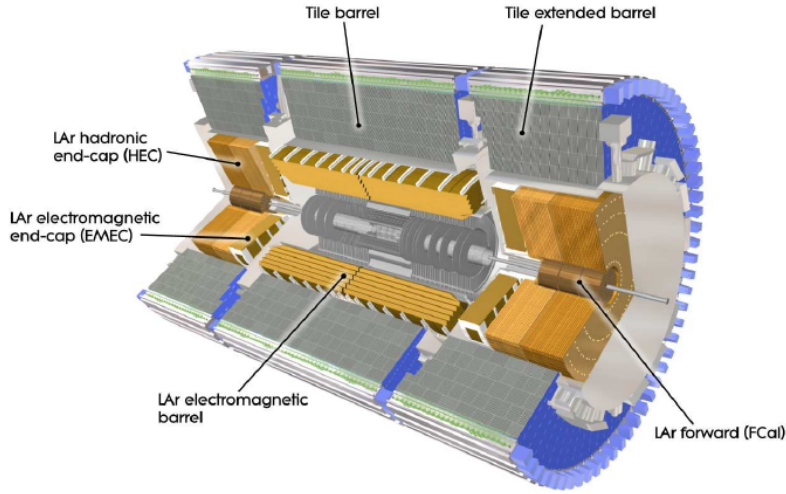


Figure 4.5: Cut-away view of the ATLAS calorimeter system [13].

#### 4.2.4 The Muon Spectrometer

The [Muon Spectrometer \(MS\)](#) is designed to identify muons and measure their momentum. It is divided in four sub-detectors, the [Monitored Drift Tubes \(MDT\)](#), the [Cathode Strip Chambers \(CSC\)](#), the [Resistive Plate Chambers \(RPC\)](#), and the [Thin Gap Chamber \(TGC\)](#). The sub-detectors are immersed in a magnetic field generated by three different toroidal magnets, a barrel toroid covering the  $|\eta| < 1.4$  region and two end-caps magnets at  $1.6 < |\eta| < 2.7$ , which produces a field almost perpendicular to the muon tracks.

The MDT covers the  $|\eta| < 2.7$  region and provides a precise measurement of the track coordinates in the principal bending direction of the magnetic field. It uses drift tubes to reconstruct the muon trajectory and the drift time of the ionized charges

is used to determine the minimum distance between the wire and the muon. The CSC covers the  $2.0 < |\eta| < 2.7$  region and is a multi-wire proportional chamber with cathodes segmented in strips, one perpendicular to the anode wire, providing the precision coordinate, and the other parallel to it (giving the transverse coordinate).

The RPC and the TGC cover the  $|\eta| < 1.05$  and  $1.05 < |\eta| < 2.7$  regions respectively. They contribute to the Level 1 trigger providing bunch crossing identification, it allows to select high and low  $p_T$  tracks and measure the muon coordinate in the direction orthogonal to that determined by MDT and CSC.

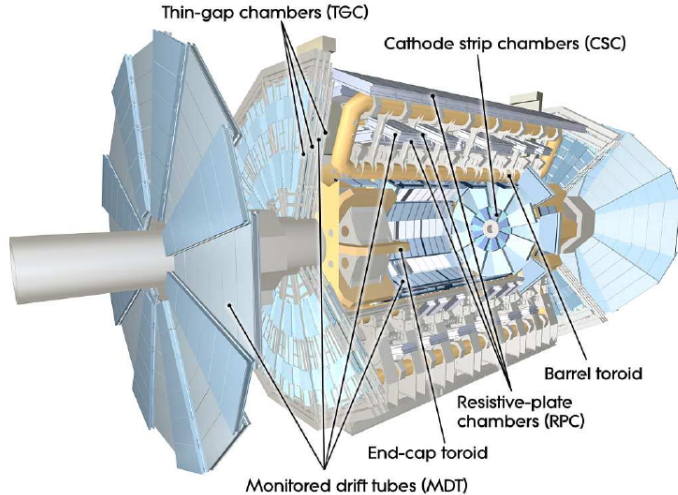


Figure 4.6: Cut-away view of the ATLAS muon spectrometer [13].

#### 4.2.5 The Forward Detectors

The ATLAS forward region is covered by three smaller detectors: the [LUminosity measurement using Cerenkov Integrating Detector \(LUCID\)](#), the [Absolute Luminosity For ATLAS \(ALFA\)](#) and the [Zero-Degree Calorimeter \(ZDC\)](#). LUCID [23] is located at  $\pm 17$  m from the IP, it is designed to monitor the relative luminosity by detecting the inelastic  $pp$  scattering. The ZDC [23] is located at  $\pm 140$  m from the IP, it consists of alternating layers of quartz rods and tungsten plates designed to measure neutron at  $|\eta| < 8.2$ , its purpose is to measure the centrality in heavy-ion collisions. ALFA [23] is located at  $\pm 240$  m from the IP and is designed to measure the absolute luminosity via elastic scattering at small angles.

#### 4.2.6 The Trigger System

The bunch crossing rate at LHC is 40 MHz for a bunch spacing of 25 ns (about 7 meters). Each event recorded by ATLAS requires  $\approx 1.4$  MB of disk space, with approximately 20 to 50 collisions per bunch crossing, the storage space required to record all the events in a second would be  $\approx 60$  TB. This is not feasible thus only the most interesting events are selected and stored on disk. The *trigger system* decides whether to keep or not a collision event for later studies, it consists of a hardware based [Level One \(L1\)](#) trigger and a software based [High Level Trigger \(HLT\)](#).

The L1 trigger determines [Region of Interest \(RoIs\)](#) in the detector using custom hardware and coarse information from the calorimeter and the muon system. The L1 trigger is capable of reducing the event rate to 100 kHz with a decision time for a L1 accept of  $2.5\ \mu\text{s}$ . The RoIs from the L1 trigger are sent to the HLT where different algorithms are run using the full detector information and reducing the L1 output rate to 1 kHz with a processing time of about 200 ms [24].

In the monojet analysis presented in this thesis, the HLT\_xe70 trigger is used, it receives an L1 accept that selects events with a missing energy (see Section 6.8) greater than 50 GeV, no muons are used in the reconstruction of the missing energy at the trigger level. The events that survive L1 are then passed to the HLT level, where events with a missing energy greater than 70 GeV are selected.

# Chapter 5

# Noise Studies with the Tile Calorimeter

## 5.1 Calorimetry

The particle interactions with matter cause them to lose energy. The particle's energy and its type determines the processes causing the energy loss; these can be of two kind, *electromagnetic* and *hadronic*. In this section a brief overview of the physics behind the two is given.

### 5.1.1 Electromagnetic Shower

High energy electrons and photons lose energy mainly by *radiation* and *conversion*. When electrons with energies greater than  $\sim 10$  MeV interact with the electromagnetic field of the absorber nuclei, a deceleration and thus a loss of energy in form of a photon (*Bremsstrahlung*) can occur. Photons in this energy range produce mostly electron-positron pairs.

Electrons and photons with a sufficient amount of energy interacting with an absorber, produce secondary photons through Bremsstrahlung or secondary electrons and positrons by pair production. These secondary particles will produce more particles through the same mechanisms giving rise to a shower of particles with progressively lower energies. When the energy loss in the shower is dominated by ionization and thermal excitation of the active material atoms, the number of particles in the shower stops growing and there is no further shower development. The above process goes on until the energy of the electrons falls below a critical energy,  $\epsilon$ , where ionization and excitation becomes the dominant effects [22].

### 5.1.2 Hadronic Shower

Hadrons lose energy through strong interaction with the calorimeter material. The strong interaction is responsible for the production of energetic secondary hadrons with momenta typically at the GeV scale and nuclear reactions such as excitation or nucleon spallation in which neutrons and protons are released from the nuclei with a characteristic energy at the MeV scale.

The energetic hadron produced contain protons, neutrons and pions. On average, 1/3 of the pion produced are neutral pions which decay to photons ( $\pi \rightarrow \gamma\gamma$ ). The

photons produced this way will initiate an electromagnetic shower as described in Section 5.1.1 transferring energy from the hadronic part to the electromagnetic shower inside the hadronic shower. The electromagnetic component of the shower does not contribute any more to hadronic processes. The nucleons released by excitation or nuclear spallation, require an energy equal to their binding energy to be released and are not recorded as a contribution to the calorimeter signal thus producing a form of *invisible energy*. Some detectors can compensate for the loss of invisible energy, these are called *compensating calorimeters* [22].

### 5.1.3 Energy Resolution

The energy resolution of a detector measures its ability of distinguishing between particles of different energies; the better the energy resolution, the better it can separate energy peaks belonging to different decays.

The energy resolution can be written as:

$$\frac{\sigma_E}{E} = \frac{a}{\sqrt{E}} \oplus \frac{b}{E} \oplus c, \quad (5.1.1)$$

where the  $\oplus$  symbol indicates a quadratic sum. The first term (*a*) in the equation is the *stochastic term*, it is mainly due to fluctuations related to the physical evolution of the shower. In homogeneous calorimeters, this term is small because the energy deposited in the active volume by a monochromatic beam of particles is constant for each event. In a sampling calorimeter, the active layers are interleaved with absorber layers thus the energy deposited in the active material fluctuates event by event. These are called *sampling fluctuations* and, in sampling electromagnetic calorimeters, represents the greatest limitation to energy resolution due to the variation in the number of charged particles which cross the active layers. The second term (*b*) in eq. (5.1.1) is called the *noise term*, it comes from the electronic noise of the detector readout chain. Sampling or homogeneous calorimeters which collect the signal in the form of light, using for example a photo-multiplier tube with a high gain multiplication of the signal with a low electronic noise, can achieve low levels of noise. Calorimeters that collect the signal in form of charge, must use an pre-amplifier having thus a higher level of noise. In sampling calorimeters, the noise term can be further reduced by increasing the sampling fraction, this way there is a larger signal coming from the active material and a higher noise-to-signal ratio. The last term (*c*) of the equation is the *constant term*, it does not depend on the energy of the particles but includes all the non uniformities in the detector response such as instrumental effect, imperfections in the calibration of different parts of the detector, radiation damage, detector aging, or the detector geometry [22].

## 5.2 The ATLAS TileCal

TileCal is the central hadronic calorimeter of the ATLAS experiment covering the  $|\eta| < 1.7$  region. It is designed for energy measurement of hadrons, jets, tau particles and also contributes to the measurement of missing transverse energy (see Section 6.8). TileCal is a scintillator steel non compensating sampling calorimeter, the scintillation light produced in the tiles is transmitted by [Wavelength Shifting Fibers \(WSFs\)](#) to [PhotoMultiplier Tubes \(PMTs\)](#). The analog signals from the PMTs are amplified, shaped and digitized by sampling the signal every 25 ns. The TileCal front end electronics read out the signals produced by about 10000 channels measuring energies

ranging from 30 MeV to 2 TeV. The readout system is responsible for reconstructing the data in real time. The digitized signals are reconstructed with the Optimal Filtering algorithm (see Section 5.2.1), which computes for each channel the signal amplitude, time and quality factor at the required high rate.

TileCal is designed as one **Long Barrel (LB)** covering the  $|\eta| < 1.0$  range and two **Extended Barrel (EB)** in the  $0.8 < |\eta| < 1.7$  range. The barrels are further divided, according to their geometrical position on the  $z$ -axis, in partitions called EBA, LBA, EBC and LBC (see Section 4.2.1). Each partition consists of 64 independent wedges (see Figure 5.1) called *modules* assembled in azimuth ( $\phi$ ). The LBA and EBA partitions are shown in Figure 5.2.

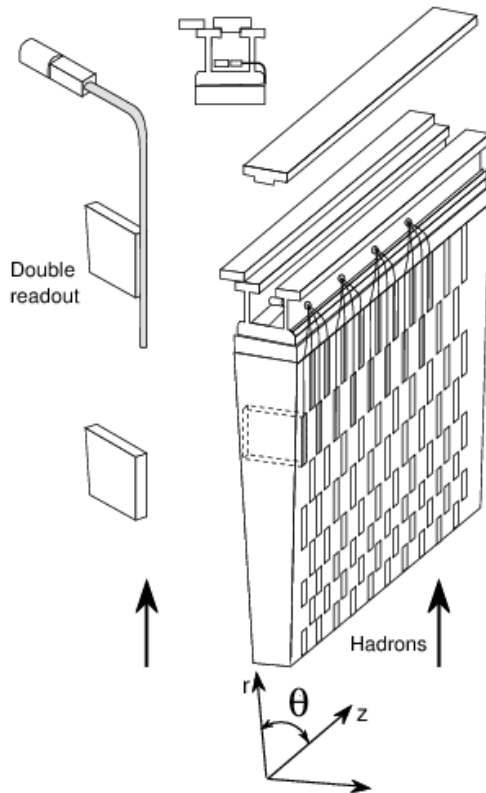


Figure 5.1: Cut away showing an individual TileCal module along with the optical read out and design of a TileCal module [25].

Between the LB and the EB there is a 600 mm gap needed for the ID and the LAr cables, electronics and services. Part of the gap contains the **Intermediate Tile Calorimeter (ITC)**, a detector designed to maximize the active material while leaving enough space for services and cables. The ITC is an extension of the EB and it occupies the  $0.8 < |\eta| < 1.6$  region. The combined  $0.8 < |\eta| < 1.0$  part is called *plug* and in the  $1.0 < |\eta| < 1.6$  region, for space reasons, the ITC is not interleaved with an absorber and is only composed of scintillator material. The scintillators between  $1.0 < |\eta| < 1.2$  are called *gap scintillators*, while those between  $1.2 < |\eta| < 1.6$  are called *crack scintillators*. The plug and the gap scintillators mainly provide hadronic shower sampling while the crack scintillator, which extends to the region between the barrel

and the end-cap cryostats, samples the electromagnetic shower in a region where the normal sampling is impossible due to the dead material of the cryostat walls and the ID cables.

TileCal is also divided in longitudinal layers, the A, BC and D layers as shown in Figure 5.2. The two innermost layers have a  $\Delta\eta \times \Delta\phi$  segmentation of  $0.1 \times 0.1$  while in the outermost, the segmentation is  $0.1 \times 0.2$ . Each layer is logically divided into *cells* (also shown in Figure 5.2) by grouping together in the same PMT the fibers coming from different scintillator tiles belonging to the same radial depth. The gap/crack scintillators are also called E layer cells.

The energy resolution for jets in ATLAS is:

$$\frac{\sigma_E}{E} = \frac{50\%}{\sqrt{E}} \oplus 3\% \quad (5.2.1)$$

for  $|\eta| < 3$ . The 3% constant term becomes dominant for high energy hadrons where an increase in energy resolution is expected [26].

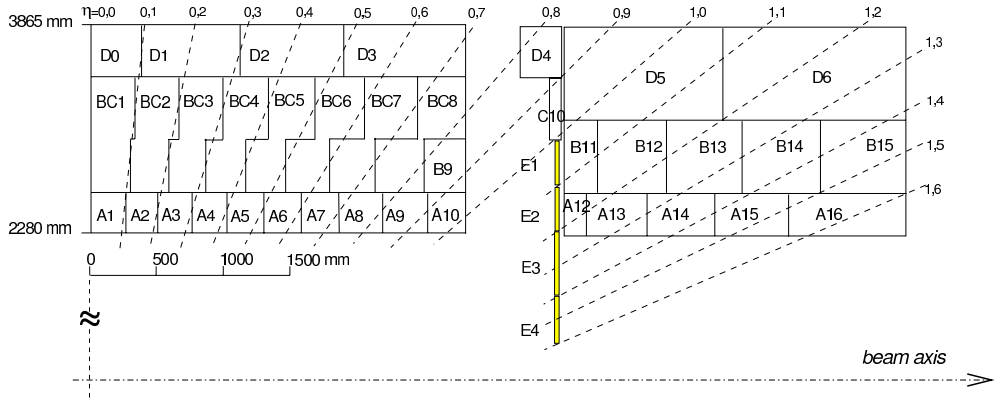


Figure 5.2: Schematic view of the TileCal layer and cell structure in a plane containing the beam axis  $z$  [27].

### 5.2.1 Signal Reconstruction

The TileCal cells are read out by two PMTs with the exception of the E layer cells that are connected to only one photomultiplier tube using [WSF](#). Each PMT is associated to an electronic read-out channel with its own shaper, preamplifier and [Analog to Digital Converter \(ADC\)](#). The current pulse from the PMTs is shaped and amplified by the 3-in-1 card. There are two possible gains: [High Gain \(HG\)](#) and [Low Gain \(LG\)](#), with an amplification ratio of 64. The 3-in-1 card forms the front-end electronics of the read-out chain and provides three basic functions: shaping of the pulse, charge injection calibration and slow integration of the PMT signals for monitoring and calibration [26]. Up to twelve 3-in-1 cards are serviced by a motherboard that provides power and individual control signals. The amplified signal is sent to two [ADCs](#) synchronous with the 40 MHz LHC clock thus sampling the signal every 25 ns. For optimization and efficiency reasons, 7 samples for each pulse are taken and sent to the [ReadOut Drivers \(RODs\)](#) if an L1 trigger accept is received.

### Optimal Filtering

The seven samples are used to reconstruct the amplitude of the pulse using the [Optimal Filtering \(OF\)](#) method. The estimate of the amplitude is given by:

$$\hat{A} = \sum_{i=0}^7 a_i S_i \quad (5.2.2)$$

where  $S_i$  are the digitized samples expressed in ADC counts and  $a_i$  are computed weights that minimize the effect of the electronic noise on the amplitude reconstruction. The procedure minimizes the variance of the amplitude distribution. In order to make the amplitude reconstruction independent from phase and signal baseline due to electronic noise (*pedestal*), the following constraints are used:

$$\sum_{i=0}^7 g_i a_i = 0 \quad (5.2.3)$$

$$\sum_{i=0}^7 g'_i a_i = 0 \quad (5.2.4)$$

$$\sum_{i=0}^7 a_i = 0 \quad (5.2.5)$$

where  $g_i$  and  $g'_i$  are the pulse shape function from the shaper and its derivative [28].

### The TileCal Calibration

The energy deposited in the calorimeter cell is proportional to the reconstructed amplitude. The amplitude is originally measured in ADC counts and needs to be converted in GeV for physics analysis using the formula:

$$E[GeV] = \hat{A}[ADC] \times C_{ADC \rightarrow pC} \times C_{laser} \times C_{Cs} \times C_{pC \rightarrow GeV} \quad (5.2.6)$$

where  $\hat{A}[ADC]$  is the amplitude estimate in ADC counts,  $C_{ADC \rightarrow pC}$  is determined using the [Charge Injection System \(CIS\)](#),  $C_{pC \rightarrow GeV}$  is measured during testbeam using electrons with a well defined energy and converts the deposited charge to energy in GeV, the laser system allows to determine the value of the  $C_{laser}$  constant while the Cesium sets the  $C_{Cs}$  factor.

The CIS calibrates the read out electronics by injecting a known charge and measuring the resulting response of the electronics. The *laser* system main purpose is to monitor the photomultipliers tubes stability and the downstream electronics. Well calibrated light pulses are sent to the PMTs and by reconstructing the signal it is possible to extract the PMTs' gain. The *cesium* system, circulates a Cs source through each scintillating tile using an hydraulic system, the PMTs signal is continuously read out through an integrator. The cesium system allows to equalize the calorimeter cell response to that measured during test beams. Figure 5.3 depicts a schematic representation of the ATLAS TileCal calibration chain.

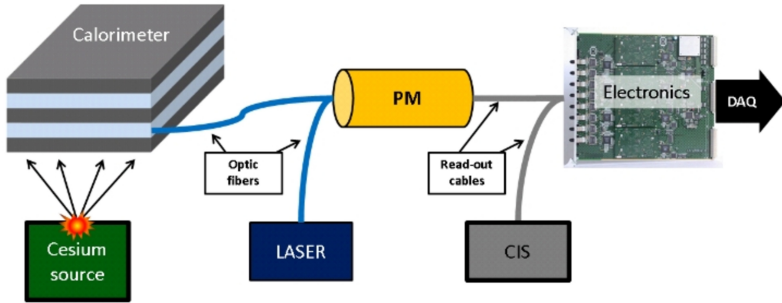


Figure 5.3: The ATLAS TileCal calibration chain [29].

### 5.2.2 Electronic Noise

TileCal periodically records sets of events (referred to as *runs*) with no signal in the PMTs, called *pedestal runs*. During these runs, each channel is read out using both, HG and LG for about 100000 events. These events are sampled every 25 ns in 7 samples as in normal physics runs and are normally distributed around a mean value called *pedestal*. The Root Mean Square (RMS) of the pedestal is the *noise*. Pedestal runs are used to calculate different parameters called *noise constants* that allow to describe the electronic noise. Two different sets of noise constants are computed: *Digital Noise* (or *Sample Noise*) and *Cell Noise*.

#### Digital Noise

The digital noise is measured in ADC counts for each PMT in both gains, HG and LG. The noise constants together with all detector conditions are stored in the [ATLAS Condition Database \(COOL\)](#). These constants are the RMS of the seven samples within each event, also called [High Frequency Noise \(HFN\)](#) and the RMS of the first digitized sample in each event or [Low Frequency Noise \(LFN\)](#). The digital noise is used for monitoring the electronics and for [Monte Carlo \(MC\)](#) noise simulation of the calorimeter response.

#### Cell Noise

Excluding the E layer cells that are connected only to one PMT, the cell noise is the combination of the two readout channels of a cell where the digital noise from the PMTs is added quadratically and converted in MeV using the calibration constants and eq. (5.2.6). There are four possible gain combinations: [High Gain – High Gain \(HGHG\)](#), [Low Gain – Low Gain \(LGLG\)](#), [Low Gain – High Gain \(LGHG\)](#) and [High Gain – Low Gain \(HGLG\)](#). When the energy deposit is large, the two channels belonging to the cell are readout in low gain thus giving rise to the LGLG combination, for small signals the HGHG combination is used. It can also occur that for energy deposits in the intermediate range, one PMT is readout in LG and the other in HG resulting in a HGLG combination. The cell noise is used to identify the seed cells in the topocluster algorithm (see Section 6.5).

Figure 5.4 shows a comparison between the cell noise and the fitted  $\sigma$  parameter of a normal distribution. The ratio  $\text{RMS} / \sigma = 1$  indicates a perfect agreement between the measured and the fitted amplitude distribution for a single Gaussian hypothesis.

The blue square in the plot indicate the comparison for an old model of [Low Voltage Power Supply \(LVPS\)](#) while the red square refers to the currently used LVPSs. It can be seen that with the old model of [LVPSs](#) the ratio RMS /  $\sigma$  can be large indicating a non Gaussian behavior of the electronic noise. For this reason a double Gaussian distribution is used to fit the energy distribution with the probability density function defined as:

$$f_{2g} = \frac{1}{1+R} \left( \frac{1}{\sqrt{2\pi}\sigma_1} e^{-\frac{x^2}{2\sigma_1^2}} + \frac{R}{\sqrt{2\pi}\sigma_2} e^{-\frac{x^2}{2\sigma_2^2}} \right) \quad (5.2.7)$$

where  $R$  is the relative normalization of the two Gaussians and  $\sigma_1, \sigma_2$  and  $R$  are independent parameters. These three are used to define the region  $\sigma_{\text{eff}}(E)$  where the significance for the double Gaussian is the same as the one  $\sigma$  region for a single Gaussian, i.e.  $\int_{-\sigma_{\text{eff}}}^{\sigma_{\text{eff}}} f_{2g} = 0.68$  [30]. In terms of  $\sigma_{\text{eff}}$ , for an energy deposit  $E$ , the significance can be expressed as:

$$\frac{E}{\sigma_{\text{eff}}(E)} = \sqrt{2} \operatorname{Erf}^{-1} \left( \frac{\sigma_1 \operatorname{Erf} \left( \frac{E}{\sqrt{2}\sigma_1} \right) + R\sigma_2 \operatorname{Erf} \left( \frac{E}{\sqrt{2}\sigma_2} \right)}{\sigma_1 + R\sigma_2} \right) \quad (5.2.8)$$

where  $\operatorname{Erf}$  is the error function. Equation 5.2.8 is the input to the calorimeter cell clustering algorithm discussed in more details in Section 6.5, moreover this definition allows to use the same unit to describe the noise for both the TileCal and LAr calorimeters. The region  $\sigma_{\text{eff}}(E)$  is commonly referred to as *cell noise* and together with the three double Gaussian parameters ( $\sigma_1$ ,  $\sigma_2$  and  $R$ ) is stored in the COOL database.

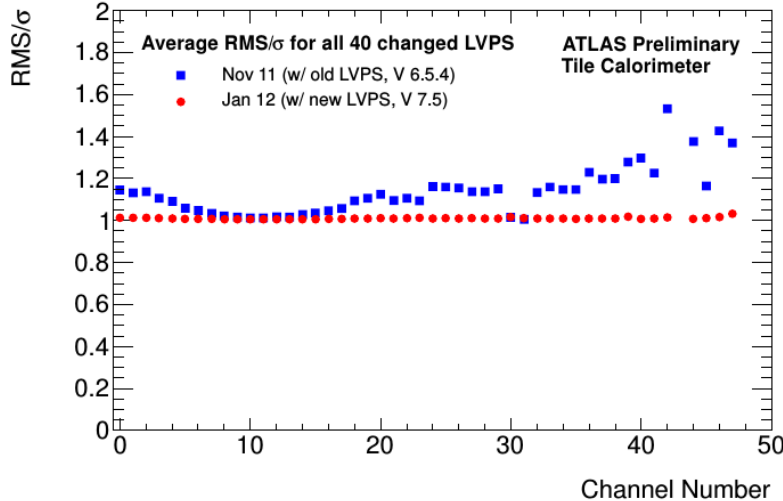


Figure 5.4: Comparison between the TileCal electronic noise, measured as the RMS of the reconstructed amplitude distribution in pedestal runs and the  $\sigma$  of the Gaussian fit of the distribution for the old and new LVPS [31].

### 5.3 The 2011 TileCal Run I Reprocessing

As new information about the detector becomes available, an update of the calibration constants and thus of the reconstructed energy must be performed; this procedure is

called *reprocessing*. In 2011 an update of the laser and cesium calibration analysis procedure were performed together with an update of which cells were considered good or bad. These updates required a recalculation of the cell noise.

### 5.3.1 Results

The cell noise for the reprocessed data has been calculated in different gain combinations. In Figures 5.5 to 5.7 the cell noise values have been calculated using all the calibration runs used for the 2011 RUN I reprocessing, each fitted using the optimal filtering method (see Section 5.2.1). The plots show the  $\eta$ -dependence of the  $\phi$ -averaged RMS of the noise in these runs. Each point is an average for a given cell over all modules containing this cell type. This is done for a given gain combination of the readout channels: High Gain–High Gain (Figure 5.5), Low Gain–Low Gain (Figure 5.6) or High Gain–Low Gain (Figure 5.7). The plots separate the different cell types: A, BC, D and E (gap and crack scintillators). Note that gap and crack scintillators have only one readout channel, so are plotted only in HG or LG read-out. The transition between the long and extended barrels can be seen in the range  $0.7 < |\eta| < 1.0$ .

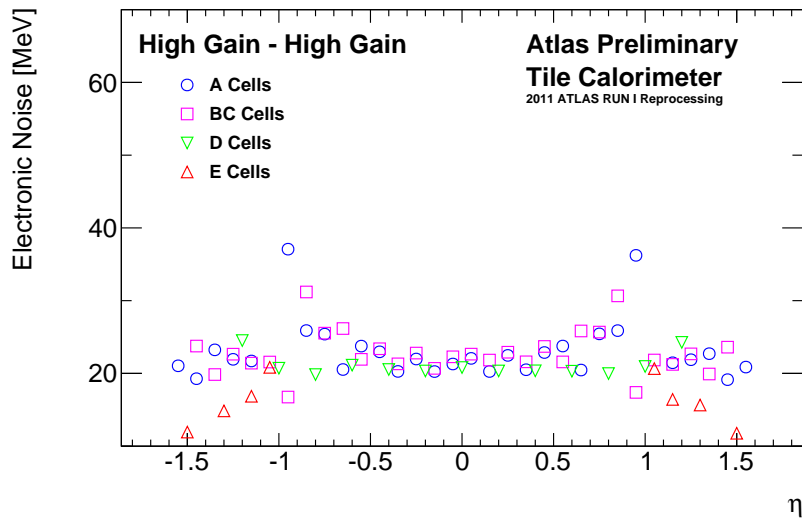


Figure 5.5:  $\phi$ -averaged RMS of electronic cell noise as a function of  $\eta$  of the cell, with both readout channels in High Gain. For each cell the average value over all modules is taken. Values have been extracted using all the calibration runs used for the 2011 RUN I reprocessing. The different cell types are shown separately, A, BC, D, and E (gap/crack). The transition between the long and extended barrels can be seen in the range  $0.7 < |\eta| < 1.0$ . HGHG combination is relevant when the energy deposition in the cell is  $\lesssim 15$  GeV [32].

Figures 5.5 to 5.7 exhibit some  $\eta$ -dependence of the noise. There are two main factors behind this, first the low voltage power supplies, which are the main noise source in TileCal, are located approximately at  $|\eta| \approx 1$  leading to higher noise in the cells in that region. Secondly the noise in these plots is in MeV, cells with the same noise expressed in ADC counts can have different noise levels when converted in MeV. This is due to the different ADC to GeV calibration factors for cells with different geometries.

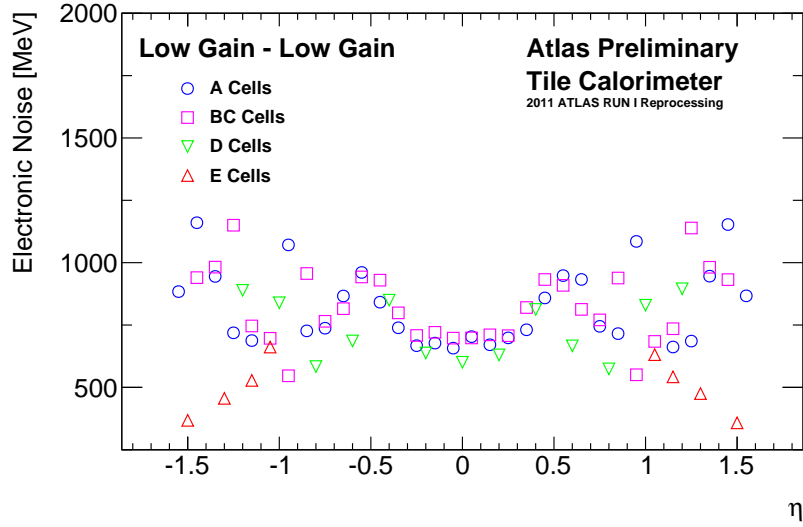


Figure 5.6:  $\phi$ -averaged RMS of electronic cell noise as a function of  $\eta$  of the cell, with both readout channels in Low Gain. For each cell the average value over all modules is taken. Values have been extracted using all the calibration runs used for the 2011 RUN I reprocessing. The different cell types are shown separately, A, BC, D, and E (gap/crack). The transition between the long and extended barrels can be seen in the range  $0.7 < |\eta| < 1.0$ . LGLG combination is relevant when the energy deposition in the cell is  $\gtrsim 15$  GeV [32].

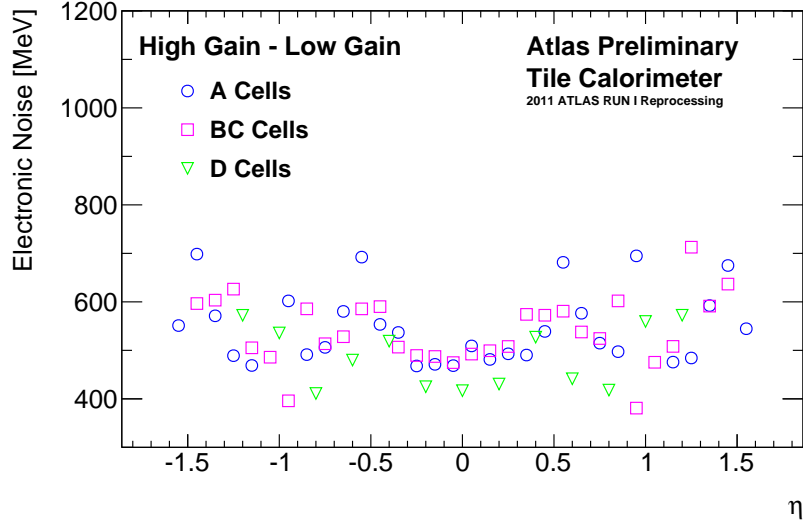


Figure 5.7:  $\phi$ -averaged RMS of electronic cell noise as a function of  $\eta$  of the cell, with one readout channel in High Gain and the other in Low Gain. For each cell the average value over all modules is taken. Values have been extracted using all the calibration runs used for the 2011 RUN I reprocessing. The different cell types are shown separately, A, BC, D. E cells do not appear in this plot since they have only one readout channel. The transition between the long and extended barrels can be seen in the range  $0.7 < |\eta| < 1.0$ . When the energy deposition in the cell is between  $10 \text{ GeV} \lesssim E \lesssim 20 \text{ GeV}$  it can happen that the cell is read out with different voltage on the readout channels [32].

## 5.4 Time Stability

The calibration constants used in Eq. (5.2.6), as mentioned in Section 5.2.1, are determined with the help of several dedicated calibration systems and runs. Each calibration constant is valid over a period of time called **Interval Of Validity (IOV)**. The cell noise can vary over time for several reasons such as a change in the calibration constants, a variation in the digital noise or the channel status in a particular run. Sudden variations in the noise must be checked and understood.

The different TileCal subsystems (laser, CIS, etc.) all use a common software framework, **TileCal Universal Calibration Software (TUCS)**, to perform validity checks on a number of different studies. To test the stability over time of the updated noise constants, a set of python scripts was developed by the author of this thesis to expand the TUCS functionality. These scripts connect to the ATLAS condition database and allow to visually display the relative change of the cell noise and digital noise constants, the channel status and the ratio between the cell noise and a variable called  $\text{RMS}_{\text{eff}}$  and defined as:

$$\text{RMS}_{\text{eff}} = \sqrt{(1 - R)\sigma_1^2 + R\sigma_2^2} \quad (5.4.1)$$

where  $\sigma_1$ ,  $\sigma_2$  and  $R$  are the free parameter in the double Gaussian model (see Section 5.2.2). The ratio  $\sigma / \text{RMS}_{\text{eff}}$ , where  $\sigma$  is the cell noise, can be used to test the goodness of the double Gaussian model: if  $\sigma / \text{RMS}_{\text{eff}}$  equals one, the double Gaussian well models the noise, if  $\sigma / \text{RMS}_{\text{eff}} > 1$ , it means that there is noise that is not well described by it.

Figure 5.8 shows the time evolution plot over the entire reprocessed period for two representative TileCal cells. This represents the typical behavior for most cells over the reprocessing period.

In Figure 5.8a it can be seen that cell number 2 in the BC layer (BC2) of the 41st module in the C side of LB (LBC 41) is stable over several pedestal runs. In Figure 5.8b on the other hand, it is possible to see a variation in the cell noise and of the  $\sigma / \text{RMS}_{\text{eff}}$  without a corresponding variation in the calibration, in the digital noise constants or in the channel status. The term *jump* is used in the following to indicate a variation in the cell noise not compatible with a change in the other quantities.

This problem was investigated by re-performing the pedestal noise fit manually and recalculating the noise constants focusing on two specific IOVs, [183110, 183382[ (before the jump) and [183382, 183515[ (after the jump). Some calorimeter cells without jump were used to validate the noise constants calculated with the fit and checked against the values stored in COOL from automated fits performed by the standard ATLAS software.

Figure 5.9 shows the control cell energy distribution with the double Gaussian fit superimposed for two runs where the jump was present in other cells. The results of the fit and the values stored in the COOL database, both reported in Table 5.1, are in good agreement.

Moving to the investigation of a cell which exhibit the jump in the time evolution the seventh cell of the BC layer (BC7) on the C side of the LB partition of the 41st module (LBC 41) was selected for illustration purposes. Figure 5.10 shows the energy distribution with the double Gaussian fit superimposed. The cell had the jump under investigation (see Figure 5.8) and this is reflected in the fit results reported in Table 5.2 together with the values from the database.

Also in this case, the noise constants from the fit, are in agreement with those stored in the COOL database. From this study it was concluded that bad fits inside

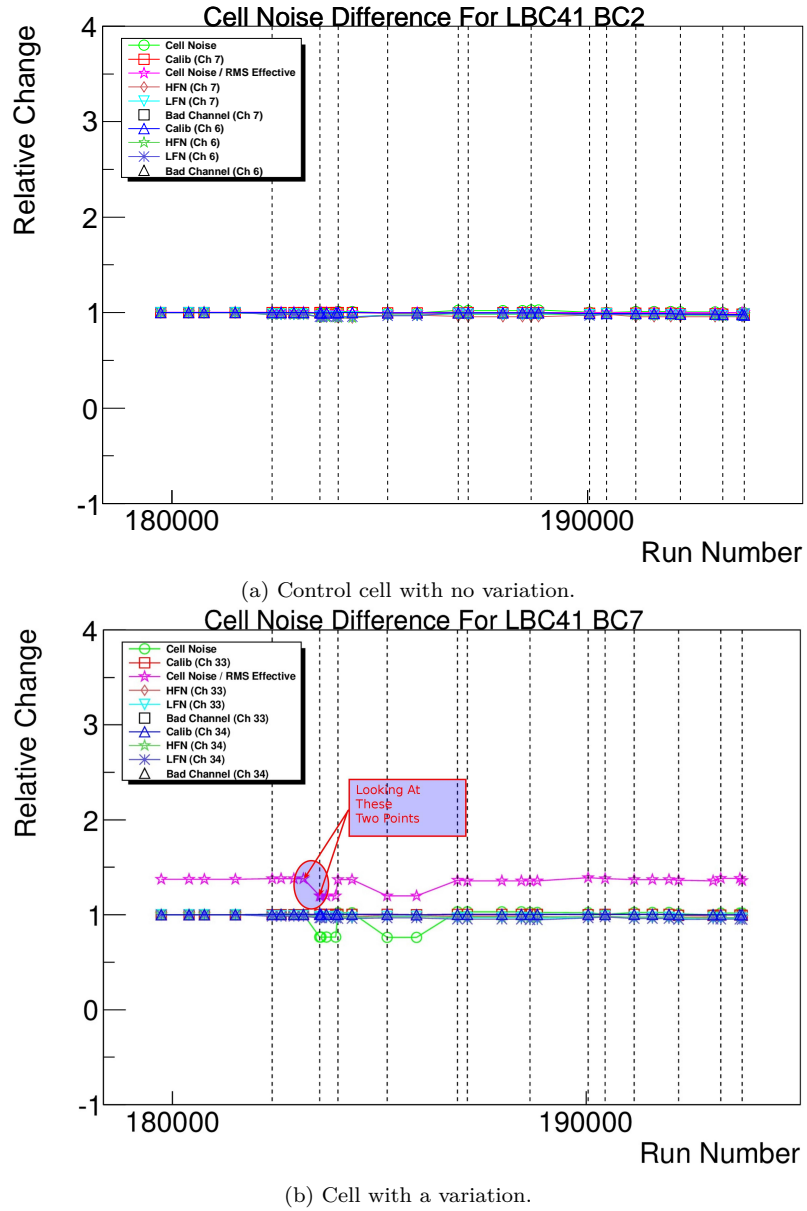


Figure 5.8: Time evolution for two different representative cells in the calorimeter over the entire reprocessing period. The plot shows the change relative to the first run considered for several quantities for different IOVs (vertical dashed lines). If a channel is off due to some problems (Bad channel), this is reported in the plot with a black square.

the automated ATLAS pedestal and noise reconstruction were not the cause of the jumps. However, the  $\chi^2$  of the distribution imply that the double Gaussian model is not a good model in this case.

After further investigations it was discovered that this behavior is caused by the [Tile Noise Filter \(TNF\)](#). The electronic noise in nearby channels can be correlated. The version of low voltage power supplies that were used during the 2011 data taking

LBC41 BC2 Values Before Jump			LBC41 BC2 Values After Jump		
	Database	Fit		Database	Fit
$\sigma_1$ :	19.97	$20.08 \pm 0.05$	$\sigma_1$ :	19.94	$20.05 \pm 0.05$
$\sigma_2$ :	80.59	$77.3 \pm 9$	$\sigma_2$ :	71.41	$71.39 \pm 10.51$
R:	0.00026	$0.0003 \pm 0.0012$	R:	0.00023	$0.0002 \pm 0.0011$

Table 5.1: The table reports the comparison between the double Gaussian parameters stored in the COOL database and those obtained from the fit for two different run numbers corresponding to before and after the jump for a cell where there is no variation in the cell noise.

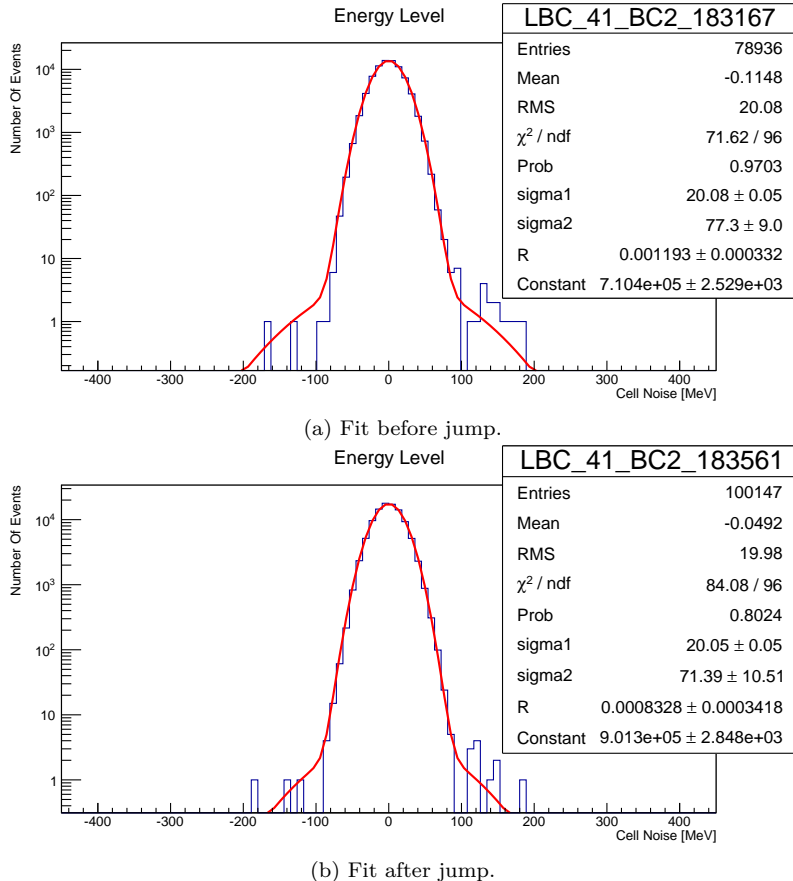


Figure 5.9: Fit of the reconstructed pulse shape on a control cell with no variation (jump) in the cell noise.

lead to significant coherent noise among several channels, particularly those close to the power supply, see Figure 5.4. Coherent noise means that the signal in several cells can vary coherently and can thus alter the jet and missing transverse energy reconstruction. In order to remedy this a Tile Noise Filter was employed. The TNF calculates for each motherboard the pedestal average:

$$d = \frac{\sum_i^N d_i}{N} \quad (5.4.2)$$

LBC41 BC7 Values Before Jump			LBC41 BC7 Values After Jump		
	Database	Fit		Database	Fit
$\sigma_1$ :	24.25	$23.56 \pm 0.1$	$\sigma_1$ :	24.42	$24.4 \pm 0.1$
$\sigma_2$ :	99.16	$98.36 \pm 0.9$	$\sigma_2$ :	94.56	$94.55 \pm 1.34$
R:	0.037	$0.042 \pm 0.036$	R:	0.014	$0.014 \pm 0.015$

Table 5.2: The table reports the comparison between the double Gaussian parameters stored in the COOL database and those obtained from the fit for two different run numbers corresponding to before and after the jump for a cell where a variation in the cell noise was spotted.

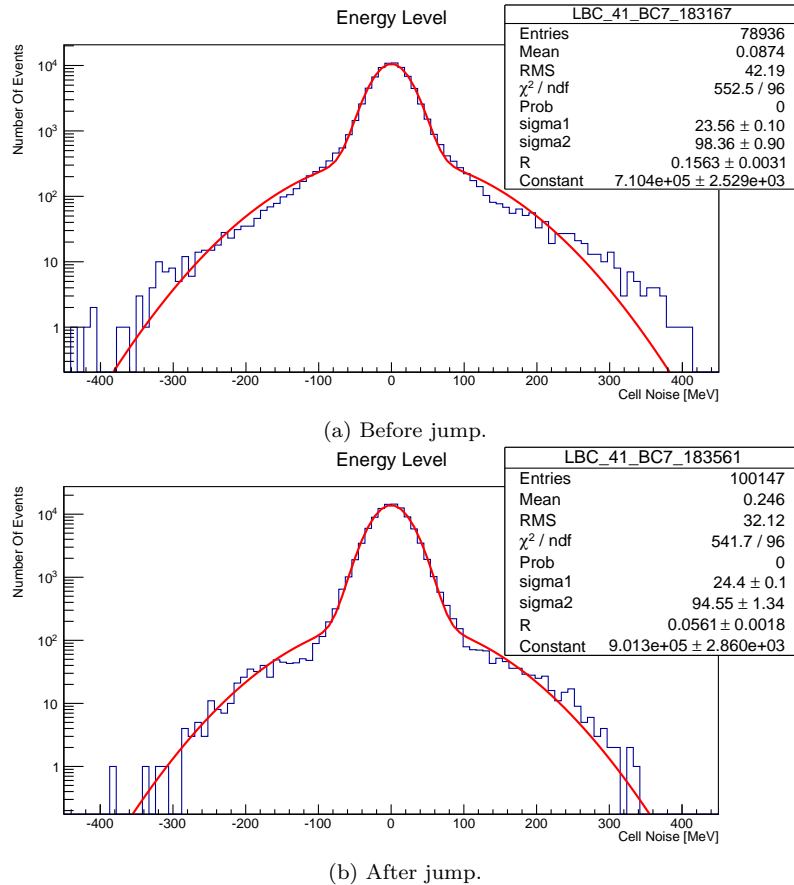


Figure 5.10: Fit of the reconstructed pulse shape on a cell with variation (jump) in the cell noise non compatible with a change in the calibration, digital noise or channel status.

where the index  $i$  runs over all the channels belonging to a certain motherboard,  $d_i$  is the  $i$ -th channel amplitude in ADC counts and  $N$  is the number of channels. Variations in this average baseline can be regarded as an estimation of the coherent noise and is subtracted from the channel data of each channel ( $d_i - d$ ) on an event-by-event basis.

The cell noise was recalculated without noise filter and the corresponding distribution re-fitted. Figure 5.11 show the double Gaussian fit applied to another cell where the jump was present, in Figures 5.11a and 5.11b the noise filter is on while in

Figures 5.11c and 5.11d the TNF was removed. It can be seen that the fit improves when there is no noise filter. This shows that the noise jump arises from bad fits when the TNF is somehow malfunctioning and transforms a double Gaussian distribution into a distribution with more complicated shape.

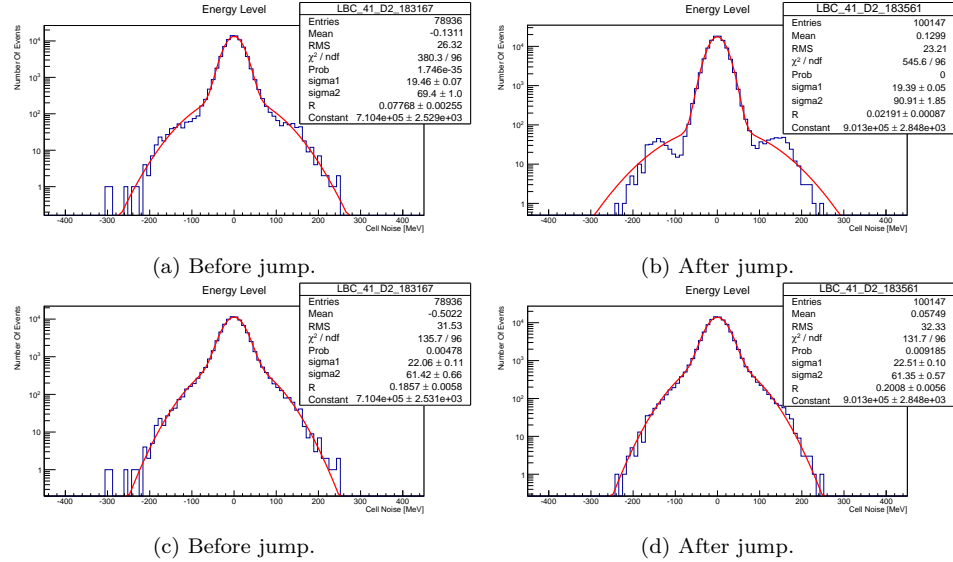


Figure 5.11: Comparison of the reconstructed pulse shape of a cell with the cell noise variation without a corresponding variation in he calibration constants, digital noise or channel status (jump) with the double Gaussian fit superimposed with the noise filter (Figures 5.11a and 5.11b) and without noise filter (Figures 5.11c and 5.11d).

## 5.5 Conclusions

In 2013 the ATLAS 2011 data was reprocessed with improved algorithms and calibrations. In TileCal the methods to produce Cs and laser calibration constants were improved and required a re-computation of the TileCal noise constants. Changing the calibration constants, according to Eq. (5.2.6), changes the reconstructed energy in the cell thus affecting the jet identification (see Section 6.5). A comparison between the  $\phi$ -averaged RMS of electronic cell noise as a function of  $\eta$  of the cell before and after reprocessing for the high statistic run 192130 with both channels in high gain is shown in Figure 5.12. There is a general increase of the cell noise of about 0.5% in the EBC, LBC and EBA partitions. The LBA partition had module 22 running in *emergency mode*, i.e. operated with  $\sim 50$  V less high voltage on the PMTs, and had the cesium calibration constants updated. This change is likely to have lowered the average noise in this partition.

The change of the cell noise between IOVs was monitored using a special software within the TUCS environment. A problem with the TNF has been identified in cells which exhibits a variation in the cell noise without a corresponding variation in other relevant quantities were present. The number of cells affected by this problem is investigated constructing the distribution of the ratio  $\sigma / \text{RMS}_{\text{eff}}$  shown in Figure 5.13. The bulk of the distribution have  $\sigma / \text{RMS}_{\text{eff}}$  close to one, this corresponds to cells for which the double Gaussian noise is a good model. There is nevertheless a big tail

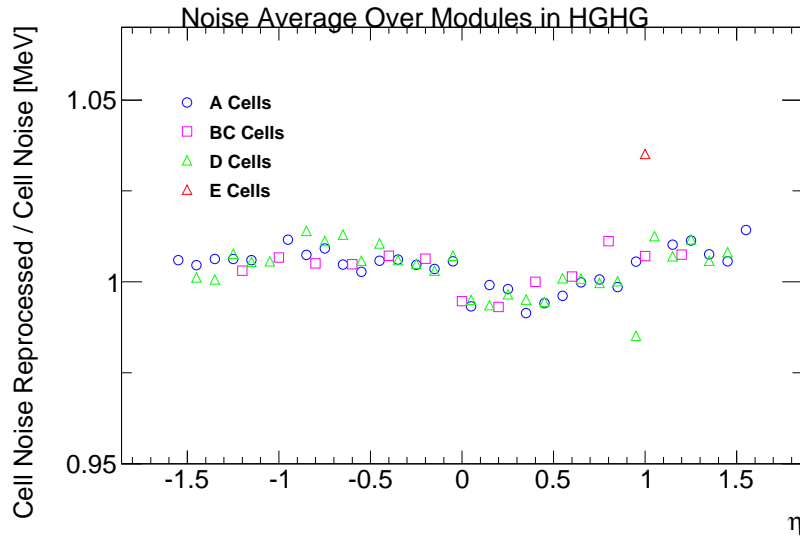


Figure 5.12: Comparison between the  $\phi$ -averaged RMS of electronic cell noise as a function of  $\eta$  of the cell before and after reprocessing for the high statistic 192130 run with both channels in high gain. The different layers are shown separately, A, BC, D and E (gap/crack). The transition between the long and extended barrels can be seen in the range  $0.7 < |\eta| < 1.0$ .

of cells with  $\sigma / \text{RMS}_{\text{eff}}$  up to 1.7, with about 5% of the cells with  $\sigma / \text{RMS}_{\text{eff}}$  larger than 1.2. After the installation of the new LVPS the contribution from a second wider Gaussian to the electronic noise is much smaller and the effect of the TNF is expected to be smaller as well. However the effect of the TNF with the new power supplies remains to be checked.

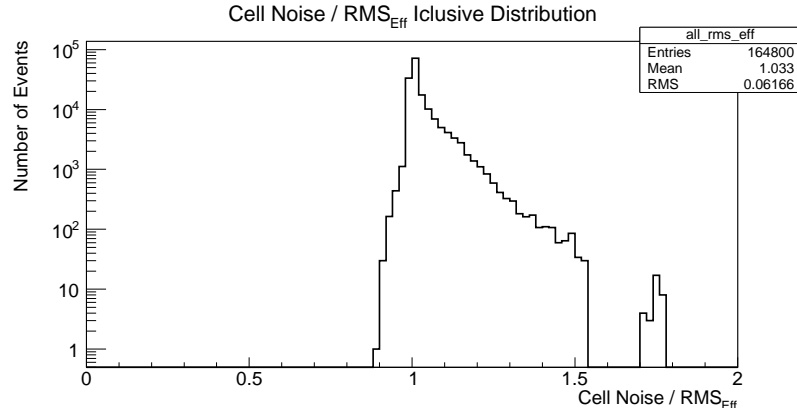


Figure 5.13: Distribution of the ratio  $\sigma / \text{RMS}_{\text{eff}}$  where the  $\sigma$  and  $\text{RMS}_{\text{eff}}$  values are taken from all IOVs considered for the 2011 TileCal reprocessing.



# Chapter 6

# Physical Objects Reconstruction

Object reconstruction is the process that associates the signal left in the detector by charged particles to physical objects through a series of algorithms. This analysis uses electrons, muons, jets and missing transverse momentum ( $E_T^{\text{miss}}$ ). Two types of electrons, muons and jets are also defined: *baseline* and *good*, where the former one is used for removal of overlapping objects and preselection while the latter for selecting the objects used to define the signal and control regions. In the following a brief introduction to the identification criteria of these objects is presented.

## 6.1 Primary Vertex

In  $pp$  collisions with high luminosity, multiple interactions occur on a given bunch crossing, the spatial location of the collision is called **Primary Vertex (PV)**, the one that has the highest  $\sum p_T^2$  of constituent tracks is known as **Hard Scatter (HS)** vertex, the rest are called *pile-up vertices*. The reconstruction of the PV generally happens in two stages that are often not distinguishable from each other. The *vertex finding* associates reconstructed tracks to a particular vertex candidate and the *vertex fitting* reconstructs the actual vertex position, refits the tracks and estimates the quality of the fit [33].

In the current analysis, events are required to have at least one PV with two associated tracks.

## 6.2 Track reconstruction

Charged particles that move through the solenoidal magnetic field that surrounds the ATLAS tracking system, follow helical trajectories. The projection of a helix on the  $xy$  plane is a circle and, in order to uniquely parametrize the particle track in three dimensions, five parameters are needed. A common choice is to use the *perigee* parameters, where the perigee is the point of closest approach to the beam axis. With this choice, the five parameters are:

- The signed curvature  $C$  of the helix, defined as  $C = q/2R$  where  $q$  is the particle charge and  $R$  is the radius of the helix. This is related to the transverse

momentum  $p_T = qB/C$ , where  $B$  is the magnetic field measured in Tesla,  $C$  is measured in  $\text{m}^{-1}$  and  $p_T$  in GeV.

- The distance of closest approach  $d_0$  in the  $xy$  plane measured in millimeter.
- The  $z$  coordinate of the point of closest approach, denoted by  $z_0$  and measured in millimeters.
- The azimuthal angle  $\phi_0$  of the tangent to this point.
- The polar angle  $\theta$  to the  $z$ -axis.

The perigee and the track parameters are schematized in Figure 6.1.

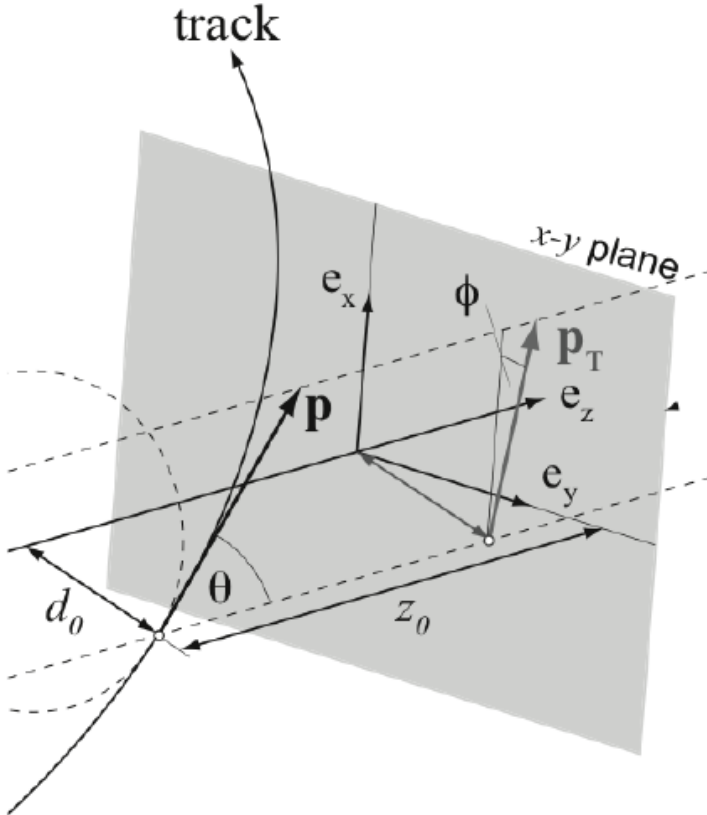


Figure 6.1: Track parameters at the perigee. In the figure  $\mathbf{p}$  is the momentum of the incoming particle,  $e_x$ ,  $e_y$ ,  $e_z$  are the versors of the coordinate system defined in Section 4.2.1 and  $\theta$  and  $\phi$ , also defined in Section 4.2.1 are the polar and azimuthal angle respectively.

### 6.3 Electrons

Electrons are identified in the central part of the ATLAS detector ( $|\eta| < 2.47$ ) by an energy deposit in the electromagnetic calorimeter and an associated track in the inner detector. Signal electrons are defined as prompt electrons coming from the decay of a  $W, Z$  boson or a top quark while background non-prompt electrons come from

hadron decays, photon conversion, semi-leptonic heavy flavor hadron decay and highly electromagnetic jets. A likelihood discriminant is formed using different information: the shower shape in the EM calorimeter, the track-cluster matching, some of the track quality distributions from signal and background simulation and cuts on the number of hits in the ID. Cuts that depends on  $|\eta|$  and  $E_T$  on the likelihood estimator allow to distinguish between signal and background electrons.

Electron identification efficiencies are measured in  $pp$  collision data and compared to efficiencies measured in  $Z \rightarrow ee$  simulations. Signal electrons can furthermore be selected with different sets of cuts for the likelihood-based criteria with  $\sim 95\%$ ,  $\sim 90\%$  and  $\sim 80\%$  efficiency for electrons with  $p_T = 40$  GeV. The different criteria are referred to as *loose*, *medium* and *tight* operating points respectively [34] where, for example, the tight criterion leads to a higher purity of signal electrons but has a lower efficiency than the looser criteria.

In this analysis, the *baseline electrons* are selected requiring a transverse energy  $E_T > 20$  GeV,  $|\eta| < 2.47$ , they need to satisfy the *loose* likelihood selection criteria, it is required that no dead EM calorimeter **Front–End Board (FEB)** or **High Voltage (HV)** channels in the calorimeter cluster are present and that the baseline electron survives the overlap removal with other particles as described in Section 6.7. The baseline electron criteria is used to veto electrons used in the muon control regions and the signal region definition. In addition to all the baseline criteria, the *good electron* definition requires the electrons to satisfy the *tight* likelihood selection criteria, the electron track  $d_0/\sigma_{d0} < 5$  and  $|z_0| < 0.5$  mm and the *LooseTrackOnly* electron isolation criteria which is based only on tracks and is 99% efficient.

Electron Definition	
Baseline electron	Good electron
$E_T > 20$ GeV	<i>baseline</i>
$ \eta  < 2.47$	<i>tight</i> working point
<i>loose</i> working point	$d_0/\sigma_{d0} < 5$
No dead FEB in the EM calo cluster	$ z_0  < 0.5$ mm
No dead HV in the EM calo cluster	<i>LooseTrackOnly</i>
passes the overlap removal	

Table 6.1: Electron definition for the monojet analysis.

## 6.4 Muons

Muons are identified using different criteria from the information provided by the ID and the MS leading to four different types of muons. The **Standalone (SA)** muons use only the MS information to reconstruct the muon’s trajectory; the **Combined (CB)**, where the track is independently reconstructed in the ID and the MS and then combined; the **Segment Tagged (ST)** are identified as muons only if the track in the ID is, after being extrapolated to the MS, associated to at least one local track segment in the MDT or CSC chambers and finally the **Calorimeter Tagged (CT)** where tracks in the ID are associated to an energy deposit in the calorimeter compatible with a minimum ionizing particle. CB candidates perform best in terms of muon purity and momentum resolution.

Muons are identified using quality requirements specific to each of the four type of muons aiming at rejecting those coming from pion and kaon decays and guarantee a robust momentum measurement. The *loose* identification criteria maximize the reconstruction efficiency and provide good muon tracks; the *medium* criteria minimize the systematic uncertainties associated to muon reconstruction and calibration; the *tight* muons maximize the purity of the sample and the *high  $p_T$*  selection maximize the momentum resolution for tracks with transverse momenta above 100 GeV [35].

This analysis uses the CB muons that pass the medium identification criteria, moreover the *baseline muons* are required to have  $p_T > 10$  GeV and  $|\eta| < 2.5$ , the  $E_T^{\text{miss}}$  definition and in the lepton veto used to define the signal and control regions. The *good muons* are required to pass the baseline selection criteria, moreover  $d_0/\sigma_{d0} < 3$ ,  $|z_0 \sin \theta| < 0.5$  mm. The good muons are used in the one muon and di-muon control regions.

Muon Definition	
Baseline muon	Good muon
CB muon	<i>baseline</i>
<i>Medium</i> id. criteria	$d_0/\sigma_{d0} < 3$
$p_T > 10$ GeV	$ z_0 \sin \theta  < 0.5$ mm
$ \eta  < 2.5$	
passes the overlap removal	

Table 6.2: Muon definitions for the monojet analysis.

## 6.5 Topocluster

The cell noise described in Section 5.2.2 is used in the *topological clustering* algorithm [36], for identification of the real energy deposits in the calorimeters. The algorithm assumes that the noise in all the calorimeter cells is normally distributed with significance (the ratio between the deposited energy and the parameter  $\sigma$  used to describe the cell noise) expressed in units of Gaussian sigmas. In the algorithm, cluster of cells called *topoclusters*, are formed by comparing the energy deposit in a cell for a significant incompatibility with a noise only hypothesis. The algorithm starts by finding the *seed cells* with  $E > 4\sigma$  where  $\sigma$  is the measured RMS of the energy distribution for every cell in the pedestal run. The second step is to add to the seeds neighbor cells that satisfy the  $E > 2\sigma$  condition. Finally an additional level of cells with  $E > 0$  is added to the perimeter of the cluster and the algorithm is ended. At this point the splitting algorithm is applied to separate the topoclusters based on the local energy maxima.

## 6.6 Jets

The quarks and gluons that carry color charge and are created in the scattering process, hadronize producing collimated bunches of colorless hadrons (jets) which keep track of the energy and direction of the originating parton. Jets in ATLAS are reconstructed as massless particles using the *anti- $k_t$*  algorithm, calibrated and corrected for pile-up contamination. These steps are briefly outlined in the next sections.

### 6.6.1 The $\text{anti-}k_t$ Algorithm

The  $\text{anti-}k_t$  algorithm is a sequential recombination algorithm. It defines two distances  $d_{ij}$  and  $d_{iB}$ . The distance  $d_{ij}$  between the physical objects  $i$  and  $j$  is defined as:

$$d_{ij} = \min(k_{ti}^{-2}, k_{tj}^{-2}) \frac{\Delta_{ij}^2}{R^2} \quad (6.6.1)$$

where  $\Delta_{ij}^2 = (\eta_i - \eta_j)^2 + (\phi_i^2 - \phi_j^2)$  and  $\eta_i$  is the rapidity,  $\phi_i$  is the azimuthal angle,  $k_{ti}$  is the transverse momentum of the object  $i$  and  $R$  is the radius parameter that controls the size of the jet. The distance  $d_{iB}$  between the object  $i$  and the beam (B) defined as:

$$d_{iB} = k_{ti}^{-2}. \quad (6.6.2)$$

This distance is meant to distinguish between hard and soft terms. The algorithm identifies the smallest of the two distances and, if it is  $d_{ij}$ , it recombines the  $i$  and  $j$  objects while if it is  $d_{iB}$ , it calls  $i$  a jet and removes it from the list of inputs to the algorithm. The distances are recalculated and the procedure reiterated until there are no more objects [37].

### 6.6.2 The Jet Vertex Tagger

The excess transverse energy coming from pile-up jets is generally subtracted on average from the signal energy, however, due to localized fluctuations in the pile-up, some of it remains in the  $p_T$  of the reconstructed jet. The [Jet Vertex Fraction \(JVF\)](#) is a variable that uses information from the track associated to each jet to identify the origin vertex of each jet and rejects it if not coming from a hard-scatter vertex [38]. The JVF can be regarded as a measure of the fraction of the jet momentum associated with a primary vertex and is defined as:

$$\text{JVF} = \frac{\sum_k p_T^{\text{trk}_k}(\text{PV}_0)}{\sum_l p_T^{\text{trk}_l}(\text{PV}_0) + \sum_{n \geq l} \sum_k p_T^{\text{trk}_l}(\text{PV}_n)} \quad (6.6.3)$$

where  $\text{PV}_0$  is the hard scatter vertex and  $\text{PV}_n$  with  $n \geq 1$  is any other pile-up PV in the same bunch crossing thus  $\sum_k p_T^{\text{trk}_k}(\text{PV}_0)$  is the scalar  $p_T$  sum of the tracks associated with the jet and originating from the hard scatter vertex while  $\sum_{n \geq l} \sum_k p_T^{\text{trk}_l}(\text{PV}_n)$  is the scalar  $p_T$  sum of the tracks associated with the pile-up vertexes.

Since the JVF denominator increases with the number of reconstructed PV, this introduces a pile-up dependence on the number of PV when minimal JVF selections are imposed in rejecting pile-up jets. To address this problem, two new variables to separate from [HS](#) and [Pile Up \(PU\)](#) jets are introduced: corrJVF and  $R_{pT}$ . The former is defined as:

$$\text{corrJVF} = \frac{p_T^{\text{HS}}}{p_T^{\text{HS}} + p_T^{\text{PU,corr}}} \quad (6.6.4)$$

where  $p_T^{\text{HS}} = \sum_k p_T^{\text{trk}_k}(\text{PV}_0)$  is the scalar sum of the  $p_T$  of the tracks associated with the jet that comes from the hard scatter vertex and  $p_T^{\text{PU,corr}} = \sum_{n \geq l} \sum_k p_T^{\text{trk}_l}(\text{PV}_n)/(kn_{\text{trk}}^{\text{PU}})$  is the scalar sum of the associated tracks originating from a pile-up vertex. Since the average  $p_T^{\text{PU}}$  increases linearly with the number of pile-up tracks,  $n_{\text{trk}}$ ,  $p_T^{\text{PU}}$  is divided by  $(kn_{\text{trk}}^{\text{PU}})$  where  $k = 0.01$  is the slope of the  $\langle p_T^{\text{PU}} \rangle$  dependence with  $n_{\text{trk}}$  [39]. The corrJVF corrects the  $N_{\text{PV}}$  dependence in the JVF denominator.

Finally the quantity  $R_{pT}$  is defined for each jet as:

$$R_{pT} = \frac{\sum_k p_T^{\text{trk}_k}(PV_0)}{p_T^{\text{jet}}} \quad (6.6.5)$$

where  $p_T^{\text{jet}}$  is the fully calibrated jet  $p_T$ . This variable is defined using tracks associated with the vertex, it is at first order independent on the  $N_{PV}$  [40].

The **Jet Vertex Tagger (JVT)** is constructed from the corrJVF and  $R_{pT}$  by forming a two dimensional likelihood based on the k-nearest neighbor algorithm. Using the JVT algorithm, the HS jet efficiency is stable within 1% up to 35 interactions per bunch crossing [39].

### 6.6.3 Jet Calibration

The **Jet Energy Scale (JES)** relates the energy measured by the ATLAS detector to the kinematic properties of the corresponding stable particles, this calibration must take into account the detector effects such as the non compensating nature of the ATLAS hadronic calorimeter (see Section 5.1.2), energy loss due to inactive regions in the detector or particle showers not fully contained in the calorimeter. The energy deposited by electromagnetic shower is the baseline energy scale of the calorimeter and is established during test beam measurements with electrons. The basic jet calibration scheme, applies JES correction to the EM scale and is usually referred to as EM+JES. The **Local Cluster Weighting (LCW)** is another calibration method that clusters topologically connected cells, classifying them as electromagnetic or hadronic and deriving the energy corrections from single pion MC simulation and dedicated studies to account for the detector effects, the jets calibrated with this method are referred to as LCW+JES. The **Global Cell Weighting (GCW)** calibration uses the fact that electromagnetic and hadronic showers leave a different energy deposition in the calorimeter cells, with the electromagnetic shower more compact than the hadronic one. The energy correction are then derived for each calorimeter cell within the jet and minimizing the energy resolution. The **Global Sequential (GS)** method starts from EM+JES calibrated jets and corrects for the fluctuation in particle content of the hadronic shower using the topology of the energy deposits. The corrections are applied in a way that leaves unchanged the mean jet energy [42].

### 6.6.4 Jet Selection

In order to distinguish jets coming from  $pp$  collisions from those from a non-collision origin, two jet selection criteria, *loose* and *tight*, are available. The loose selection criteria, provides an efficiency for selecting jets coming from  $pp$  collisions above 99.5% for  $p_T > 20$  GeV, the tight criteria can reject even further background jets [43].

In this analysis the jets are reconstructed using the anti- $k_t$  algorithm with the radius parameter  $R = 0.4$ . The *baseline jets* are required to have  $|\eta| < 2.8$  and to make sure they come from a HS vertex, they need to satisfy any of the following:

- The  $p_T > 50$  GeV.
- They have  $20 < p_T < 50$  GeV and  $|\eta| > 2.4$ .
- they have  $20 < p_T < 50$  GeV,  $|\eta| < 2.4$  and  $\text{JVT} > 0.64$ .

Furthermore, events in which the jets, after the overlap removal is applied, fail the loose selection criteria are disregarded. Finally the most energetic jet in the event (the *leading jet*) is required to pass the tight selection criteria. The *good jets* require an increased  $p_T$  threshold of 30 GeV and at most 4 HS jet in the event.

Jet Definition	
Baseline jet	Good jet
$R = 0.4$	<i>baseline</i>
$ \eta  < 2.8$	at most 4 jets
<i>Loose</i> selection criteria	$p_T > 30$ GeV
<i>Tight</i> on the leading jet	
passes the overlap removal	
any of:	
• $p_T > 50$ GeV	
• $20 < p_T < 50$ GeV, $ \eta  > 2.4$	
• $20 < p_T < 50$ GeV, $ \eta  < 2.4$ , $JVT > 0.64$	

Table 6.3: Jet definition in the monojet analysis.

## 6.7 Overlap Removal

During object reconstruction, it may happen that different algorithms identify the same track and cluster as different types of particles, this results in a duplicate object. In physics analyses a decision must be made on which interpretation to give to the reconstructed object, this process is called **Overlap Removal (OR)** [44].

In this analysis, an overlap removal is applied to electrons, muons and jets that pass the baseline criteria and the following objects are removed:

- Remove jet in case any pair of jet and electron satisfies  $\Delta R(j, e) < 0.2$ .
- Remove electron in case any pair of jet and electron satisfies  $0.2 < \Delta R(j, e) < 0.4$ .
- Remove muon in case any pair of muon and jet with at least 3 tracks satisfies  $\Delta R(j, \mu) < 0.4$ .
- Remove jet if any pair of muon and jet with less than 3 tracks satisfies  $\Delta R(j, \mu) < 0.4$ .

## 6.8 Missing Transverse Energy

Due to the conservation of momentum and the fact that the proton bunches are parallel to the  $z$ -axis, the sum of the momenta of the collision products in the transverse plane should sum to zero. Any energy imbalance is known as **missing transverse momentum ( $E_T^{\text{miss}}$ )**, it may indicate weakly interacting stable particles (neutrinos within the SM, new particles in beyond SM models) or non reconstructed physical objects that escape the detector acceptance like for example jets with  $p_T < 20$  GeV. Physical objects that are fully reconstructed and calibrated such as electrons, photons, hadronically decaying tau-leptons, jets or muons are called *hard objects* and are used to compute

the missing transverse momentum in an event [45]. The  $x$  and  $y$  components of the  $E_T^{\text{miss}}$  can be written as:

$$E_{x(y)}^{\text{miss}} = E_{x(y)}^{\text{miss}, e} + E_{x(y)}^{\text{miss}, \gamma} + E_{x(y)}^{\text{miss}, \tau} + E_{x(y)}^{\text{miss, jets}} + E_{x(y)}^{\text{miss}, \mu} + E_{x(y)}^{\text{miss, soft}} \quad (6.8.1)$$

where the terms for jets, charged leptons and photons are the negative sum of the momenta of the respective calibrated object while the *soft term* is reconstructed from the transverse momentum deposited in the detector that is not already associated to hard objects. It may be reconstructed by means of calorimeter-based methods, the so called [Calorimeter Soft Term \(CST\)](#), or using track-based methods known as [Track Soft Term \(TST\)](#).

The CST is reconstructed using energy deposits in the calorimeters which are not associated to hard objects, it arise from soft radiation accompanying the hard scatter event and from underlying event activity. A downside of the CST is its vulnerability to pile up.

The TST is built from tracks not associated to any hard object, tracks can be associated to vertices and thus to a particular  $pp$  collision, making this method robust against pile-up. This method is, however, insensitive to soft terms coming from neutral particles that do not leave a track in the ID, thus the TST  $E_T^{\text{miss}}$  is combined with calorimeter-based measurements for hard objects.

Due to its stability against pile-up, this analysis uses the TST  $E_T^{\text{miss}}$  term. Moreover, the muons are treated as invisible particles in the  $E_T^{\text{miss}}$  reconstruction (i.e.  $E_{x(y)}^{\text{miss}, \mu} = 0$ ).

# Chapter 7

## The Monojet Signature

### 7.1 Motivation

There are two possible cases that results in an energy imbalance in the detector, the first one occurs in beyond Standard Model physics, that often involves the presence of particles that interact weakly or not at all with normal matter. These particles are not detected thus leaving an energy imbalance in the detector. In the second case, the decay products in the final state involve neutrinos that are not detectable by ATLAS. To better understand this second category of events, consider Figure 7.1a that shows the decay topology of squark pair production with a neutralino and two jets in the final state. Using the two body decay energy and momentum relations [11]:

$$E_q = \frac{M_{\tilde{q}}^2 - m_{\tilde{\chi}_1^0}^2 + m_q^2}{2M_{\tilde{q}}}, \quad (7.1.1)$$

$$|\vec{p}_q| = |\vec{p}_{\tilde{\chi}_1^0}| = \frac{\left[ (M_{\tilde{q}}^2 - (m_q + m_{\tilde{\chi}_1^0})^2) (M_{\tilde{q}}^2 - (m_q - m_{\tilde{\chi}_1^0})^2) \right]^{1/2}}{2M_{\tilde{q}}} \quad (7.1.2)$$

where  $M_{\tilde{q}}$  is the squark center of mass energy,  $m_{\tilde{\chi}_1^0}$  is the neutralino mass and  $m_q$  is the quark mass. Neglecting the quark mass ( $m_q = 0$ ) we get that:

$$E_q = \frac{M_{\tilde{q}}^2 - m_{\tilde{\chi}_1^0}^2}{2M_{\tilde{q}}}, \quad (7.1.3)$$

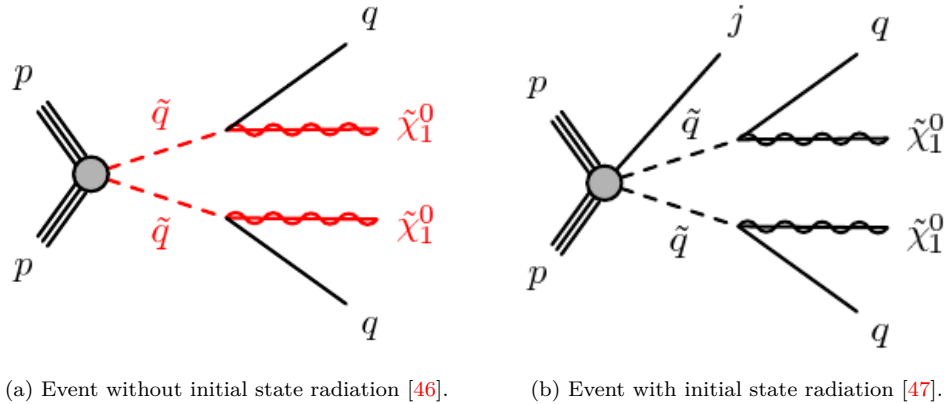
$$|\vec{p}_q| = |\vec{p}_{\tilde{\chi}_1^0}| = \frac{M_{\tilde{q}}^2 - m_{\tilde{\chi}_1^0}^2}{2M_{\tilde{q}}}. \quad (7.1.4)$$

The quark will hadronize in the calorimeter and give rise to a jet that can be detected by the ATLAS detector only if  $p_T > 20$  GeV. If for example the mass of the squark is  $M_{\tilde{q}} = 450$  GeV and the mass of the neutralino is  $m_{\tilde{\chi}_1^0} = 445$  GeV then it can be seen from Eq. (7.1.4) that the quark and neutralino momenta are given by  $|\vec{p}_q| = |\vec{p}_{\tilde{\chi}_1^0}| = 5$  GeV. Since the neutralino escape detection, this results in low  $E_T^{\text{miss}}$  thus when the mass of the neutralino approaches the mass of the quark this results in a low energy jet and  $E_T^{\text{miss}}$  that cannot be triggered by the ATLAS detector. This means that when the mass difference between the particles is small, the sensitivity to new physics signal of many standard SUSY searches is reduced due to

the low amount of missing energy and the low transverse momentum of the associated jets. This effect is shown in Figure 7.2 that reports the results of the “Standard SUSY multijet +  $E_T^{\text{miss}}$ ” analysis, it can be seen that there is no sensitivity close to the diagonal in the region  $400 < M_{\tilde{q}} < 600$  GeV.

If in the event is present an initial state radiation jet, as depicted in Figure 7.1b, the squark–squark system gets boosted in the opposite direction thus increasing the momentum of the decay products and the missing energy leading to a clean signature for the monojet.

Events with an energetic jet  $p_T$  and large  $E_T^{\text{miss}}$  in the final state thus constitute a clean signature for new physics searches at hadron colliders. Signals that can be studied with this experimental signature include the production of WIMPS, the ADD model for large extra dimensions and SUSY.



(a) Event without initial state radiation [46].

(b) Event with initial state radiation [47].

Figure 7.1: Event topology of squark pair production resulting in a neutralinos with two jets final state with (Figure 7.1b) and without (Figure 7.1a) initial state radiation.

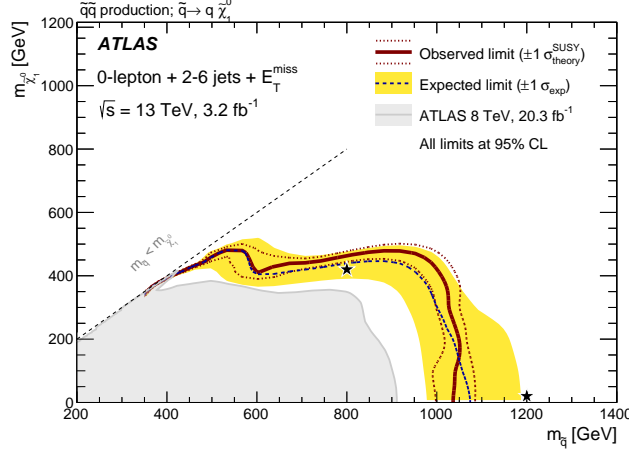


Figure 7.2: Exclusion limits for direct production of squark pairs [46].

## 7.2 Event Selection

The search is carried out in  $pp$  collisions using the data collected by the ATLAS experiment during the 2015 Run II corresponding to a total integrated luminosity of  $3.2 \text{ fb}^{-1}$ . The signal region is defined by the following selection criteria:

- A - The HLT\_xe70 trigger was used in the whole 2015 dataset.
- B - In order to assure that the event originated from a  $pp$  collision, a primary vertex with at least two associated tracks with  $p_T > 0.4 \text{ GeV}$  is required.
- C - Events in which any jet fails the *loose* jet cleaning criteria are rejected. This suppress noise from non-collision background.
- D - The most energetic jet in the event (the *leading jet*) must have  $p_T > 250 \text{ GeV}$  and  $|\eta| < 2.4$ . Moreover, in order to reject beam-induced and cosmic particles background, the event is rejected if the leading jet fails the *tight* cleaning criteria.
- E - In order to suppress  $Z(\rightarrow \ell\bar{\ell}) + \text{jets}$  and  $W(\rightarrow \ell\nu) + \text{jets}$  background, events with an identified electron of  $p_T > 20 \text{ GeV}$  or muon of  $p_T > 10 \text{ GeV}$  are rejected.
- F - In order not to overlap with other ATLAS analyses, events with more than four jets are rejected, see Section 7.3 for more details on this selection.
- G - The  $E_T^{\text{miss}}$  trigger can acquire multi-jet events in case of a mis-reconstructed jet, since in these cases, usually, the missing transverse momentum points in the direction of one of the jets, this background can be suppressed by imposing a minimum azimuthal angle separation between the missing transverse momentum and any jet of  $R = 0.4$ .
- H - A  $E_T^{\text{miss}} > 250 \text{ GeV}$  requirement is imposed in order to be able to test different BSM signals with different sensitivities to the missing energy.

Inclusive (IM1–IM7) and exclusive (EM1–EM6) [Signal Regions \(SRs\)](#) are defined in the monojet analysis with increasing  $E_T^{\text{miss}}$  thresholds from  $250 \text{ GeV}$  to  $700 \text{ GeV}$ , see Table 7.1 for the exact definition of the signal regions. These different  $E_T^{\text{miss}}$  bins are defined in order to address different BSM signals tested with the monojet signature. In this chapter special emphasis is placed on the compressed squark–neutralino model which has been studied by the author of the thesis.

## 7.3 Jet Veto

In order to reduce the overlap with other analyses, especially those containing multijet final states, an upper cut on the number of [HS](#) jets is necessary. This procedure is denominated *jet veto*. In order to define hard scatter jets, cuts on the jet  $p_T$  and on the JVT (see Section 6.6.2) have been studied. The aim of these cuts is to render the analysis independent from pile-up as much as possible but stay signal efficient, too hard cuts would lead to disregarding possible signal events while, on the other hand, too loose cuts let pile-up jets in the signal region.

Due to the jets coming from the squark decays, the SUSY compressed squark–neutralino model have more jets compared to other signals considered in the monojet analysis and are therefore the most sensitive to jet veto efficiency and to the definition of hard scatter jet. To study the pile-up contamination of different  $p_T$  thresholds

Event Selection Criteria							
HLT_xe70 trigger							
Primary Vertex							
$E_T^{\text{miss}} > 250 \text{ GeV}$							
Leading jet with $p_T > 250 \text{ GeV}$ and $ \eta  < 2.4$							
At most 4 jets							
$\Delta\phi(\text{jets}, E_T^{\text{miss}}) > 0.4$							
Jet quality requirements							
No identified muon with $p_T > 10 \text{ GeV}$ or electron of $p_T > 20 \text{ GeV}$							
Inclusive SRs	IM1	IM2	IM3	IM4	IM5	IM6	IM7
$E_T^{\text{miss}} [\text{GeV}]$	$> 250$	$> 300$	$> 350$	$> 400$	$> 500$	$> 600$	$> 700$
Exclusive SRs	EM1	EM2	EM3	EM4	EM5	EM6	
$E_T^{\text{miss}} [\text{GeV}]$	$[250\text{--}300]$	$[300\text{--}350]$	$[350\text{--}400]$	$[400\text{--}500]$	$[500\text{--}600]$	$[600\text{--}700]$	

Table 7.1: Definition of the signal region.

a *figure of merit* is defined and its dependence from the average number of proton–proton collisions per bunch crossing studied. The figure of merit is defined as:

$$\frac{N \text{ (events) with baseline cuts + at most } N \text{ (jet) HS jets}}{N \text{ (events) with baseline cuts}} \quad (7.3.1)$$

where the baseline cuts, excluding cut F, are given in Section 7.2 (the study presented here uses  $E_T^{\text{miss}} = p_T = 250 \text{ GeV}$ ) and the hard scatter jets are defined as:

- Jets with  $p_T > 50 \text{ GeV}$  or  $|\eta| > 2.4$  (forward jets), are always considered coming from the hard scatter.
- In order to be considered coming from the hard scatter proton-proton collision, the jets with  $p_T^{\text{thresh}} \leq p_T \leq 50 \text{ GeV}$  must additionally satisfy a  $\text{JVT} > \text{JVT}^{\text{thresh}}$  selection where different  $p_T^{\text{thresh}}$  and  $\text{JVT}^{\text{thresh}}$  have been studied, in particular  $p_T^{\text{thresh}} \in \{30 \text{ GeV}, 40 \text{ GeV}, 50 \text{ GeV}, 70 \text{ GeV}\}$  and  $\text{JVT}^{\text{thresh}} \in \{0.14, 0.64, 0.92\}$ .

Figure 7.3a shows the jet veto efficiency for the different  $p_T^{\text{thresh}}$  and  $N \text{ (jets)} \leq 4$  in the case where no JVT cut is applied. In the case of  $p_T^{\text{thresh}}$  of 30 GeV the pile-up dependence is noticeable while it becomes less important with tighter cuts. In Figure 7.3b a  $\text{JVT} > 0.64$  selection is applied in the definition of the hard scatter jets, in this case the pile-up dependence for the  $p_T^{\text{thresh}}$  of 30 GeV is reduced and the distribution for  $p_T^{\text{thresh}}$  of 40, 50 and 70 GeV cuts is, within statistical error, flat. The effect of the upper cuts on the number of hard-scatter jets with the default definition used in this analysis on the signal models considered was verified. Figure 7.4 shows no strong dependence of the jet veto efficiency as function of the average number of interaction per crossing. The selected definition of the hard-scatter jets, with  $N \text{ (jets)} \leq 4$  provides high efficiency for the considered signals.

## 7.4 Sources of Background

The Standard Model process  $Z \rightarrow \nu\bar{\nu} + \text{jets}$  where the jets are produced by [Initial State Radiation \(ISR\)](#) and the neutrinos escape detection generating large  $E_T^{\text{miss}}$  is

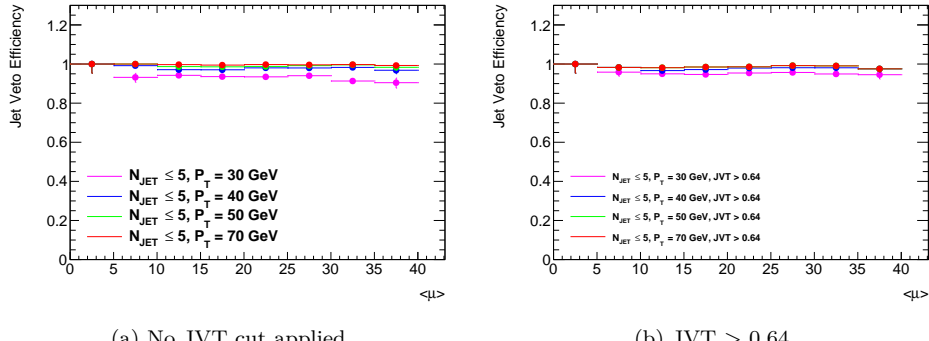


Figure 7.3: Jet veto efficiency for different jet  $p_T$  thresholds and  $N(\text{jets}) \leq 4$  as a function of the average number of interactions per bunch crossing  $\langle \mu \rangle$  for a compressed spectra  $M_{\tilde{q}} = 450 \text{ GeV}$   $M_{\tilde{\chi}_0^1} = 435 \text{ GeV}$ . In Figure 7.3a no JVT cut is applied and there is some drop of the efficiency at high pile-up. In Figure 7.3b a  $\text{JVT} > 0.64$  cut is applied, the dependence from pile-up is reduced.

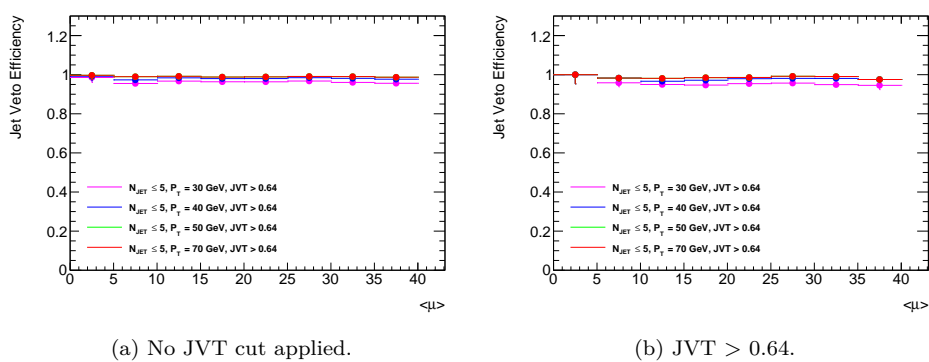


Figure 7.4: Jet veto efficiency for different jet  $p_T$  thresholds and  $N(\text{jets}) \leq 4$  with a  $\text{JVT} > 0.64$  selection applied as a function of the average number of interactions per bunch crossing  $\langle \mu \rangle$  for the analysis  $Z \rightarrow \nu\bar{\nu}$  background (Figure 7.4a) and the SUSY squark–neutralino signal model with  $M_{\tilde{q}} = 450$  GeV and  $M_{\tilde{\chi}_0^1} = 435$  GeV.

experimentally similar to signal events in the search for BSM physics with a monojet signature in the final state. This process constitutes an irreducible background and is the largest background in the monojet analysis. The key to estimate the  $Z \rightarrow \nu\bar{\nu} + \text{jets}$  background is to be able to predict the momentum spectrum of the  $Z$  boson and thus the amount of missing transverse energy. The control regions defined in later sections provide ways to derive the  $Z$  boson momentum using data control regions.

The second biggest source of background with a monojet topology is the  $W(\rightarrow \ell\nu) + \text{jets}$ , where  $W(\rightarrow \tau\nu) + \text{jets}$ , in which the  $\tau$  decays hadronically, it gives the highest contribution to this class of events. The  $W(\rightarrow \ell\nu) + \text{jets}$  events with  $\ell = e$  or  $\mu$  can fake a monojet signature if the lepton escapes the detector acceptance or has a quality that is lower than the quality of the lepton veto criteria.

Other background processes are di-boson,  $t\bar{t}$  and single top processes. Multi-jet production from QCD processes where one or more jets are mis-reconstructed leading to high  $E_T^{\text{miss}}$  represent a small source of background. Finally **Non Collision Background (NCB)** coming from cosmic particles, detector noise and beam-induced background can give rise to fake jets and consequently to  $E_T^{\text{miss}}$ .

## 7.5 Estimation of the $Z + \text{jets}$ and $W + \text{jets}$ backgrounds

A **Control Region (CR)** is a region of the phase space where the signal contribution is negligible but the event selections are similar to those of the signal region. The main reason to define control regions is to check the agreement in shape and normalization between MC simulations and data in reconstructed kinematic quantities. The  $V + \text{jets}$ , where  $V$  is either a  $W$  or a  $Z$  vector boson, constitutes the main background of the monojet analysis. A pure MC estimation of these processes, suffers from theoretical uncertainties like the limited knowledge of the **Parton Distribution Functions (PDFs)**, limited order accuracy of the Monte Carlo generators and experimental uncertainties related to the JES and luminosity determination. In order to estimate the contribution of these backgrounds in the SR, a *data driven* technique is used. The method aims at reducing the systematic uncertainties by relying on information from data in the CRs rather than on MC simulations. It can be divided in three major steps:

- Define CRs to select  $V + \text{jets}$  event in data.
- Calculate a transfer factor from MC predicted events in the CR to background estimates in the SR.
- Apply the transfer factor to the observed events in the CR to obtain the estimate number of events from the process in the SR.

The CRs used to constrain the  $V + \text{jets}$  backgrounds have an event selection that differs from the SR only in the lepton veto and the missing transverse momentum calculation. They are thus orthogonal to the SR and a minimum contribution from a monojet-like signal is expected.

### 7.5.1 The Muon Control Region

The  $W(\rightarrow \mu\nu) + \text{jets}$  events can enter the SR if the muon is outside the detector acceptance or it fails quality criteria. The muon control region ( $\text{CR}_{\text{wmn}}$ ) selects  $W(\rightarrow \mu\nu) + \text{jets}$  events in order to estimate the  $Z(\rightarrow \nu\bar{\nu}) + \text{jets}$  contribution in the signal region. The muon is treated like a neutrino in the  $E_{\text{T}}^{\text{miss}}$  calculation, in this way the  $E_{\text{T}}^{\text{miss}}$  is a measurement of the  $W$  momentum which is later translated in the  $Z$  boson momentum to estimate the  $Z(\rightarrow \nu\bar{\nu}) + \text{jets}$  background. The  $\text{CR}_{\text{wmn}}$  region selects events with:

- Exactly one good muon.
- The transverse mass, defined as:

$$m_{\text{T}} = \sqrt{2p_{\text{T}}^{\mu}p_{\text{T}}^{\nu}(1 - \cos(\phi_{\mu} - \phi_{\nu}))} \quad (7.5.1)$$

and determined by the muon ( $p_{\text{T}}^{\mu}$ ) and neutrino ( $p_{\text{T}}^{\nu}$ )  $p_{\text{T}}$ , is required to be  $30 < m_{\text{T}} < 100$  GeV, consistent with  $W$  boson production.

The transverse mass cut suppress the  $W(\rightarrow \tau\nu) + \text{jets}$  processes in this region. The measured  $E_{\text{T}}^{\text{miss}}$  and leading jet  $p_{\text{T}}$  distributions after the fitting the background normalizations to the control regions (see Section 7.5.4) are shown in Figure 7.5. The agreement between data and MC is good.

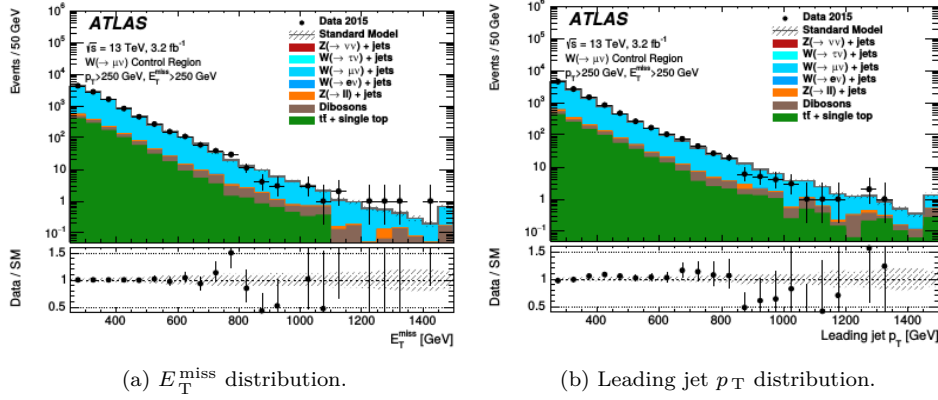


Figure 7.5: Observed and predicted  $E_T^{\text{miss}}$  and leading jet  $p_T$  distributions after the background only fit in the single muon CR for the  $E_T^{\text{miss}} > 250$  GeV selection. The error bands include the statistical and systematic error.

### 7.5.2 The Electron Control Region

The  $W(\rightarrow e\nu) + \text{jets}$  process enter the signal region, thus contributing to the background, in case the electron is not identified in the detector. In the  $W(\rightarrow \tau\nu) + \text{jets}$  process the  $\tau$  particle can decay hadronically in the 65% of the cases resulting in additional jets that can help this background mimic the signal. To address these backgrounds an electron control region ( $\text{CR}_{\text{ele}}$ ) is built. It is designed to constrain both  $W(\rightarrow e\nu) + \text{jets}$  and  $W(\rightarrow \tau\nu) + \text{jets}$  processes. In order to efficiently reject multi-jet background, the electron is retained in the  $E_T^{\text{miss}}$  calculation, the missing transverse momentum in this case measures the momentum of the escaping neutrino. The  $\text{CR}_{\text{ele}}$  region selects events with:

- Exactly one good electron.
- Reject any other good electron.

In order to enhance the  $W(\rightarrow \tau\nu) + \text{jets}$  contribution in this region, no  $m_T$  cut is applied. Figure 7.6 shows the observed and predicted  $E_T^{\text{miss}}$  and the leading jet  $p_T$  distribution in this control region. The overall agreement between data and MC is good and improved after the global likelihood fit procedure described in Section 7.5.4.

### 7.5.3 The Di-Muon Control Region

This region ( $\text{CR}_{\text{zmm}}$ ) is designed to select the  $Z(\rightarrow \mu^+\mu^-) + \text{jets}$  events in order to estimate the background contribution in the signal region coming from this process together with the dominant  $Z(\rightarrow \nu\bar{\nu}) + \text{jets}$ . Events in the  $\text{CR}_{\text{zmm}}$  region are selected requiring:

- Exactly two good muons.
- An invariant mass in the  $Z$  boson mass window range  $66 < m_{\mu\mu} < 116$  GeV.

Figure 7.7 shows a good agreement between data and MC for the measured  $E_T^{\text{miss}}$  and leading jet  $p_T$  distributions also in this region.

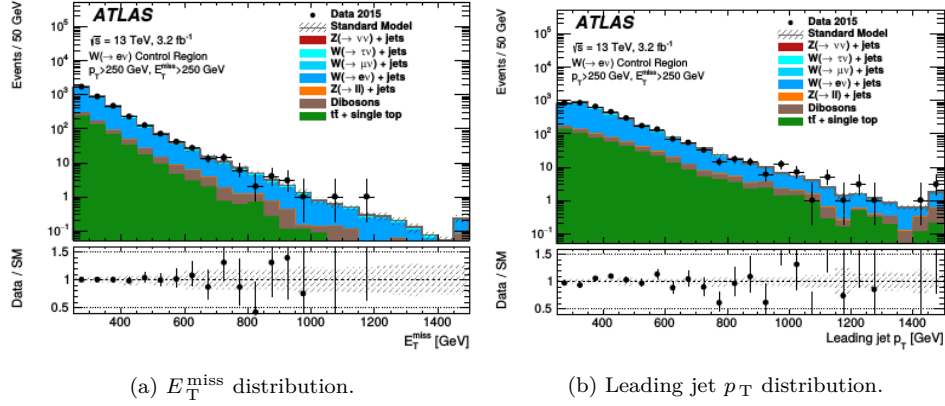


Figure 7.6: Observed and predicted  $E_T^{\text{miss}}$  and leading jet  $p_T$  distributions after the background only fit in the electron CR for the  $E_T^{\text{miss}} > 250$  GeV selection. The error bands include the statistical and systematic error.

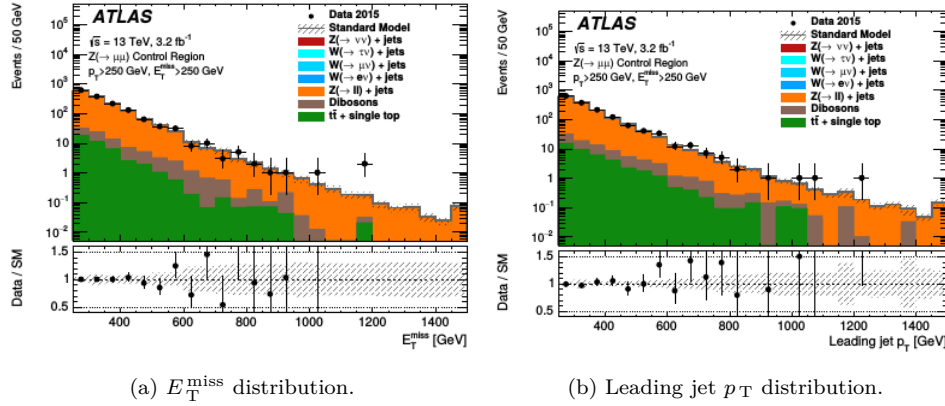


Figure 7.7: Observed and predicted  $E_T^{\text{miss}}$  and leading jet  $p_T$  distributions after the background only fit in the di-muon CR for the  $E_T^{\text{miss}} > 250$  GeV selection. The error bands include the statistical and systematic error.

#### 7.5.4 The Global Simultaneous Likelihood Fit

A pure MC based prediction of the background contamination in the signal region would suffer from large theoretical and experimental systematic uncertainties in the shape and normalization of the predicted distributions, thus a data driven approach, where the different backgrounds are normalized using the data in CRs that are orthogonal to the SR, is used. To extrapolate from CR to SR prediction an MC based *transfer factor* is used. This factor is a ratio of MC predictions thus most of the systematic uncertainties either cancel out or are significantly reduced. The extrapolation from one kinematic region to another can be itself source of uncertainties, to avoid this, the selection in terms of kinematic in the CRs and SRs is chosen to be the same. The expected contributions of a background process  $BG_i$ , which is extracted from a control region  $CR_j$  dominated by background  $BG_j$ , to a signal region  $SR_k$ , is given

by:

$$N_{\text{BG}_i}^{\text{SR}_k} = \frac{(N_{\text{data}}^{\text{CR}_j} - N_{\text{non BG}_i, \text{ MC}}^{\text{CR}_j})}{N_{\text{BG}_i, \text{ MC}}^{\text{CR}_j}} \times N_{\text{BG}_i, \text{ MC}}^{\text{SR}_k} \quad (7.5.2)$$

where  $N_{\text{BG}_i}^{\text{SR}_k}$  is the predicted number events for background  $i$  events in the signal region  $\text{SR}_k$ ,  $N_{\text{data}}^{\text{CR}_j}$  is the observed number of events in the control region  $j$ ,  $N_{\text{non BG}_i, \text{ MC}}^{\text{CR}_j}$  is the estimated number of the background contamination coming from other processes in the given control region,  $N_{\text{BG}_j, \text{ MC}}^{\text{CR}_j}$  is the MC prediction of the  $j$  background in the  $j$  control region and  $N_{\text{BG}_i, \text{ MC}}^{\text{SR}_k}$  is the number of the  $i$  background events predicted in MC simulation in the signal region. The ratio:

$$C_{\text{BG}_i}^{\text{CR}_j \rightarrow \text{SR}_k} = \frac{N_{\text{BG}_i, \text{ MC}}^{\text{SR}_k}}{N_{\text{BG}_j, \text{ MC}}^{\text{CR}_j}} \quad (7.5.3)$$

is the transfer factor used to extrapolate from  $\text{CR}_j$  to  $\text{SR}_k$ . The normalization factors used in the normalization of the BG expectation in the SRs is given by:

$$\mu_{ijk} = \frac{(N_{\text{data}}^{\text{CR}_j} - N_{\text{non BG}_i, \text{ MC}}^{\text{CR}_j})}{N_{\text{BG}_k, \text{ MC}}^{\text{CR}_j}}. \quad (7.5.4)$$

The different normalization factors are not independent since different processes can enter several CRs and thus the background subtraction term,  $N_{\text{other BG}, \text{ MC}}^{\text{CR}_j}$ , gets contributions from the other normalization factors. To properly treat the correlations, the normalization factors are obtained from a simultaneous fit of all the CRs referred to as the *global fit*. A summary of the different processes and the corresponding CR used to extract the normalization factor is given in Table 7.2.

Control Region	Background Process	Normalization Factor
$\text{CR}_{\text{wmn}}$	$W(\rightarrow \mu\nu), Z(\rightarrow \nu\bar{\nu})$	$\mu_{\text{wmn}}$
$\text{CR}_{\text{ele}}$	$W(\rightarrow e\nu), W(\rightarrow \tau\nu), Z/\gamma^*(\rightarrow \tau^+\tau^-)$	$\mu_{\text{ele}}$
$\text{CR}_{\text{zmm}}$	$Z/\gamma^*(\rightarrow \mu^+\mu^-)$	$\mu_{\text{zmm}}$

Table 7.2: Summary table of the different background processes and the corresponding control regions used to evaluate the normalization factors.

The global fit can be performed in two different ways:

1. The background only hypothesis, fits only the control regions in order to predict the background in the signal region. This fit is used to set model independent limits.
2. The signal plus background hypothesis, fits both the signal and control regions with a sum of background and specific signal. The normalization of the specific BSM signal is a free parameter. This fit is used to exclude specific models.

## 7.6 Other Backgrounds

### 7.6.1 The Multi-Jet Background

The multi-jet background events are mainly due to mis-reconstruction or loss in some dead part of the calorimeter of jets or to the presence of neutrinos in some heavy-flavor

hadronic decay. The acceptance in the SR for multi-jet events is low, nevertheless the large cross section of this process could potentially lead to a high contamination in the SR. The use of MC simulation in order to estimate the contribution to BG of this process is very difficult due to the very large MC samples that would be required and the detailed modeling of any calorimeter defects. For these reasons a data–driven technique, the *jet smearing method*, is used. It addresses event topologies with large  $E_T^{\text{miss}}$  originating from jet mis-reconstruction. This method creates large sample of well measured low  $E_T^{\text{miss}}$  jets called *seeds* which are *smeared* using a function that quantify the  $p_T$  fluctuation of a measured reconstructed jet (the *response function*) to create  $E_T^{\text{miss}}$  in the event. This process is reiterated many times to create a *pseudo-data* sample that is used in the SR analysis selection to estimate the distribution of variables defining the control and signal regions. The procedure is described in more details in Ref. [48]. The multi-jet control region is defined by inverting the  $\Delta\phi_{\min}(E_T^{\text{miss}}, \text{jet})$  and applying the inclusive and exclusive SR  $E_T^{\text{miss}}$  cuts. For the EM1 and IM1 the multi-jet background constitutes the 0.5% of the total BG and it is negligible in other signal regions.

### 7.6.2 The Non-Collision Background

Non collision background is a term used to refer to BG processes coming from cosmic particles, beam induced muons resulting from proton-gas inelastic interaction or beam halo protons intercepting the LHC collimators and detector noise. The characteristic signature of NCB is that of a jet recoiling against invisible energy thus resembling the monojet final state signature. The jet quality selection criteria mentioned in Section 7.2 manage to reduce the rate of jet coming from cosmic muons to a negligible amount compared to the rate of data in the SR thus the main source of NCB is [Beam Induced Background \(BIB\)](#). In order to estimate the BIB contribution the two-sided no-time method [49] was used. This method tries to match a calorimeter energy cluster with a muon segment in both A and C side of the detector. This topology corresponds to a particle moving parallel to the beam line but several meters away from the beam axis and thus presumably arising from beam background. An estimate of the number of NCB events in the SR is obtained by correcting the number of events tagged as BIB inside the signal region for the efficiency of the method. The efficiency of the tagger is estimated in a sample of events in the SR failing the jet tight cleaning criteria that is dominated by BIB jets.

The NCB contribution in the IM1 results in  $112 \pm 23$  events and only  $19 \pm 9$  events in the EM3, this constitutes about 0.5% of the total background in these regions. For  $E_T^{\text{miss}} > 500$  GeV there is no NCB contribution in the signal region.

## 7.7 Systematic Uncertainties

Systematic uncertainties can originate from the theory, caused for example by our limited knowledge of the parton distribution function, or from experimental sources such as the absolute jet energy scale and resolution or production cross section for various processes determination. The systematic uncertainties are treated as Gaussian nuisance parameters in the global likelihood fit described in Section 7.5.4.

### 7.7.1 Theoretical Uncertainties

Since the normalization factor for the  $Z(\rightarrow \nu\bar{\nu})$  is taken from the single muon region, following the Run 1 analysis strategy [50], a conservative flat  $\pm 3\%$  uncertainty corresponding to the maximum variation in several distributions for different  $E_T^{\text{miss}}$  regions is assumed. This number includes MC modeling differences between the  $E_T^{\text{miss}}$  in the  $Z(\rightarrow \nu\bar{\nu})$  and in  $W(\rightarrow \mu\nu)$ , parton shower parameters, PDFs related uncertainties and the lepton reconstruction acceptance. In practice we look for small differences in the  $W(\rightarrow \mu\nu) + \text{jets}$  and  $Z(\rightarrow \nu\bar{\nu}) + \text{jets}$   $E_T^{\text{miss}}$  distribution and since our background calculation builds on the fact that these quantities should be the same, any difference needs to be taken into account as a systematic. These differences affect the ratio in Eq. (7.5.3).

In addition electroweak correction that takes into account the theoretical differences between the production rate of the  $W$  and  $Z$  bosons as described in Ref. [51] are added in quadrature leading to a  $\pm 3.5\%$  and  $\pm 6\%$  uncertainty in the IM1 and IM7 region respectively.

Processes related to the *top quark* production gets their uncertainties from the  $t\bar{t}$  and single-top production cross section, levels of initial and final state radiation, the parameters used to generate the parton shower MC samples and the normalization factor. This introduce a  $\pm 2.7\%$  and  $\pm 3.3\%$  variation in the background estimation in the IM1 and IM7 signal region respectively. Uncertainties coming from *diboson* processes are estimated using different MC generators and account for an uncertainty between  $\pm 0.05\%$  and  $\pm 0.4$  on the number of events in the signal region. A flat  $\pm 100\%$  uncertainty is assigned to *multi-jet* and *NCB* that translates to a  $\pm 0.2\%$  variation in the total background in the IM1 signal region.

### 7.7.2 Experimental Uncertainties

Experimental systematic uncertainties can be divided in the following broad categories:

- **Jet/ $E_T^{\text{miss}}$ :** This category includes uncertainties on the  $E_T^{\text{miss}}$  and jet energy scale and resolution, jet quality, pile-up estimation and  $p_T$  measurement.
- **Leptons:** This category includes uncertainties related to the identification, simulation, reconstruction efficiencies and energy and momentum resolution of electrons and muons.
- **Luminosity:** Is the uncertainty on the integrated luminosity.

A  $\pm 5\%$  uncertainty is assigned to the *integrated luminosity*. Since the efficiency plateau of the HLT\_xe70 is reached below 250 GeV  $E_T^{\text{miss}}$  values, no uncertainty is assigned to the trigger. Uncertainties in the jet and  $E_T^{\text{miss}}$  *energy scale* and *resolution* contribute to the total background with a variation of  $\pm 0.5\%$  and  $\pm 1.6\%$  in the IM1 and IM7 respectively. The jet quality requirement, pile-up estimation and correction to the measured  $E_T^{\text{miss}}$  and jet  $p_T$  results in an uncertainty in the estimation of the total background of  $\pm 0.2\%$  in the IM1 and  $\pm 0.9\%$  in the IM7 control region. Lepton *identification* simulation and *reconstruction efficiency* lead to a  $\pm 0.1\%$  uncertainty in the IM1 and IM7 regions while energy and momentum *resolution* results in a  $\pm 1.4\%$  variation in the IM1 selection and a  $\pm 2.6\%$  uncertainty in the IM7 signal region.

## 7.8 Results and Interpretations

The number of events observed in data in the signal regions was compared with the background only fit. The results of the comparison between the observed number of events in data and the background calculations including the background only fit is shown in Figure 7.8. No significant excess of data over background is observed. The results of the global fit procedure described in Section 7.5.4 are used to set model independent exclusion limit (see Section 7.8.3) and interpreted in terms of squark pair production with  $\tilde{q} \rightarrow q + \tilde{\chi}_1^0$  ( $q = u, d, c, s$ ) (see Section 7.8.4).

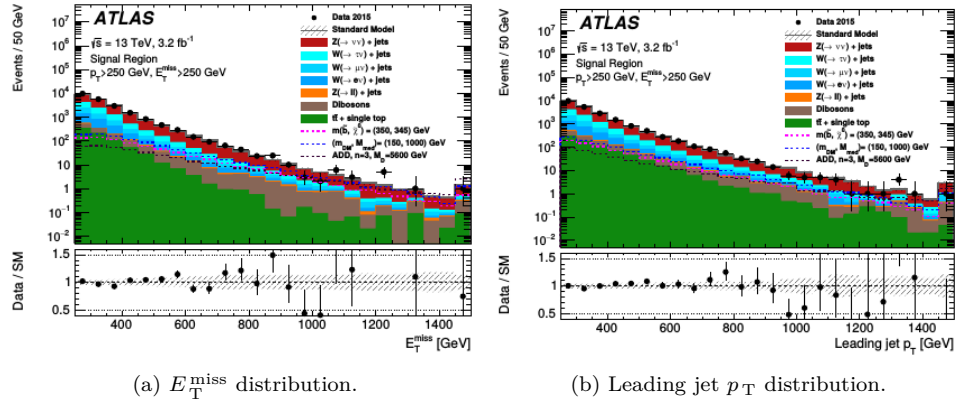


Figure 7.8: Distribution of the  $E_T^{\text{miss}}$  and the leading jet  $p_T$  for IM1 signal region compared with the background estimates from the background only fit in the control regions. The distributions of different signal models are superimposed for comparison. The contribution from the multi-jet and NCB background is negligible and not reported in the plot. In the ratio window the error bars include experimental and systematic uncertainties.

### 7.8.1 The Signal Hypothesis Exclusion Procedure

In general the physics search strategy for new phenomena can be outlined in four steps, the first one is to define an *hypothesis test*, the *null hypothesis*, is that no signal is present i.e. only known SM processes are present in the SR and the *alternate hypothesis* is that it exists. The next steps are meant to quantify which one of the hypotheses is favored by experimental observations. To this end it is necessary to identify the observables of the experiment, next a *test-statistic* (a function of these observables) of the known background and to be tested signal is defined to rank the experiments from the least to the most signal-like. Finally a rule to quantify the significance of the exclusion or discovery is chosen.

In the monojet analysis the observable of the experiment is the number of events in the signal regions defined with the criteria illustrated in Section 7.2, the  $E_T^{\text{miss}}$  is the test-statistic and a **Confidence Level (CL)** of 95% is chosen for the exclusion. The number of events observed in the signal region is governed by a Poisson distribution

$$P(O|E) = \frac{E^O}{O!} e^{-E} \quad (7.8.1)$$

where  $O$  is the number of observed events and  $E$  is the number of expected events. In absence of signal (background only hypothesis), the expected number of events is the total number of predicted background events from SM processes. If some signal is

present (signal plus background hypothesis), the expected number of events is given by the predicted number of background events plus the predicted number of signal events. In terms of Poisson distribution, the probability of observing up to  $N_{\text{SR}}$  events in the SR in a signal plus background hypothesis is:

$$P(N_{\text{SR}}|\mu_S + B) = \sum_{k=0}^{N_{\text{SR}}} \frac{(\mu_S + B)^k}{k!} e^{-(\mu_S + B)}, \quad (7.8.2)$$

where  $\mu_S$  is the *signal strength* and represents the number of expected signal events. The lower this probability is, the more likely it is that the tested signal is not present in the SR and the hypothesis of it explaining some physics process can be excluded. To quantify the significance of the exclusion a CL is calculated as:

$$CL_{S+B} = 1 - P(N_{\text{SR}}|S + B) = 1 - \alpha \quad (7.8.3)$$

where typically  $\alpha = 0.05$  and a 95% CL<sub>S+B</sub> is quoted. The maximum number of expected signal events ( $S_{\text{max}}$ ) for which CL<sub>S+B</sub> < 0.95 can be calculated and if the number of expected signal events ( $S$ ) exceeds this value ( $S > S_{\text{max}}$ ), the model can be excluded [52] with a confidence level  $\alpha$ . In the monojet analysis the CL<sub>S</sub> method [53] is used, where:

$$CL_S = \frac{CL_{S+B}}{CL_B}. \quad (7.8.4)$$

The CL<sub>S</sub> method is preferred in high energy physics. It is designed to address situations where the observed data could fluctuate below the predicted SM background. This can happen in the case of low statistic, using CS<sub>S+B</sub> in this case can lead to exclude BSM signals even if the experiment has no real sensitivity. The CL<sub>S</sub> method allows to deal with such situations and obtain more conservative limits on the signal hypothesis by normalizing the confidence level obtained in the signal plus background hypothesis to the confidence level in the background only hypothesis.

## 7.8.2 Expected Limits

Since in the compressed SUSY models the  $E_T^{\text{miss}}$  recoils typically against several jets, the average jet momenta are lower than the missing energy, thus requiring an asymmetric cut on the leading jet momentum and  $E_T^{\text{miss}}$  to capture this signal. Prior to deciding the signal region selections presented in Section 7.2 a signal region (AM1) with  $E_T^{\text{miss}} > 700$  GeV and leading jet  $p_T > 300$  GeV was defined and compared with the IM1 signal region. The results for an integrated luminosity of  $L = 3.3 \text{ fb}^{-1}$  for these two signal regions is presented in Figure 7.9. On these figure a model is excludable if the signal strength  $\mu$ , depicted by the color scale in the picture, is lower than one. The sensitivity improves for the signal region AM1 to reflect the asymmetric kinematics.

In the AM1 signal region, models with mass gaps  $\Delta m = 5$  GeV between the squark mass and the neutralino mass, can be excluded up to squark masses of 650 GeV. At a larger mass gap of  $\Delta m = 25$  GeV, squark masses up to 580 GeV are excludable.

The performance of the shape fit method was also tested on the SUSY compressed squark–neutralino model and the result is also shown in Figure 7.9. The shape fit method, thanks to its flexibility, is capable of adapting to different signal models and thus improves the expected limits of the SUSY squark–neutralino model especially for the largest mass gap of  $\Delta m = 25$  GeV between the squark and the neutralino masses.

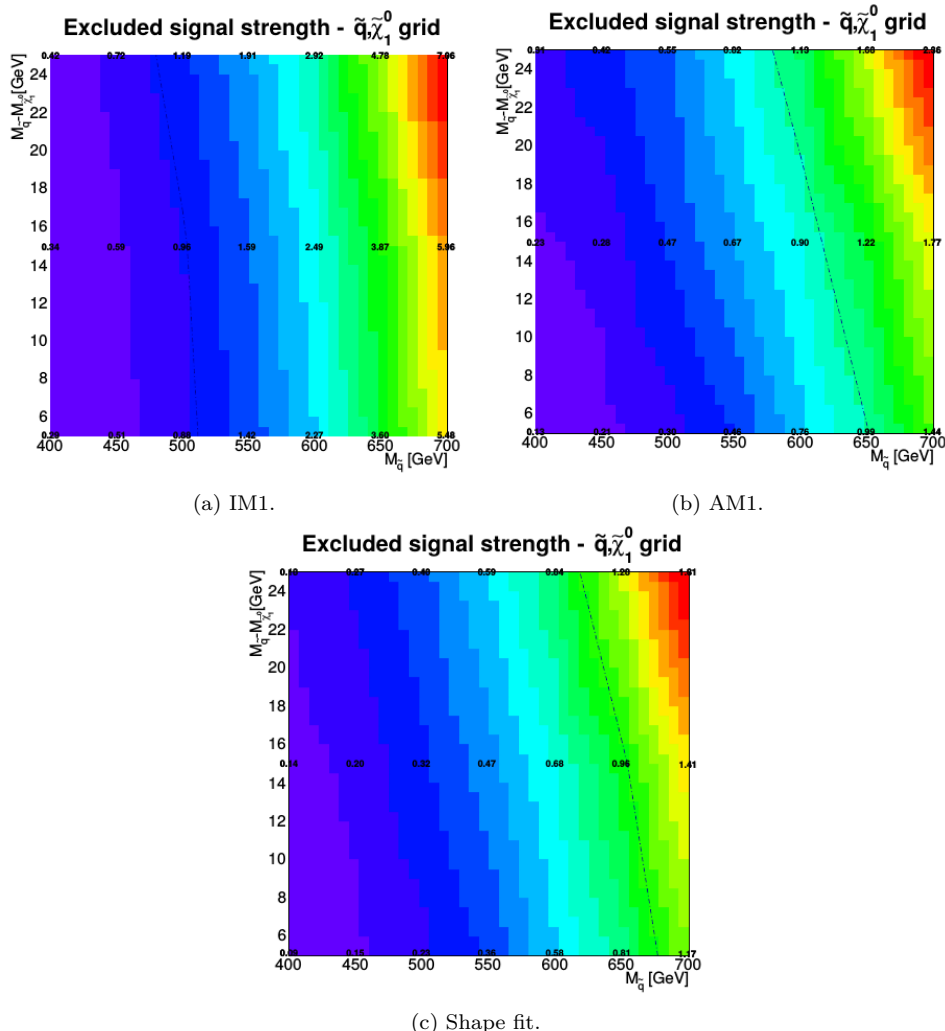


Figure 7.9: Sensitivity to the compressed SUSY models with an integrated luminosity of  $L = 3.3 \text{ fb}^{-1}$  in the plane defined by the squark mass  $m_{\tilde{q}}$  and the mass difference between the squark mass and the lightest neutralino mass  $\Delta m = m(\tilde{q}) - m(\tilde{\chi}_1^0)$ . The color scale reflects the lowest excludable signal strength for a particular mass point. The values indicated on the map indicate the actual excludable  $\mu$  values at some specific SUSY models. The dashed line shows the limit between excludable and not excludable models. The theoretical uncertainties in the signal are not included.

### 7.8.3 Model Independent Limits

The *visible cross section* represents the number of BSM events in the signal region in units of luminosity and is defined as:

$$\sigma_{\text{vis}} = \sigma \times A \times \epsilon \quad (7.8.5)$$

where  $\sigma$  is the production cross section,  $A$  is the selection acceptance and  $\epsilon$  is the selection efficiency. The CL<sub>S</sub> modified frequentist approach introduced in Section 7.8.1 is used to set 95% CL exclusion limit on the *visible cross section* for models with a monojet final state experimental signature. The results are reported in Table 7.3,

values of  $\sigma_{\text{vis}}$  above  $\langle \sigma \rangle_{\text{obs}}^{95}$  are excluded at 95% CL. These results can be understood as follow: BSM models with more than 19 events per inverse femtobarn of integrated luminosity in the IM7 signal region are excluded by the ATLAS data.

Result Table			
Signal Region	$\langle \sigma \rangle_{\text{obs}}^{95}$ [fb]	$S_{\text{obs}}^{95}$	$S_{\text{exp}}^{95}$
IM1	533	1773	1864 $^{+829}_{-548}$
IM2	308	988	1178 $^{+541}_{-348}$
IM3	196	630	694 $^{+308}_{-204}$
IM4	153	491	401 $^{+168}_{-113}$
IM5	61	196	164 $^{+63}_{-45}$
IM6	23	75	84 $^{+32}_{-23}$
IM7	19	61	48 $^{+18}_{-13}$

Table 7.3: Results on the expected and observed upper limits on the number of events,  $S_{\text{exp}}^{95}$  and  $S_{\text{obs}}^{95}$  respectively and on the visible cross section at 95% CL.

#### 7.8.4 SUSY Compressed Spectra Interpretation

The results of model independent limits are interpreted in terms of limits computed for squark pair production with  $\tilde{q} \rightarrow q + \tilde{\chi}_1^0$  ( $q = u, d, c, s$ ) in a SUSY compressed scenario. The sensitivity to these models is estimated by performing a global signal plus background fit that includes the CR<sub>ele</sub>, CR<sub>wmn</sub>, CR<sub>zmm</sub> control regions, the signal regions and all the systematic uncertainties. The expected limits are derived with the same procedure but by replacing the data with the background prediction.

Figure 7.10 shows the result limits on the SUSY compressed squark–neutralino model for the Run II 2015 data. This is the result of the shape fit with a luminosity of  $3.2 \text{ fb}^{-1}$  with all theoretical signal systematic uncertainties included in the observed and expected exclusion contour and using the CR<sub>ele</sub>, CR<sub>wmn</sub>, CR<sub>zmm</sub> control regions. The theoretical uncertainty on the signal cross section is used to derive the uncertainty on the observed limit.

Models with a mass gap of  $\Delta m = 5 \text{ GeV}$  between the squark and the neutralino mass can be excluded up to squark masses of  $608 \text{ GeV}$ . For larger mass gap of  $\Delta m = 25 \text{ GeV}$ , squark masses up to  $532 \text{ GeV}$  are also excluded. The results of this study are combined with the more general SUSY searches adding sensitivity to the region close to the diagonal (dashed line) in Figure 7.2.

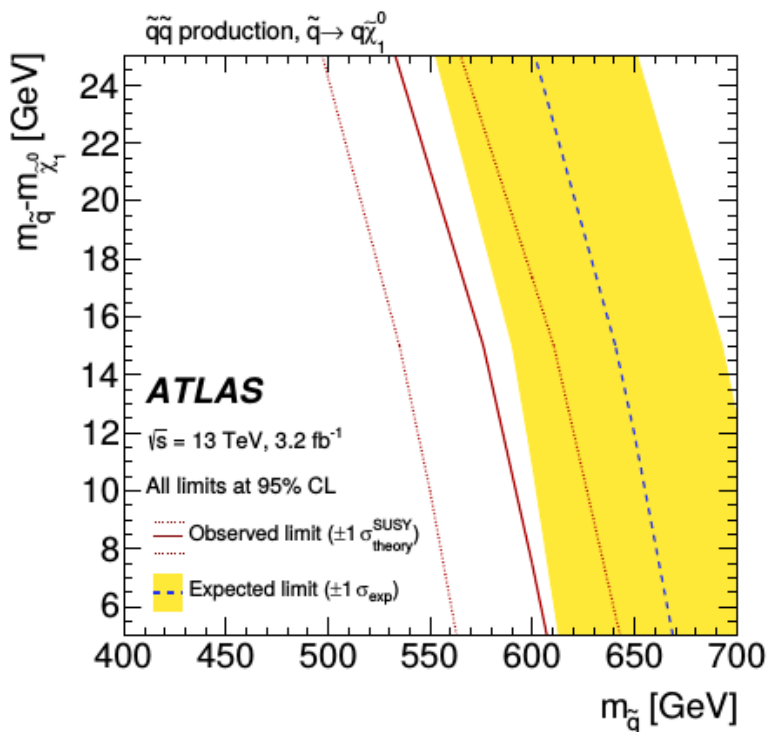


Figure 7.10: Expected and observed limits on the SUSY compressed models using the Run 2 2015 data, in the plane defined by the squark mass on the  $x$ -axis and the mass difference between the squark and lightest neutralino mass on the  $y$ -axis. All experimental and theoretical systematic uncertainties are included.

# Chapter 8

## Conclusions

The ATLAS detector is a multipurpose detector used in the search for the Higgs boson, supersymmetry and dark matter particles. It is divided into three main components, the inner detector, used to track charged particles and momentum measurement, the calorimeters which measure the energy and the muon spectrometer which provides tracking and momentum information for the muons. The Tile Calorimeter is the hadronic calorimeter covering the most central region of the ATLAS detector, it is used in the measurement of hadrons, jets, taus and the missing energy. To this end, an understanding of the electronic noise inside the detector is crucial as it affects the signal left by the particles crossing the calorimeter and must be known in order to know which energy deposits in the calorimeter are significant and should be used in the reconstruction of jets, electrons and taus. Part of the work presented in this thesis was to update, monitor and study the noise calibration constants for the Tile Calorimeter to allow for processing of data and the identification of hadronic jets. During these studies unexpected variations over time in the cell noise were observed. Further investigation led to discover that the tile noise filter, an algorithm used to mitigate the effect of coherent noise, was not behaving as expected in some situations significantly affecting approximately 5% of the cells in the TileCal.

The results of the search for new physics phenomena in a monojet with large missing transverse momentum using the data from  $pp$  collisions at LHC collected by the ATLAS experiment during 2015 and corresponding to an integrated luminosity of  $3.2 \text{ fb}^{-1}$  has been presented. For the first time the monojet analysis was used to set limits on compressed light squark–neutralino models. Selections adapted to the specific characteristics of this signal were studied. It was shown that the generic approach provided by the global fit provides better sensitivity to this new signal than a single signal region with asymmetric jet and  $E_T^{\text{miss}}$  cuts. Several jet veto criteria were studied since the BSM signal studied in this thesis is the most sensitive to this type of cuts and considered in the monojet analysis. It was found that cut F in Section 7.2 provides pile-up independent jet veto efficiency retaining most of the signal. No significant excess in the data compared to the SM predictions has been found thus the results have been translated into model independent upper limits on the visible cross section with a 95% CL and interpreted in terms of squark pair production with  $\tilde{q} \rightarrow q + \tilde{\chi}_1^0$  ( $q = u, d, c, s$ ). Squark masses up to 608 GeV are excluded. This study extends limits shown in Figure 7.2 that are provided by the more classical approach to SUSY searches.

Naturalness suggests that supersymmetric standard model partners are expected

at the TeV scale, with the high luminosity foreseen in 2016 it will be possible to test experimentally the squark pair production with masses at that scale.

# **Appendix A**

## **Further Studies**



# Acronyms

$E_T$  transverse energy. [17](#)

$\eta$  pseudorapidity. [17](#)

$E_T^{\text{miss}}$  missing transverse momentum. [35](#)

$p_T$  transverse momentum. [17](#)

$pp$  proton-proton. [15](#)

**ADC** Analog to Digital Converter. [26](#)

**ALFA** Absolute Luminosity For ATLAS. [20](#)

**ATLAS** A Toroidal LHC apparaSuS. [16](#)

**BG** BackGround. [42](#)

**BIB** Beam Induced Background. [48](#)

**BSM** Beyond Standard Model. [11](#)

**CB** Combined. [35](#)

**CERN** European Organization for Nuclear Research. [15](#)

**CIS** Charge Injection System. [27](#)

**CL** Confidence Level. [49](#)

**COOL** ATLAS Condition Database. [28](#)

**CR** Control Region. [43](#)

**CSC** Cathode Strip Chambers. [20](#)

**CST** Calorimeter Soft Term. [36](#)

**CT** Calorimeter Tagged. [35](#)

**EB** Extended Barrel. [25](#)

**EM** electromagnetic. [18](#)

- FCal** LAr Forward Calorimeter. [19](#)
- FEB** Front-End Board. [34](#)
- GCW** Global Cell Weighting. [38](#)
- GS** Global Sequential. [38](#)
- HEC** Hadronic End-cap Calorimeter. [19](#)
- HFN** High Frequency Noise. [28](#)
- HG** High Gain. [26](#)
- HGHG** High Gain – High Gain. [28](#)
- HGLG** High Gain – Low Gain. [28](#)
- HL–LHC** High Luminosity LHC. [18](#)
- HLT** High Level Trigger. [22](#)
- HS** Hard Scatter. [37](#)
- HV** High Voltage. [34](#)
- IBL** Insertable B-Layer. [18](#)
- ID** Inner Detector. [17](#)
- IOV** Interval Of Validity. [29](#)
- IP** interaction point. [16](#)
- ISR** Initial State Radiation. [42](#)
- ITC** Intermediate Tile Calorimeter. [25](#)
- JES** Jet Energy Scale. [37](#)
- JVF** Jet Vertex Fraction. [37](#)
- JVT** Jet Vertex Tagger. [37](#)
- L1** Level One. [22](#)
- LAr** Liquid Argon. [19](#)
- LB** Long Barrel. [25](#)
- LCW** Local Cluster Weighting. [38](#)
- LFN** Low Frequency Noise. [28](#)
- LG** Low Gain. [26](#)
- LGHG** Low Gain – High Gain. [28](#)

- LGLG** Low Gain – Low Gain. [28](#)
- LHC** Large Hadron Collider. [15](#)
- LSP** Lightest Supersymmetric Particle. [13](#)
- LUCID** Luminosity measurement using Cerenkov Integrating Detector. [20](#)
- LVPS** Low Voltage Power Supply. [28](#)
- MC** Monte Carlo. [28](#)
- MDT** Monitored Drift Tubes. [20](#)
- MS** Muon Spectrometer. [20](#)
- MSSM** Minimal Supersymmetric Standard Model. [13](#)
- NCB** Non Collision Background. [42](#)
- OF** Optimal Filtering. [26](#)
- OR** Overlap Removal. [33](#)
- PDF** Parton Distribution Function. [43](#)
- PMT** PhotoMultiplier Tube. [24](#)
- PS** Proton Synchrotron. [15](#)
- PSB** Proton Synchrotron Booster. [15](#)
- PU** Pile Up. [37](#)
- PV** Primary Vertex. [33](#)
- RMS** Root Mean Square. [27](#)
- ROD** ReadOut Driver. [26](#)
- RoIs** Region of Interest. [22](#)
- RPC** Resistive Plate Chambers. [20](#)
- SA** Standalone. [35](#)
- SCT** SemiConductor Tracker. [18](#)
- SM** Standard Model. [3](#)
- SPS** Super Proton Synchrotron. [15](#)
- SR** Signal Region. [42](#)
- ST** Segment Tagged. [35](#)
- SUSY** Supersymmetry. [12](#)

- TGC** Thin Gap Chamber. [20](#)
- TileCal** Tile Calorimeter. [19](#)
- TNF** Tile Noise Filter. [31](#)
- TRT** Transition Radiation Tracker. [18](#)
- TST** Track Soft Term. [36](#)
- TUCS** TileCal Universal Calibration Software. [30](#)
- WSF** Wavelength Shifting Fibers. [26](#)
- ZDC** Zero-Degree Calorimeter. [20](#)

# Bibliography

- [1] Ian J. R. Aitchison. “Supersymmetry and the MSSM: An Elementary introduction”. In: (2005). arXiv: [hep-ph/0505105 \[hep-ph\]](#).
- [2] The ATLAS Collaboration. “Search for new phenomena in final states with an energetic jet and large missing transverse momentum in  $pp$  collisions at  $\sqrt{s} = 13$  TeV using the ATLAS detector”. In: (2016). arXiv: [1604.07773 \[hep-ex\]](#).
- [3] F. Halzen and A. D. Martin. *Quark and Leptons: An introductory Course in Modern Particle Physics*. John Wiley & Sons INC, 1984.
- [4] G. 't Hooft. *Recent Developments in Gauge Theories*. Plenum Press, 1979.
- [5] Gian Francesco Giudice. “Naturally Speaking: The Naturalness Criterion and Physics at the LHC”. In: (2008). arXiv: [0801.2562 \[hep-ph\]](#).
- [6] Edvige Corbelli and Paolo Salucci. “The Extended Rotation Curve and the Dark Matter Halo of M33”. In: *Mon. Not. Roy. Astron. Soc.* 311 (2000), pp. 441–447. DOI: [10.1046/j.1365-8711.2000.03075.x](#). arXiv: [astro-ph/9909252 \[astro-ph\]](#).
- [7] P. A. R. Ade et al. “Planck 2013 results. I. Overview of products and scientific results”. In: *Astron. Astrophys.* 571 (2014), A1. DOI: [10.1051/0004-6361/201321529](#). arXiv: [1303.5062 \[astro-ph.CO\]](#).
- [8] Tarek Saab. “An Introduction to Dark Matter Direct Detection Searches & Techniques”. In: *The Dark Secrets of the Terascale*. 2013, pp. 711–738. DOI: [10.1142/9789814390163\\_0011](#). arXiv: [1203.2566 \[physics.ins-det\]](#). URL: <https://inspirehep.net/record/1093524/files/arXiv:1203.2566.pdf>.
- [9] Stephen P. Martin. “A Supersymmetry primer”. In: (1997). [Adv. Ser. Direct. High Energy Phys.18,1(1998)]. DOI: [10.1142/9789812839657\\_0001](#), [10.1142/9789814307505\\_0001](#). arXiv: [hep-ph/9709356 \[hep-ph\]](#).
- [10] John Ellis. “From Little Bangs to the Big Bang”. In: *Journal of Physics: Conference Series* 50.1 (2006), p. 8. URL: <http://stacks.iop.org/1742-6596/50/i=1/a=002>.
- [11] K. A. Olive et al. “Review of Particle Physics”. In: *Chin. Phys.* C38 (2014), p. 090001. DOI: [10.1088/1674-1137/38/9/090001](#).
- [12] Lyndon R Evans and Philip Bryant. “LHC Machine”. In: *J. Instrum.* 3 (2008). This report is an abridged version of the LHC Design Report (CERN-2004-003), S08001. 164 p. URL: <https://cds.cern.ch/record/1129806>.
- [13] The ATLAS Collaboration. “The ATLAS Experiment at the CERN Large Hadron Collider”. In: *Journal of Instrumentation* 3.08 (2008), S08003. URL: <http://stacks.iop.org/1748-0221/3/i=08/a=S08003>.

- [14] The CMS Collaboration. “The CMS experiment at the CERN LHC”. In: *Journal of Instrumentation* 3.08 (2008), S08004. URL: <http://stacks.iop.org/1748-0221/3/i=08/a=S08004>.
- [15] The ALICE Collaboration. “The ALICE experiment at the CERN LHC”. In: *Journal of Instrumentation* 3.08 (2008), S08002. URL: <http://stacks.iop.org/1748-0221/3/i=08/a=S08002>.
- [16] The LHCb Collaboration. “The LHCb Detector at the LHC”. In: *Journal of Instrumentation* 3.08 (2008), S08005. URL: <http://stacks.iop.org/1748-0221/3/i=08/a=S08005>.
- [17] The LHCf Collaboration. “The LHCf detector at the CERN Large Hadron Collider”. In: *Journal of Instrumentation* 3.08 (2008), S08006. URL: <http://stacks.iop.org/1748-0221/3/i=08/a=S08006>.
- [18] The TOTEM Collaboration. “The TOTEM Experiment at the CERN Large Hadron Collider”. In: *Journal of Instrumentation* 3.08 (2008), S08007. URL: <http://stacks.iop.org/1748-0221/3/i=08/a=S08007>.
- [19] C Lefevre. “LHC: the guide (English version). Guide du LHC (version anglaise)”. Feb. 2009. URL: <https://cds.cern.ch/record/1165534>.
- [20] E Carquin. “Forward Physics with ATLAS”. In: (May 2013). URL: <https://cds.cern.ch/record/1547762>.
- [21] M Capeans et al. *ATLAS Insertable B-Layer Technical Design Report*. Tech. rep. CERN-LHCC-2010-013. ATLAS-TDR-19. Geneva: CERN, Sept. 2010. URL: <http://cds.cern.ch/record/1291633>.
- [22] C. W. Fabjan and F. Gianotti. “Calorimetry for particle physics”. In: *Rev. Mod. Phys.* 75 (2003), pp. 1243–1286. DOI: [10.1103/RevModPhys.75.1243](https://doi.org/10.1103/RevModPhys.75.1243).
- [23] L Fabbri. “Forward Detectors in ATLAS: ALFA, ZDC and LUCID”. In: (Apr. 2009). DIS09. Start date 26/04/2009. URL: <https://cds.cern.ch/record/1172844>.
- [24] Aranzazu Ruiz-Martinez and ATLAS Collaboration. *The Run-2 ATLAS Trigger System*. Tech. rep. ATL-DAQ-PROC-2016-003. Geneva: CERN, Feb. 2016. URL: <https://cds.cern.ch/record/2133909>.
- [25] The ATLAS Collaboration. “Hadron energy reconstruction for the ATLAS calorimetry in the framework of the nonparametrical method”. In: *Nucl. Instrum. Meth.* A480 (2002), pp. 508–523. DOI: [10.1016/S0168-9002\(01\)01229-3](https://doi.org/10.1016/S0168-9002(01)01229-3). arXiv: [hep-ex/0104002 \[hep-ex\]](https://arxiv.org/abs/hep-ex/0104002).
- [26] *ATLAS tile calorimeter: Technical Design Report*. Technical Design Report ATLAS. Geneva: CERN, 1996. URL: <https://cds.cern.ch/record/331062>.
- [27] *TileCal Approved Plots*. URL: <https://twiki.cern.ch/twiki/bin/view/AtlasPublic/ApprovedPlotsTile>.
- [28] B S M Peralva et al. *The TileCal Energy Reconstruction for Collision Data Using the Matched Filter*. Tech. rep. ATL-TILECAL-PROC-2013-023. Geneva: CERN, Nov. 2013. URL: [http://cds.cern.ch/record/1629575](https://cds.cern.ch/record/1629575).
- [29] Alexander Solodkov. *Performance of the ATLAS Tile Calorimeter*. Tech. rep. ATL-TILECAL-PROC-2015-024. Geneva: CERN, Dec. 2015. URL: <https://cds.cern.ch/record/2114824>.

- [30] G. Aad et al. “Readiness of the ATLAS Tile Calorimeter for LHC collisions”. In: *Eur. Phys. J.* C70 (2010), pp. 1193–1236. DOI: [10.1140/epjc/s10052-010-1508-y](https://doi.org/10.1140/epjc/s10052-010-1508-y). arXiv: [1007.5423 \[physics.ins-det\]](https://arxiv.org/abs/1007.5423).
- [31] *TileCal Approved Plots*. URL: <https://twiki.cern.ch/twiki/bin/view/AtlasPublic/ApprovedPlotsTileNoise>.
- [32] G Bertoli. “TileCal Electronic Noise in 2011 With ATLAS RUN I Reprocessing”. In: (Feb. 2014). URL: <https://cds.cern.ch/record/1646961>.
- [33] G Piacquadio, K Prokofiev, and A Wildauer. “Primary vertex reconstruction in the ATLAS experiment at LHC”. In: *Journal of Physics: Conference Series* 119.3 (2008), p. 032033. URL: <http://stacks.iop.org/1742-6596/119/i=3/a=032033>.
- [34] *Electron identification measurements in ATLAS using  $\sqrt{s} = 13$  TeV data with 50 ns bunch spacing*. Tech. rep. ATL-PHYS-PUB-2015-041. Geneva: CERN, Sept. 2015. URL: <https://cds.cern.ch/record/2048202>.
- [35] The ATLAS Collaboration. *Muon reconstruction performance in early  $\sqrt{s} = 13$  TeV data*. Tech. rep. ATL-PHYS-PUB-2015-037. Geneva: CERN, Aug. 2015. URL: <https://cds.cern.ch/record/2047831>.
- [36] W Lampl et al. *Calorimeter Clustering Algorithms: Description and Performance*. Tech. rep. ATL-LARG-PUB-2008-002. ATL-COM-LARG-2008-003. Geneva: CERN, Apr. 2008. URL: <https://cds.cern.ch/record/1099735>.
- [37] Matteo Cacciari, Gavin P. Salam, and Gregory Soyez. “The Anti-k(t) jet clustering algorithm”. In: *JHEP* 04 (2008), p. 063. DOI: [10.1088/1126-6708/2008/04/063](https://doi.org/10.1088/1126-6708/2008/04/063). arXiv: [0802.1189 \[hep-ph\]](https://arxiv.org/abs/0802.1189).
- [38] *Pile-up subtraction and suppression for jets in ATLAS*. Tech. rep. ATLAS-CONF-2013-083. Geneva: CERN, Aug. 2013. URL: <https://cds.cern.ch/record/1570994>.
- [39] *Tagging and suppression of pileup jets with the ATLAS detector*. Tech. rep. ATLAS-CONF-2014-018. Geneva: CERN, May 2014. URL: <http://cds.cern.ch/record/1700870>.
- [40] Marianna Testa. “Performance of pile-up mitigation techniques for jets in pp collisions with the ATLAS detector”. In: (June 2015). URL: <https://cds.cern.ch/record/2022887>.
- [41] *Measurement of the jet mass scale and resolution uncertainty for large radius jets at  $\sqrt{s} = 8$  TeV using the ATLAS detector*. Tech. rep. ATLAS-CONF-2016-008. Geneva: CERN, Mar. 2016. URL: <https://cds.cern.ch/record/2139642>.
- [42] *Jet energy scale and its systematic uncertainty in proton-proton collisions at  $\sqrt{s}=7$  TeV in ATLAS 2010 data*. Tech. rep. ATLAS-CONF-2011-032. Geneva: CERN, Mar. 2011. URL: <http://cds.cern.ch/record/1337782>.
- [43] *Selection of jets produced in 13TeV proton-proton collisions with the ATLAS detector*. Tech. rep. ATLAS-CONF-2015-029. Geneva: CERN, July 2015. URL: <https://cds.cern.ch/record/2037702>.
- [44] John Alison and I. J. Kroll. “The Road to Discovery: Detector Alignment, Electron Identification, Particle Misidentification, WW Physics, and the Discovery of the Higgs Boson”. Presented 08 Nov 2012. PhD thesis. Pennsylvania U.: Pennsylvania U., Dec. 2012. URL: <https://cds.cern.ch/record/1536507>.

- [45] Benjamin Hylton Brunt et al. *Expected performance of missing transverse momentum reconstruction for the ATLAS detector at  $\sqrt{s} = 13$  TeV*. Tech. rep. ATL-COM-PHYS-2015-347. Geneva: CERN, May 2015. URL: <https://cds.cern.ch/record/2013489>.
- [46] *SUSY Approved Plots*. URL: <http://atlas.web.cern.ch/Atlas/GROUPS/PHYSICS/PAPERS/SUSY-2015-06/>.
- [47] *Monojet Approved Plots*. URL: <https://atlas.web.cern.ch/Atlas/GROUPS/PHYSICS/PAPERS/EXOT-2015-03/>.
- [48] The ATLAS Collaboration. “Search for squarks and gluinos with the ATLAS detector in final states with jets and missing transverse momentum using  $4.7 \text{ fb}^{-1}$  of  $\sqrt{s}=7$  TeV proton-proton collision data”. In: *Phys. Rev. D* 87 (1 Jan. 2013), p. 012008. DOI: [10.1103/PhysRevD.87.012008](https://doi.org/10.1103/PhysRevD.87.012008). URL: <http://link.aps.org/doi/10.1103/PhysRevD.87.012008>.
- [49] The ATLAS Collaboration. “Characterisation and mitigation of beam-induced backgrounds observed in the ATLAS detector during the 2011 proton-proton run”. In: *Journal of Instrumentation* 8.07 (2013), P07004. URL: <http://stacks.iop.org/1748-0221/8/i=07/a=P07004>.
- [50] The ATLAS Collaboration. “Search for new phenomena with the monojet and missing transverse momentum signature using the ATLAS detector in proton–proton collisions”. In: *Physics Letters B* 705.4 (2011), pp. 294–312. ISSN: 0370-2693. DOI: <http://dx.doi.org/10.1016/j.physletb.2011.10.006>. URL: <http://www.sciencedirect.com/science/article/pii/S037026931101238X>.
- [51] Johann H. Kuhn et al. “Electroweak corrections to hadronic production of W bosons at large transverse momenta”. In: *Nucl. Phys.* B797 (2008), pp. 27–77. DOI: [10.1016/j.nuclphysb.2007.12.029](https://doi.org/10.1016/j.nuclphysb.2007.12.029). arXiv: [0708.0476 \[hep-ph\]](https://arxiv.org/abs/0708.0476).
- [52] Paweł Jan Klimek, Christophe Clément, and Barbro Åsman. “Search for Charginos and Sleptons in ATLAS and Identification of Pile-up with the Tile Calorimeter”. Presented 08 Oct 2015. PhD thesis. Stockholm U., Aug. 2015. URL: <https://cds.cern.ch/record/2062001>.
- [53] A L Read. “Modified frequentist analysis of search results (the  $CL_s$  method)”. In: CERN-OPEN-2000-205 (2000). URL: <https://cds.cern.ch/record/451614>.